Macroscopic States of Dipolar Quantum Gases

Von der Fakultät Mathematik und Physik der Universität Stuttgart
zur Erlangung der Würde eines Doktors der
Naturwissenschaften (Dr. rer. nat.) genehmigte Abhandlung

vorgelegt von

Matthias Wenzel

aus Reutlingen

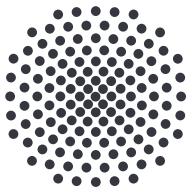

Hauptberichter	Prof. Dr. Tilman Pfau
Mitberichter	Prof. Dr. Martin Dressel
Prüfungsvorsitzender	Prof. Dr. Hans Peter Büchler
Tag der Prüfung	14.12.2018

5. Physikalisches Institut
Universität Stuttgart
2018

Abstract

In this thesis, we investigate macroscopic many-body quantum states of ultracold bosons with dipolar interaction both experimentally and theoretically. We thereby focus on a novel state of matter, the dipolar quantum droplet, that exists due to the interplay of attractive binary interactions and repulsive quantum fluctuations.
In this context, we predict groundstates with multiple droplets. These are promising candidates for the realization of a supersolid phase merging both superfluidity and a density modulation, that resembles the solid phase. Furthermore, we extend our studies on single droplets and measure its collective excitations. We also investigate the immersion of a fermionic impurity to probe the bosonic quantum droplet and predict a novel kind of droplet for an inverted dipolar interaction.
In addition, we study the superfluid properties of a Bose-Einstein condensate with dipolar interactions featuring an anisotropic excitation spectrum. Based on this effect, we measure an anisotropy of the critical velocity for the breakdown of superfluidity in the gas and predict the deformation of vortex cores and striped vortex lattices in rotating gases for our experimental parameters.

List of Publications

- H. Kadau, M. Schmitt, M. Wenzel, C. Wink, T. Maier, I. Ferrier-Barbut, and T. Pfau, *Observing the Rosensweig instability of a quantum ferrofluid*, Nature **530**, 194 (2016).
- I. Ferrier-Barbut, H. Kadau, M. Schmitt, M. Wenzel, and T. Pfau, *Observation of Quantum Droplets in a Strongly Dipolar Bose Gas*, Phys. Rev. Lett. **116**, 215301 (2016).
- M. Schmitt, M. Wenzel, F. Böttcher, I. Ferrier-Barbut, and T. Pfau, *Self-bound droplets of a dilute magnetic quantum liquid*, Nature **539**, 259 (2016).
- I. Ferrier-Barbut, M. Schmitt, M. Wenzel, H. Kadau, and T. Pfau, *Liquid quantum droplets of ultracold magnetic atoms*, J. Phys. B. **49**, 214004 (2016).
- M. Wenzel, F. Böttcher, T. Langen, I. Ferrier-Barbut, and T. Pfau, *Striped states in a many-body system of tilted dipoles*, Phys. Rev. A **96**, 053630 (2017).
- I. Ferrier-Barbut, M. Wenzel, M. Schmitt, F. Böttcher, and T. Pfau, *Onset of a modulational instability in trapped dipolar Bose-Einstein condensates*, Phys. Rev. A **97**, 011604(R) (2018).
- I. Ferrier-Barbut, M. Wenzel, F. Böttcher, T. Langen, M. Isoard, S. Stringari, and T. Pfau, *Scissors Mode of Dipolar Quantum Droplets of Dysprosium Atoms*, Phys. Rev. Lett. **120**, 160402 (2018).
- M. Wenzel, F. Böttcher, J. Schmidt, M. Eisenmann, T. Langen, T. Pfau, and I. Ferrier-Barbut, *Anisotropic Superfluid Behavior of a Dipolar Bose-Einstein Condensate*, Phys. Rev. Lett. **121**, 030401 (2018).
- M. Wenzel, T. Pfau, and I. Ferrier-Barbut, *A fermionic impurity in a dipolar quantum droplet*, Physica Scripta **93**, 104004 (2018).

Prior publications

- T. Maier, H. Kadau, M. Schmitt, M. Wenzel, I. Ferrier-Barbut, T. Pfau, A. Frisch, S. Baier, K. Aikawa, L. Chomaz, M. J. Mark, F. Ferlaino, C. Makrides, E. Tiesinga, A. Petrov, and S. Kotochigova, *Emergence of Chaotic Scattering in Ultracold Er and Dy*, Phys. Rev. X **5**, 041029 (2015).
- T. Maier, I. Ferrier-Barbut, H. Kadau, M. Schmitt, M. Wenzel, C. Wink, T. Pfau, K. Jachymski, and P. S. Julienne, *Broad universal Feshbach resonances in the chaotic spectrum of dysprosium atoms*, Phys. Rev. A **92**, 060702(R) (2015).

Contents

Zusammenfassung

Die gewöhnliche Materie, die uns im täglichen Leben umgibt, besteht aus einzelnen Atomen. Abhängig von der Spezies und den äußeren Gegebenheiten, befinden sich diese Atome typischerweise in einem gasförmigen, flüssigen oder festen Aggregatzustand. In der Gasphase ist die kinetische Energie der Atome größer als die Wechselwirkung zwischen den Atomen, sodass deren typischer Abstand viel größer als die Ausdehnung der Partikel ist. Ein solches System ist komprimierbar und füllt einen leeren Behälter homogen aus. In einer Flüssigkeit sind die kinetische Energie und die Wechselwirkungsstärke vergleichbar, wodurch sich ein bevorzugter Abstand mit beliebiger Ausrichtung zwischen den Atomen einstellt. Deshalb besitzt eine Flüssigkeit ein konstantes Volumen und lässt sich kaum komprimieren, nimmt aber die Form des Behälters an. Im Gegensatz dazu ist die kinetische Energie im Festkörper vernachlässigbar, wodurch sich die Atome durch deren gegenseitige Wechselwirkung in kristallinen Strukturen mit Fernordnung arrangieren.

Bei sehr niedrigen Temperaturen kurz über dem absoluten Nullpunkt sollte daher die kinetische Energie verschwinden. Dementsprechend erwarten wir alle Spezies in fester Form vorzufinden. Eine berühmte Ausnahme ist flüssiges Helium, das unterhalb von 2 K *suprafluid* wird. Dieser Zustand ist charakterisiert durch eine verschwindende Viskosität, sehr ähnlich zum *supraleitenden* Zustand, bei dem der elektrische Widerstand verschwindet. Letzterer wurde bereits 1911 von K. Onnes in festem Quecksilber bei Temperaturen von 4 K entdeckt. In beiden Fällen ist das makroskopische Verhalten auf Quantenphänomene zurückzuführen.

Seit der Erzeugung der ersten *Bose-Einstein Kondensate* (BEKs) im Jahre 1995 und *entarteten Fermigasen* im Jahre 1999 in ultrakalten verdünnten Gasen, steht eine herausragende Plattform zur Untersuchung solcher makroskopischer Quanteneffekte bereit. Diese Materiezustände existieren bei Temperaturen unterhalb von 1 µK und Dichten, die mehrere Größenordnungen unterhalb derer von Festkörpern liegen. Der große Vorteil liegt in der ausgezeichneten Kontrolle der internen und externen Freiheitsgrade sowie der relativen Einfachheit des Systems, die ein umfassendes theoretisches Verständnis ermöglicht. Aus diesen Gründen haben sich ultrakalte Atome zu einem stetig wachsenden Forschungsgebiet mit dem Fokus auf der Untersuchung von makroskopischen Quantenphänomenen entwickelt. Von den vielen bahnbrechenden Untersuchungen wollen wir die folgenden nennen: Interferenz von Materiewellen, Quantenwirbel in einem rotierenden BEK, den Phasenübergang vom bosonischen Suprafluid zum Mott-Isolator, BEKs von Molekülen aus Fermionen und Suprafluidität in stark wechselwirkenden Fermigasen. In den letzten Jahren wurden Quantengasmikroskope entwickelt, die direkten Einblick und die Kontrolle

von einzelnen Atomen des Vielkörperzustands in optischen Gittern für Bosonen sowie auch für Fermionen ermöglichen. All diese Experimente basieren auf Alkaliatomen mit isotropen kurzreichweitigen Wechselwirkungen.
Die Erweiterung dieses Forschungsfelds zu neuartigen Quantengasen basierend auf anderen atomaren Spezies, Molekülen, oder exotischen Systemen wie Photonen im Mikroresonator, Magnonen oder Exziton-Polaritonen ermöglicht dabei die Beobachtung einer Vielzahl weiterer Phänomene. Die Erzeugung eines Bose-Einstein Kondensats mit Chromatomen in unserem Labor im Jahre 2004 war der Startpunkt für die Erforschung von *dipolaren Quantengasen*, bei denen das vergleichsweise große magnetische Moment der Atome zu einer merklichen magnetischen Dipol-Dipol-Wechselwirkung zwischen den Atomen führt. Im Gegensatz zur Wechselwirkung in Alkaliatomen ist diese anisotrop und langreichweitig. Dies führt beispielsweise zu einem Kollaps des Quantengases in Form eines kurzlebigen Kleeblatt-Musters. Die Forschung in unserer Gruppe wurde dabei durch ähnliche Studien in Paris ergänzt.
Die Realisierung von Quantengasen aus Dysprosium- oder Erbiumatomen mit stärkerer dipolarer Wechselwirkung führte zur Beobachtung von weiteren Effekten wie die Verformung der Fermifläche, chaotische Streuung in Lanthaniden, Wechselwirkungen zwischen benachbarten Plätzen in optischen Gittern oder die Studien zur Thermalisierung durch die dipolare Wechselwirkung.
Während meiner Zeit am Dysprosium-Experiment haben wir unser erstes BEK im Juni 2014 und das erste entartete Fermigas im Februar 2015 erzeugt. Unsere anfänglichen Studien zu den Streueigenschaften dieses Elements wurden dann durch die Entdeckung von langlebigen dipolaren *Quantentröpfchen* gekrönt, die, wie wir später belegen konnten, durch Quantenfluktuationen stabilisiert werden. Dieser Zustand war absolut unerwartet und löste eine Vielzahl von theoretischen Erklärungsversuchen aus. Während das anfängliche BEK gasförmig ist, zeigen diese Tröpfchen die Eigenschaften einer *Quantenflüssigkeit*, wie beispielsweise verminderte Komprimierbarkeit, auf. Im Gegensatz zu anderen Flüssigkeiten ist die Dichte allerdings mehrere Größenordnungen geringer und das Tröpfchen nicht rund, sondern durch die dipolare Wechselwirkung gestreckt. Weitere Experimente zeigten außerdem, dass sich ein solches Tröpfchen nicht ausdehnt wenn der einschließende Behälter entfernt wird, was im Gebiet der Quantengase eine absolute Neuheit darstellte. Unsere Studien wurden dabei durch die Untersuchung von Quantentröpfchen aus Erbiumatomen ergänzt. In neuerer Zeit wurde dieses wachsende Forschungsgebiet durch die Realisierung von Quantentröpfchen aus Mischungen von zwei BEKs mit kurzreichweitigen Wechselwirkungen komplettiert.

In dieser Arbeit untersuchen wir diese Quantentröpfchen in umfassenden numerischen Simulationen und neuartigen Experimenten. Ein Teil dieser Promotion war der Entwicklung dieser Simulationen gewidmet, welche sich als unerlässlich für das Verständnis dieses eigentümlichen Materiezustandes erwiesen. Diese sind außerdem wichtig um Parameterbereiche zu finden, für die die gewünschten Effekte unter experimentellen Bedingungen beobachtet werden können.

Mit diesem Werkzeug finden wir neuartige "gestreifte" Grundzustände mit mehreren Tröpfchen, welche durch Frustration entlang der Polarisationsachse der Dipole induziert werden. Diese sind besonders interessant, weil sich eine gemeinsame Phase der beteiligten Tröpfchen über das ganze System einstellen kann. Dieses Verhalten entspricht einer möglichen Realisierung eines *suprasoliden* Materiezustands, welcher Suprafluidität mit einer ortsabhängigen Modulation der Dichte in Anlehnung an einen Festkörper verbindet. Im Experiment können wir metastabile Streifenzustände erzeugen, finden aber in Interferenzexperimenten keine solche globale Phasenkohärenz des suprasoliden Zustands. Weiterführende semi-analytische und numerische Untersuchungen bestätigen dieses Verhalten und deuten auf einen Parameterbereich hin, bei dem sich diese Phasenkohärenz in zukünftigen Experimenten einstellen sollte.

Mit Messungen der kollektiven Anregungen untersuchen wir auch die internen Eigenschaften der Quantentröpfchen. Dabei diskutieren wir die Natur der Scherenmode, und präsentieren Messungen dieser sowie der Quadrupolmode. Basierend auf einer zeitabhängigen Variationsrechnung extrahieren wir damit einen Wert von $a_{\mathrm{bg}} = 69(4)\,a_0$ für die Stärke der kurzreichweitigen Wechselwirkung im Isotop ^{164}Dy.

Dieser Wert weicht von früheren Messungen ab, weshalb wir außerdem Erweiterungen der gängigen theoretischen Beschreibung für endliche Temperaturen untersuchen. Wir führen diese Abweichung auf eine Verstärkung der dipolaren Streuung zurück, welche auch mit Messungen in klassischen Gasen bei höheren Temperaturen kompatibel ist. Mit den aktuellen Werkzeugen können wir jedoch die Temperatur eines Quantentröpfchens nicht messen. Daher untersuchen wir theoretisch, ob ein Fremdatom in das Tröpfchen eingebracht werden kann. Für ein dipolares Fermion finden wir dabei mehrere gebundene Zustände, was ein vielversprechender erster Schritt für die Messung der internen Eigenschaften mit Hilfe solcher Fremdatome darstellt. Des Weiteren entdecken wir in der Theorie eine weitere Klasse von Quantentröpfchen für eine invertierte dipolare Wechselwirkung, welche mit Hilfe eines schnell rotierenden Magnetfelds im zeitlichen Mittel erzeugt werden kann. Diese *Pfannküchlein* genannten Zustände sind dementsprechend zweidimensionale Strukturen, die sich senkrecht zur gemittelten Polarisationsachse anordnen.

Unsere Untersuchungen sind allerdings nicht auf Quantentröpfchen beschränkt. Die di-

polare Wechselwirkung im BEK führt zu einer Anisotropie des Anregungsspektrums und dementsprechend auch zu einer anisotropen kritischen Geschwindigkeit einer Anregung, unterhalb derer Suprafluidität auftritt. Im Experiment realisieren wir eine Situation, bei der eine Bewegung entlang der Polarisationsachse reibungsfrei ist, während eine Bewegung bei der selben Geschwindigkeit senkrecht dazu zu einer Anregung und dementsprechend Reibung führt. Unsere Messungen von kritischer Geschwindigkeit und der Heizrate stimmen exzellent mit den numerischen Simulationen überein. Mit letzteren untersuchen wir auch die Möglichkeit dipolare Effekte von Quantenwirbeln in rotierenden dipolaren Gasen im Experiment zu realisieren. In zukünftigen Experimenten erwarten wir deshalb einen deformierten Kern solcher Wirbel, die sich außerdem durch die dipolare Wechselwirkung in parallelen Streifen anordnen, zu beobachten.

All of physics is either impossible or trivial.
It is impossible until you understand it,
and then it becomes trivial.
— *Ernest Rutherford*

Chapter 1

Introduction

The ordinary matter surrounding us in everyday life is made up of atoms. Depending on the species and the ambient conditions, an amount of atoms is typically found in either the gas, the liquid, or the solid phase. In the gas phase, the kinetic energy of particles dominates over the interparticle forces and the typical distance is much larger than the particle size. Such a system is compressible and, when placed inside an empty container, will expand to homogeneously fill the latter. In a liquid kinetic energy and the interparticle forces are on the same order of magnitude, such that the latter determine a fixed interparticle distance but atoms can still align freely. Thus liquids are almost incompressible having a constant volume, but follow the shape of the surrounding container. In a solid, the kinetic energy is negligible and atoms align due to the interparticle forces in crystalline structures with long-range ordering.

For very low temperatures just above absolute zero, kinetic energy should vanish and we therefore expect to find all species in the solid phase. A famous exception is liquid helium, which does not turn into a solid, but rather becomes a *superfluid* below 2 K [12]. This state is characterized by a vanishing viscosity, much like the *superconducting* state, for which the electrical resistance vanishes. The latter was discovered by K. Onnes for solid mercury at a temperature of 4 K already in 1911 [13]. In both cases, the macroscopic phenomena observed at low temperatures cannot be explained by classical physics anymore, but instead are due to quantum physics.

An outstanding experimental platform to study such macroscopic quantum effects was heralded by the creation of *Bose-Einstein condensates* (BECs) in 1995 [14, 15] and *degenerate Fermi gases* in 1999 [16] from ultracold dilute gases of alkali atoms. These states of matter exist at temperatures below 1 µK and densities several orders of magnitude lower compared to solids. Their enormous advantage for experimentalists is the superb control of both the internal and external degrees of freedom. Moreover, on the theoretical

side their relative simplicity enables a comprehensive understanding. For these reasons they have become an ever-growing playground to study many-body quantum phenomena. Amongst the vast amount of pioneering studies, we highlight the observation of matter-wave interference [17], vortices in a rotating BEC [18], the phase transition from a bosonic superfluid to a Mott insulator state [19], BECs of molecules paired from fermions [20, 21], and superfluidity in strongly interacting Fermi gases [22]. Nowadays, quantum gas microscopes also enable the direct imaging and manipulation of single atoms of the many-body state in optical lattices for both bosons [23, 24] and fermions [25–27]. Although these experiments cover a wide range of phenomena, these are all based on alkali atoms possessing an isotropic short-range interaction.

Extending the field to new kinds of quantum degenerate gases based on different atomic species, molecules, or even completely other systems, e.g. photons in a microcavity [28], magnon quasiparticles [29], and exciton polaritons [30], greatly enriches the accessible phenomena. The condensation of chromium atoms in our lab in 2004 marked the starting point for the studies of *ultracold dipolar gases* [31], where the large magnetic moment of the atom gives rise to an observable magnetic dipole-dipole interaction (DDI) [32, 33], which is both long-range and anisotropic in distinction to the previous short-range interaction. For a sufficiently weak short-range interaction the quantum gas collapses in a d-wave pattern due to the predominant dipolar interaction [34, 35]. These studies in our group were complemented by the Paris group investigating spinor chromium BECs [36–39]. With the first quantum gases of dysprosium [40, 41] and erbium [42, 43] degenerate atoms with even stronger dipolar interaction became available. These triggered the observation of a series of novel effects like the deformation of the Fermi surface [44], chaotic scattering in lanthanides [10, 45], nearest-neighbor interactions in an optical lattice [46], or the study of thermalization near integrability [47].

During my time at the dysprosium experiment, we created our first BEC in June 2014 and our first degenerate Fermi gas in February 2015 with this apparatus[1]. Our initial studies on the scattering properties of this element [10, 11] culminated in the discovery of long-lived dipolar *quantum droplets* [1], which we found to be stabilized by quantum fluctuations [2, 4, 48]. The existence of this state was not expected at all at the time and quickly triggered a variety of theory contributions in order to understand its properties [49–55]. While the initial BEC is a dilute gas, it turned out that the droplets rather share many properties of liquids, including their incompressibility. However, this exotic *quantum liquid* exhibits a density that is several orders of magnitude lower compared to any other liquid and also, due to the anisotropy of the dipolar interaction, has a very elongated

[1] Second in the world! Here, I want to thank my former colleagues T. Maier, H. Kadau and M. Schmitt.

shape. Furthermore, we confirmed that the droplets do not expand once released from a container [3]. Such a self-bound behavior is an absolute novelty in the field of quantum gases. Our studies were complemented by the creation of quantum droplets with erbium atoms [56], showing the universality of this phenomenon. Following the original proposal [48], also droplets of two-component Bose-Bose mixtures based on isotropic short-range interactions have later been created experimentally [57–59] extending this growing field of research.

Outline

In this thesis we investigate macroscopic many-body quantum states of ultracold dipolar bosons both experimentally and theoretically. In chapter 2 we describe their state-of-the-art theoretical description, which gives rise to both dipolar effects in BECs and dipolar quantum droplets. In this context we further introduce a set of numerical tools, that were developed during this thesis to understand and predict such phenomena.
After providing insight into the recent additions to our experimental setup in chapter 3, we present first results in chapter 4. There, we investigate ensembles of droplets in confined geometries both theoretically and experimentally. This gives rise to spontaneously formed many-droplet states, so-called "striped states". Such behavior naturally raises the question, whether the many-droplet state is phase-coherent, i.e. sharing a common phase throughout the whole system. A coherent droplet crystal would be considered a *supersolid* state of matter, merging superfluid behavior with a density modulation resembling the solid phase. We therefore investigate the coherence properties of these many-droplet states.
Furthermore, we study the properties of single droplets and present measurements of their collective excitations in chapter 5. We are especially interested in the scissors mode, since it is conceptually different in a dipolar system compared to previous observations. Using a time-dependent theory model we can extract important details of the short-range scattering properties in dysprosium.
In chapter 6, we compare this result with a previous measurement based on the critical atom number for the stability of self-bound quantum droplets. We find a clear deviation, which we attribute to an enhancement of dipolar scattering at finite-temperature. In addition, we evaluate the immersion of a fermionic dipolar impurity in such a bosonic quantum droplet, which is the first step towards probing quantum droplets with impurities, and find a new class of pancake-like droplet states for inverted dipolar interaction.
Our research is not limited to the physics of quantum droplets, and we further investigate superfluidity of a dipolar BEC (dBEC) in chapter 7. Due to the anisotropy of the

dipolar interaction, the critical velocity for the onset of dissipation is modified, which we confirm experimentally by moving a laser beam through the condensate. Furthermore, we numerically investigate the creation and detection of vortices in a rotating dBEC paving the way for their future observation in our experiment.

Chapter 2

Ultracold dipolar bosons

In this chapter, we review the theoretical description of ensembles of bosonic atoms with a sizeable magnetic moment at ultracold temperatures. First, we introduce the concept of Bose-Einstein condensation for the ideal non-interacting gas. Taking into account the conceptually different contact and dipolar interactions then leads to a mean-field theory for the interacting Bose-Einstein condensate. A first-order correction to this theory due to quantum fluctuations gives rise to dipolar quantum liquids.
Starting with the homogeneous gas we then investigate dipolar effects of the excitation spectrum. For a harmonically trapped gas we introduce the variational method to describe the ground state and the dynamics of both dipolar Bose-Einstein condensates and quantum droplets. In a next step, we study the exact solutions of the eGPE numerically, which gives rise to additional effects. These tools form the basis to describe the experiments presented in this thesis.
The chapter is based on the excellent book by L. Pitaevskii and S. Stringari [60] and a review on dipolar condensates by T. Lahaye et.al. [61]. In addition, we describe the theory of dipolar quantum droplets, that emerge from quantum fluctuations, as introduced by A. Lima and A. Pelster for dipolar atoms [62, 63].

2.1. The ideal Bose gas

Based on the work by S. Bose in 1924 [64], who derived a statistical description of photons, A. Einstein predicted a phase transition for identical massive particles in 1925 [65, 66]. At sufficiently low temperature, these noninteracting particles would accumulate in the ground state of the system and form a macroscopic quantum state, nowadays known as a *Bose-Einstein condensate* (BEC). This phase transition is exclusively dictated by

quantum statistics, such that we can estimate the critical temperature T_c by the following qualitative argument. Many-body quantum effects become important once the coherence length of a particle's wavefunction λ_T is on the order of the inter-particle spacing $d = n^{-1/3}$. The latter is determined by the number density n, and the former is given by the thermal de Broglie wavelength $\lambda_\mathrm{T} = \sqrt{\frac{2\pi\hbar^2}{m k_\mathrm{B} T}}$ for a given temperature T. For the critical temperature T_c we then obtain

$$T_\mathrm{c} = \frac{2\pi\hbar^2}{k_\mathrm{B}} \frac{n^{2/3}}{m} \tag{2.1}$$

with the particle mass m, reduced Planck constant $\hbar$ and Boltzmann constant k_B[1]. This way, we can estimate the critical temperature to $T_\mathrm{c} = 3.5\,\mathrm{K}$ for liquid ^{4}He at a density of $10^{28}\,\mathrm{m}^{-3}$ [67], which is close to the λ-point $T_\lambda = 2.2\,\mathrm{K}$ at which it becomes superfluid. Experiments with cold gases of various species operate at densities $10^{19-21}\,\mathrm{m}^{-3}$, which yields $T_c \sim 1\,\mu\mathrm{K}$.

Such experiments are typically carried out in harmonic trapping potentials. Therefore, we summarize the basic quantities of the ideal Bose gas in this setting based on [60, ch. 10]. For identical bosons in a state k with energy ϵ_k the mean occupation number

$$\langle n_k \rangle = \frac{1}{e^{\beta(\epsilon_k - \mu)} - 1} \tag{2.2}$$

in the grand-canonical ensemble is determined by $\beta = 1/k_\mathrm{B}T$ and the chemical potential μ is fixed by the total particle number $N = \sum_k \langle n_k \rangle$. In the classical limit $k_\mathrm{B}T \gg \hbar\omega$ we recover the Boltzmann distribution $\langle n_k \rangle = e^{-\beta(\epsilon_k - \mu)}$. We assume a spherical harmonic potential $V_\mathrm{ext} = \frac{1}{2} m\omega^2 r^2$, with the trap frequency ω and characteristic length $a_\mathrm{ho} = \sqrt{\hbar/m\omega}$. This way, the single-particle Hamiltonian is $H = p^2/2m + \frac{1}{2}m\omega^2 r^2$, which is the well-known harmonic oscillator.

At zero temperature, all particles occupy its ground state $\phi_0(\boldsymbol{r})$ and the many-body wavefunction, which is symmetric under particle exchange, reads

$$\psi(\boldsymbol{r}_1, ..., \boldsymbol{r}_N) = \prod_k \phi_0(\boldsymbol{r_k}) \quad \text{with} \quad \phi_0(\boldsymbol{r}) = \frac{1}{(\pi a_\mathrm{ho}^2)^{3/4}} \exp\left(-\frac{r^2}{2a_\mathrm{ho}}\right) . \tag{2.3}$$

The density distribution thus becomes $n(\boldsymbol{r}) = N|\phi_0(\boldsymbol{r})|^2$, and the condensate is confined to a volume a_ho^3 independent of particle number. A BEC of noninteracting particles is therefore infinitely compressible. At finite temperature T excited states are populated

[1] Throughout this thesis energy units are given in units of Hz (by division of the planck constant) or nK (by disivion of the Boltzmann constant), since these are natural when working on experiments with ultracold atoms.

leaving $N_0 < N$ particles in the ground state. The fraction of condensed atoms

$$\frac{N_0}{N} = 1 - \left(\frac{T}{T_\mathrm{c}}\right)^3 \quad \text{with} \quad T_\mathrm{c} = 0.94\,\frac{\hbar\omega}{k_\mathrm{B}} N^{1/3} \tag{2.4}$$

is determined by the critical temperature T_c. For a typical trap with $\omega = 2\pi \times 70\,\mathrm{Hz}$ in the experiment, a noninteracting ^{164}Dy BEC with $N = 10^4$ atoms has a size of $a_\mathrm{ho} = 1\,\mu\mathrm{m}$ and yields a critical temperature of $T_c = 70\,\mathrm{nK}$.
An important property is the coherence, which can be investigated by means of the one-body density matrix $n^{(1)}(\boldsymbol{r}, \boldsymbol{r'}) = \langle\hat{\psi}^\dagger(\boldsymbol{r})\hat{\psi}(\boldsymbol{r'})\rangle$ given by the expectation value of the creation and annihilation operators $\hat{\psi}^\dagger$ and $\hat{\psi}$, respectively [60, ch. 2]. For the diagonal components with $\boldsymbol{r} = \boldsymbol{r'}$ it reduces to the density distribution $n(\boldsymbol{r}) = n^{(1)}(\boldsymbol{r}, \boldsymbol{r'})$. Introducing the relative coordinate $s = |\boldsymbol{r} - \boldsymbol{r'}|$ we can investigate the non-diagonal components $n^{(1)}(s) = n^{(1)}(\boldsymbol{r}, \boldsymbol{r'})$, which yields zero for $s \to \infty$ in the normal phase. Interestingly, for a BEC it converges to a finite value given by the condensate density, $n^{(1)}(s \to \infty) = n$. The persistence of coherence throughout the condensate is called *off-diagonal long-range order* [68]. BECs are thus coherent matter waves showing interference [17]. While there are many similarities between BECs and superfluids, we point out, that an ideal Bose gas is not a superfluid, see ch. 2.3.3.

2.2. Ultracold atoms & interactions

In the experiment, we realize such Bose-Einstein condensates with interacting atoms. The addition of interactions profoundly changes some of the properties described in the previous section and enriches the physics leading to a variety of quantum phenomena, that can be observed with interacting BECs. We are particularly interested in the element dysprosium with the electronic configuration $[\mathrm{Xe}]\,4f^{10}\,6s^2$ and the ground state $^5\mathrm{I}_8$. The total angular momentum $J = 8$ leads to a large magnetic moment and thus gives rise to a sizeable dipole-dipole interaction in addition to the contact interaction known from the study of alkali atoms. In the following we introduce both interactions, pointing the interested reader to a more thorough analysis on the scattering properties of dysprosium atoms to ref. [69].

Contact interaction

We consider *dilute gases*, where the range of inter-particle interactions r_0 is small compared to the average distance between particles $d = n^{-1/3}$, fixed by the number density n. Under these conditions, we can neglect interactions between three or more particles and reduce

our analysis to pairs of particles. Secondly, *ultracold* atoms are characterized by a de Broglie wavelength $\lambda_\mathrm{T} \sim n^{-1/3} \gg r_0$, which limits the momentum $p = \hbar k = h/\lambda_\mathrm{T}$ to low collisional energies[2] $E_\mathrm{kin} = \hbar^2 k^2/m$ satisfying the condition $kr_0 \ll 1$.
In this regime, collisions are elastic[3] and the interatomic potential is not resolved during the collision process. The only remainder of such a collision is a phase shift of the interatomic wavefunction, which is independent of the microscopic details of the interatomic potential. This phase shift can be expressed in terms of a single universal value, called the *s-wave scattering length* a_s, as shown e.g. in [60, ch. 9]. This scattering length can be positive or negative corresponding to a repulsive or attractive interaction. The elastic scattering cross-sections for identical bosons and fermions are then $\sigma_B = 8\pi a_\mathrm{s}^2$ and $\sigma_F = 0$, respectively, and we can replace the unknown short-range interaction potential by a *pseudopotential* of form

$$V_\mathrm{con}(\boldsymbol{r}) = g\,\delta(\boldsymbol{r}) \quad \text{with} \quad g = \frac{4\pi\hbar^2 a_\mathrm{s}}{m} \tag{2.5}$$

recovering the same physics.
Important tools for the study of cold gases are *Feshbach resonances*, that allow for arbitrary tuning of the scattering length. By means of a differential magnetic or light shift, a second scattering channel can be tuned in resonance with respect to the threshold. This gives rise to magnetic [70, 71] or optical [72, 73] Feshbach resonances. For the former, the dependence of the scattering length

$$a_\mathrm{s}(B) = a_\mathrm{bg}\left(1 - \frac{\Delta}{B - B_0}\right) \tag{2.6}$$

is determined by the background scattering length a_bg away from resonances, as well as the position B_0 and width Δ of the resonance. In dysprosium, the open $4f$-shell gives rise to a dense set of Feshbach resonances [10, 11].
In the vicinity of such resonances, inelastic three-body collisions lead to fast atom losses scaling approximately with a_s^4 close to resonance [74]. In appendix B, we present three-body spectra in the vicinity of broader resonances for ^{164}Dy.

Dipolar interaction

With a large magnetic moment $\mu_\mathrm{m} \approx 10\,\mu_\mathrm{B}$ in the ground state, dysprosium atoms are also subject to the magnetic dipole-dipole interaction or *dipolar interaction*. In the experiment,

[2] We introduced the reduced mass $\mu = m/2$ in the center-of-mass frame.
[3] Atoms are typically prepared in specific internal states to prevent inelastic collisions.

atoms are typically spin-polarized by an external magnetic field $\boldsymbol{B} \parallel \boldsymbol{\mu}_\mathbf{m}$. In this case, the general interaction reduces to the interaction potential

$$V_{\mathrm{dd}}(\boldsymbol{r}) = \frac{\mu_0 \mu_\mathrm{m}^2}{4\pi} \frac{1 - 3\cos^2\vartheta}{r^3} \tag{2.7}$$

which is anisotropic and long-range [61]. As illustrated in fig. (2.1a), depending on the angle ϑ, the interaction is attractive or repulsive defining the magic angle $\vartheta_\mathrm{m} = \arccos(1/\sqrt{3}) \approx 54.7\,\mathrm{deg}$ for zero interaction. Two dysprosium atoms spaced by 1 µm are subject to a dipolar interaction $V_{\mathrm{dd}}(r = 1\,\mu\mathrm{m}, \theta = \pi/2) \approx 1.3\,\mathrm{Hz}$. Although the magnetic moment is fixed, the strength of the dipolar interaction can be tuned by a rotating magnetic field giving rise to a time-averaged interaction [75], which has been realized recently [76].

For convenience, we define a characteristic length scale, called the *dipolar length* a_{dd}, and the relative dipolar strength $\varepsilon_{\mathrm{dd}}$ as

$$a_{\mathrm{dd}} = \frac{\mu_0 \mu_\mathrm{m}^2 m}{12\pi\hbar^2} \qquad \text{and} \qquad \varepsilon_{\mathrm{dd}} = \frac{a_{\mathrm{dd}}}{a_\mathrm{s}}\,. \tag{2.8}$$

In fig. (2.1b) we list some isotopes of magnetic atoms used in the field along with the corresponding dipolar and measured background scattering lengths. The homonuclear magnetic molecules would feature an eight-fold enhancement of the dipolar length in the ground state, but have only been realized in a weakly-bound manner close to a Feshbach resonance.

Due to the long-range character[4], the interaction energy is not extensive in the thermodynamic limit and depends on the global properties of the system, e.g. absolute atom number. In contrast, for the contact-interaction in the previous section the interaction energy only depends on the density, a local quantity. Importantly, all partial waves $l > 0$ contribute to the scattering amplitude for the DDI and we cannot reduce the interaction to a simple pseudo-potential. Fortunately, for low enough collisional energy[5] dipolar scattering becomes universal and only involves s-wave channels [80–82]. Within the Born approximation and away from resonances, the scattering amplitudes of both contact and dipolar interaction can conveniently be added and we obtain the total elastic scattering cross-sections

$$\sigma_\mathrm{B} = 8\pi\left(\frac{1}{5}a_{\mathrm{dd}}^2 + a_\mathrm{s}^2\right) \qquad \text{and} \qquad \sigma_\mathrm{F} = 8\pi\left(\frac{3}{5}a_{\mathrm{dd}}^2\right) \tag{2.9}$$

[4] We call a $1/r^n$ potential long-range in d dimensions, if the integral $\int_{r_\mathrm{c}}^{\infty} r^{-n}\mathrm{d}^d r$ with a small cut-off r_c diverges, which yields the condition $n \leq d$.

[5] Compared to the dipolar energy $E_D = V_{\mathrm{dd}}(r = \frac{3}{2}a_{\mathrm{dd}}, \theta = \pi/2) \approx 14\,\mu\mathrm{K}$ for dysprosium.

(a)

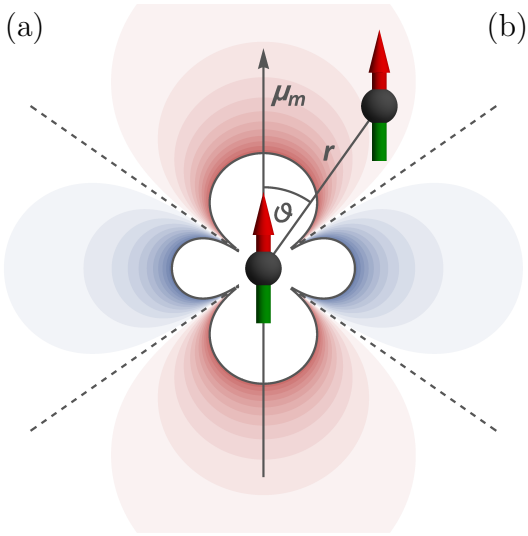

(b)

Dipole	μ_m (μ_B)	a_{dd} (a_0)	a_{bg} (a_0)	ε_{dd} (1)	Ref.
^{87}Rb	1	0.7	100.4(1)	0.01	[77]
^{52}Cr	6	15	102.5(4)	0.15	[78]
^{166}Er	6.98	65	67(2)	0.97	[56]
^{168}Er	6.98	66	137(1)	0.48	[46]
^{162}Dy	9.93	129	141(17)	0.91	[47]
^{164}Dy	9.93	131	69(4)	1.89	[7]
^{168}Er$_2$	14.0	530	-	-	[79]
^{164}Dy$_2$	19.9	1050	-	-	[11]

Figure 2.1.: **Magnetic dipole-dipole interaction.** (a) Dipole-dipole interaction of two polarized particles with magnetic moment $\boldsymbol{\mu_m}$ separated by $\boldsymbol{r}$, defining the angle ϑ. For ϑ smaller than the magic angle ϑ_m (dashed) the interaction is attractive (red) and above repulsive (blue). (b) List of ultracold atoms and molecules with magnetic moment μ_m, dipolar length a_{dd} and measured background scattering length a_{bg}. In the respective ground state, the homonuclear molecules would have an eight times larger dipolar length compared to the single atoms.

for identical bosons and fermions, respectively [69]. The dipolar interaction thus permits thermalization for ultracold identical fermions, as reported for both dysprosium [41] and later for erbium [43]. Going beyond the Born approximation, numerical calculations of the scattering amplitude with realistic inter-atom potentials confirm this behavior and conclude a small temperature-dependent enhancement of the DDI. For two dysprosium atoms this effect is +10% at a relative energy corresponding to $T = 100\,\mathrm{nK}$ [83, 84].

The dipolar interaction also couples the spin degrees of freedom and orbital angular momentum. As a consequence, dipolar collisions do not conserve magnetic quantum numbers allowing for *spin-changing collisions* [85]. Based on this effect, specialized cooling schemes were realized [86–88]. For our experimental parameters with large Zeeman splitting compared to the thermal energy, such spin flips are suppressed.

Finally, the complex scattering physics of the atom reduces to the full interaction potential

$$V_{\mathrm{int}}(\boldsymbol{r}) = V_{\mathrm{con}}(\boldsymbol{r}) + V_{\mathrm{dd}}(\boldsymbol{r}) \qquad \text{and} \qquad \tilde{V}_{\mathrm{int}}(\boldsymbol{q}) = \frac{g}{2}\left[1 + \varepsilon_{\mathrm{dd}}\left(3\cos^2\alpha - 1\right)\right] \tag{2.10}$$

for the Fourier transformation. The latter is independent of the modulus and depends on the angle α of momentum $\boldsymbol{q}$ with respect to the dipole axis in momentum space.

2.2.1. Gross-Pitaevskii equation

In this section, we present the mean-field theory for a condensate of interacting bosons, which is the basic description for the physics presented in this thesis. Starting within second quantization [60, ch. 5] the general Hamiltonian for the field operator $\hat{\psi}$ reads

$$\begin{aligned}\hat{H} = &\int \mathrm{d}\boldsymbol{r}\, \hat{\psi}^\dagger(\boldsymbol{r}) \left[-\frac{\hbar^2}{2m}\nabla^2 + V_{\mathrm{ext}}(\boldsymbol{r})\right] \hat{\psi}(\boldsymbol{r}) \\ &+ \frac{1}{2}\int \mathrm{d}\boldsymbol{r}' \int \mathrm{d}\boldsymbol{r}\, \hat{\psi}^\dagger(\boldsymbol{r})\hat{\psi}^\dagger(\boldsymbol{r}')V_{\mathrm{int}}(\boldsymbol{r}'-\boldsymbol{r})\hat{\psi}(\boldsymbol{r}')\hat{\psi}(\boldsymbol{r}) \end{aligned} \tag{2.11}$$

with a two-body interaction potential $V_{\mathrm{int}}(\boldsymbol{r}'-\boldsymbol{r})$ and an external potential $V_{\mathrm{ext}}(\boldsymbol{r})$. The time-dependence of this field operator is given by

$$\begin{aligned} i\hbar\frac{\partial}{\partial t}\hat{\psi}(\boldsymbol{r},t) = \left[\hat{\psi}(\boldsymbol{r},t), \hat{H}\right] = \Bigg[&-\frac{\hbar^2}{2m}\nabla^2 + V_{\mathrm{ext}}(\boldsymbol{r}) \\ &+ \int \mathrm{d}\boldsymbol{r}'\, \hat{\psi}^\dagger(\boldsymbol{r}',t)V_{\mathrm{int}}(\boldsymbol{r}'-\boldsymbol{r})\hat{\psi}(\boldsymbol{r}',t)\Bigg]\hat{\psi}(\boldsymbol{r},t) \end{aligned} \tag{2.12}$$

in the Heisenberg picture. As we introduced for the ideal Bose gas, the field operator

$$\hat{\psi} = \phi_0\hat{a}_0 + \sum_{k\neq 0}\phi_k\hat{a}_k \tag{2.13}$$

can be expressed[6] in terms of the single-particle wavefunctions ϕ_k. For a BEC with a macroscopic occupation number $\langle\hat{a}_0^\dagger\hat{a}_0\rangle \gg 1$ of the ground state we can introduce the Bogoliubov approximation [89]. Since the operators $\hat{a}_0$ and $\hat{a}_0^\dagger$ scale as $\sqrt{N_0}$ and their commutator is equal to one, we neglect the latter and replace these by the complex numbers $\sqrt{N_0}$. This way, the field operator

$$\hat{\psi} = \langle\hat{\psi}\rangle + \cancel{\delta\hat{\psi}} \approx \psi \tag{2.14}$$

is replaced by the classical field $\psi = \langle\hat{\psi}\rangle = \sqrt{N_0}\phi_0$, which is also called the order parameter. For low enough temperatures and interactions the non-condensed part $\delta\hat{\psi} = \sum_{k\neq 0}\phi_k\hat{a}_k$ vanishes, which is typically satisfied for experiments with BECs of ultracold atoms.

Application of the approximation to eq. (2.12) then directly yields the *dipolar Gross-*

[6] $\hat{a}_k^\dagger$ and $\hat{a}_k$ are the well-known bosonic creation and annihilation operators, which obey the commutation relations $[\hat{a}_i, \hat{a}_j^\dagger] = \delta_{ij}$ and $[\hat{a}_i, \hat{a}_j] = [\hat{a}_i^\dagger, \hat{a}_j^\dagger] = 0$.

Pitaevskii equation (dGPE)

$$i\hbar\,\partial_t\psi = \Big[-\frac{\hbar^2\nabla^2}{2m} + V_{\text{ext}} + g|\psi|^2 + \Phi_{\text{dd}}\Big]\psi \tag{2.15}$$

with the interactions given by eq. (2.10). In addition to the well-known result for contact-interacting particles [90, 91], we thereby introduce the dipolar interaction potential

$$\Phi_{\text{dd}}(\boldsymbol{r}) = \int \mathrm{d}\boldsymbol{r}'\, V_{\text{dd}}(\boldsymbol{r}-\boldsymbol{r}')|\psi(\boldsymbol{r}')|^2 \tag{2.16}$$

making the dGPE a non-local non-linear Schrödinger equation [61]. In other words, the quantum many-body problem reduces to a classical mean-field theory.

2.2.2. The extended Gross-Pitaevskii equation

The dGPE derived in the previous section is well-suited to describe the experiments with chromium condensates. In contrast, we observed stable quantum droplets with dysprosium, that were not predicted by the presented theory. In this case, both the contact and dipolar interaction are an order of magnitude higher[7] and the droplets have shorter lifetime pointing to an order-of-magnitude higher density compared to the condensate phase. For these reasons, we need to reconsider the previous assumption of weak interactions. In particular, we calculate a contribution due to the population of excited states and thus $\delta\hat{\psi} \neq 0$.

In lack of a more suited microscopic theory, we outline the derivation of these effects within Bogoliubov theory for a uniform gas. For this purpose, we assume a uniform gas in a volume V with a density $n = N/V$ and decompose the field operator $\hat{\psi} = \sum_p \hat{a}_{\mathbf{p}} V^{-1/2} e^{i\boldsymbol{p}\boldsymbol{r}/\hbar}$ in terms of plane wave single-particle states.

As elaborated in [60, ch. 4], the Bogoliubov transformation finally yields a Hamiltonian

$$\hat{H} = E_0 + \sum_{\boldsymbol{q}\neq 0} E(\boldsymbol{q})\hat{b}^\dagger_{\mathbf{q}}\hat{b}_{\mathbf{q}} \tag{2.17}$$

with the energy of the ground state E_0 and a set of *quasi-particles* with their corresponding destruction and creation operators $\hat{b}_{\mathbf{q}}$ and $\hat{b}^\dagger_{\mathbf{q}}$. This way, the physical system of interacting particles is described in terms of independent quasi-particles with energy $E(\boldsymbol{q})$ and quasi-momentum $\boldsymbol{q}$. We study the excitations of the homogeneous dipolar gas in ch. 2.3 and turn to the ground state, which corresponds to the vacuum of quasi-particles. The ground state

[7] In order to drive ^{52}Cr to the strongly dipolar regime $a_{\text{dd}} \gtrsim a_{\text{s}}$, the scattering length was decreased by an order of magnitude [33], cf. fig. (2.1b).

features a finite population of excited single-particle states, which is due to interactions. This *quantum depletion* Δn of the ground state density n results in a shift of the ground state energy E_0, and thus a modification of the chemical potential $\mu = \partial E_0/\partial N$ due to *quantum fluctuations*. For a contact-interacting gas we find

$$\frac{\Delta n}{n} = \frac{8}{3\sqrt{\pi}}\sqrt{n a_\mathrm{s}^3} \qquad \text{and} \qquad \Delta\mu = \frac{32}{3\sqrt{\pi}} g n \sqrt{n a_\mathrm{s}^3} \tag{2.18}$$

known as the Lee-Huang-Yang (LHY) correction [92]. Derived within Bogoliubov theory, this is the first-order correction, that also neglects interactions of quasi-particles. The next-order term $\Delta\mu \propto (n a_\mathrm{s}^3)\ln(n a_\mathrm{s}^3)$ was derived by considering three-particle collisions [93] and depends on the details of the short-range interaction.

In liquid helium, which is far from the weakly-interacting regime, the fraction of condensed atoms is only 7% due to quantum depletion [94]. Within the context of ultracold atoms, the quantum depletion is typically negligible and has only been recently measured quantitatively in a homogeneous BEC of ^{39}K [95]. In this experiment, the scattering length was tuned to $a_\mathrm{s} = 3000\, a_0$ close to a Feshbach resonance in order to increase the gas parameter to finite values $\sqrt{n a_\mathrm{s}^3} \lesssim 0.04$. For a typical quantum droplet with a gas parameter $\sqrt{n a_\mathrm{s}^3} \sim 0.01$ the expansion is thus applicable.

The generalization of eq. (2.18) to include the dipolar interaction [62, 63] yields

$$\frac{\Delta n}{n} = \frac{8}{3\sqrt{\pi}}\sqrt{n a_\mathrm{s}^3}\, Q_3(\varepsilon_\mathrm{dd}) \qquad \text{and} \qquad \Delta\mu = \frac{32}{3\sqrt{\pi}} g n \sqrt{n a_\mathrm{s}^3}\, Q_5(\varepsilon_\mathrm{dd}) \tag{2.19}$$

with the functions $Q_l = \frac{1}{2}\int_0^\pi \mathrm{d}\alpha\, \sin(\alpha)[1 + \varepsilon_\mathrm{dd}(3\cos^2\alpha - 1)]^{l/2}$ averaging the angular contribution of the DDI. For $\varepsilon_\mathrm{dd} \leq 1$ these are $Q_{3,5} \geq 1$ and develop a negligible imaginary part for $\varepsilon_\mathrm{dd} > 1$, pointing towards the destabilization due to a softened excitation spectrum, see ch. 2.3. We use the resulting quantum fluctuations term $\Delta\mu = \Delta\mu(\boldsymbol{r})$ within a *local-density approximation* (LDA), which yields

$$\Delta\mu(\boldsymbol{r}) = g_\mathrm{qf}|\psi(\boldsymbol{r})|^3 \quad \text{with} \quad g_\mathrm{qf} = \frac{32 g a_\mathrm{s}^{3/2}}{3\sqrt{\pi}}\left(1 + \frac{3}{2}\varepsilon_\mathrm{dd}^2\right) \tag{2.20}$$

and the series expansion of $Q_5(\varepsilon_\mathrm{dd}) \approx 1 + \frac{3}{2}\varepsilon_\mathrm{dd}^2$. Finally, we arrive at the *extended Gross-Pitaevskii equation* (eGPE)

$$i\hbar\,\partial_t\psi = \left[-\frac{\hbar^2\nabla^2}{2m} + V_\mathrm{ext} + g|\psi|^2 + \Phi_\mathrm{dd} + g_\mathrm{qf}|\psi|^3\right]\psi \tag{2.21}$$

that properly describes condensates of ultracold dysprosium atoms and gives rise to the physics of dipolar quantum liquids [48, 52–55]. Interestingly, we have introduced quantum fluctuations to a mean-field theory, which is intrinsically free of fluctuations.

Although there are no general solutions to this equation, we can study the homogeneous gas analytically. In ch. 2.3 we thereby derive the excitation spectrum, that gives rise to a variety of dipolar effects. Non-uniform gases can be described by an approximate method, the variational ansatz, which we thoroughly study in ch. 2.4. The starting point for this analysis is the energy functional

$$E[\psi] = \int \mathrm{d}\boldsymbol{r} \left[\frac{\hbar^2}{2m} |\nabla\psi|^2 + V_{\mathrm{ext}} |\psi|^2 + \frac{1}{2} g |\psi|^4 + \frac{1}{2} |\psi|^2 \Phi_{\mathrm{dd}} + \frac{2}{5} g_{\mathrm{qf}} |\psi|^5 \right] \tag{2.22}$$

of the eGPE. Using this method, we explore the properties of quantum droplets in ch. 2.4.3. In ch. 2.5 we present numerical simulations for an exact solution of the eGPE, which then yields additional insight on the density profiles and dynamics of the quantum gas.

In lower dimensions, the Lee-Huang-Yang correction has been studied for droplets of Bose-Bose mixtures [96] as well as in the crossover to the 3D regime [97]. For dipolar atoms, this has been investigated in a quasi-1D setting [98], while a description for the intermediate dimension is still lacking.

2.3. The homogeneous gas

Having developed a suitable description of ultracold dipolar atoms, we can use it to explore effects of the dipolar interaction. The most simple, yet instructive system is a homogeneous isotropic gas of atoms with a constant number density $n = N/V$. In such a system, the mean-field dipolar interaction of eq. (2.16) averages to zero. Nevertheless, there are various dipolar effects related to the excitation spectrum of the gas. In order to illustrate these in general, we restrict ourselves to small densities n, such that the fluctuation term derived in 2.2.2 is negligible.

2.3.1. Excitation spectrum

Within the famous Bogoliubov theory [89] the gas of weakly-interacting bosons is described as a system of non-interacting quasi-particles with energy $E(\boldsymbol{q})$ and quasi-momentum

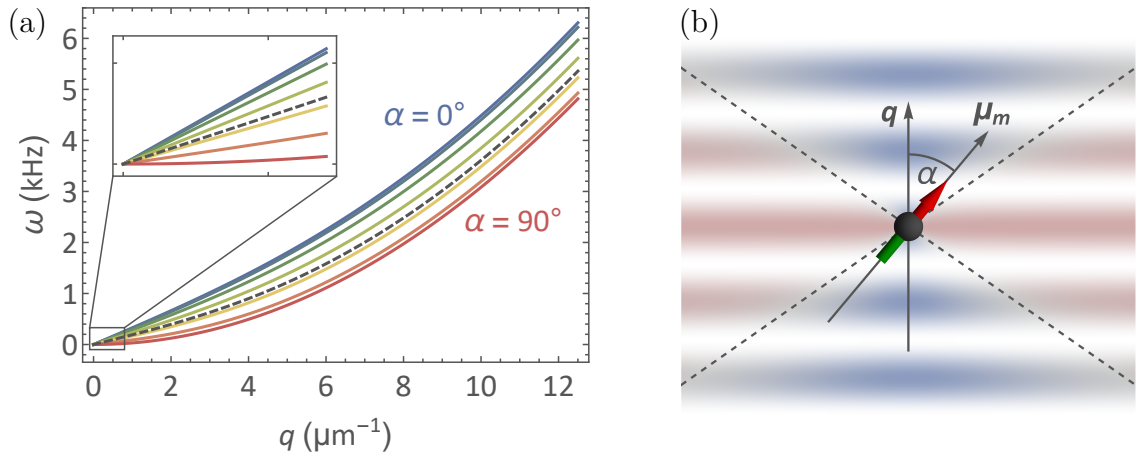

Figure 2.2.: **Bogoliubov excitation spectrum.** (a) The dispersion relation eq. (2.24) of a dipolar homogeneous gas depends on the angle α between the dipole axis $\boldsymbol{\mu_m}$ and an excitation with momentum $\boldsymbol{q}$. (b) Sketch of such an excitation $\boldsymbol{q}$. Density modulations with $\boldsymbol{q} \perp \boldsymbol{\mu_m}$ accumulate dipoles in an attractive configuration, thus "softening" the mode towards lower energy (red). For $\boldsymbol{q} \parallel \boldsymbol{\mu_m}$ the density modulation leads to a larger energy (blue). Dashed lines correspond to the magic angle α_m, where the dipolar interaction vanishes [99].

$\boldsymbol{q}$. The Bogoliubov excitation spectrum

$$E(\boldsymbol{q}) = \sqrt{\left(\frac{\hbar^2 q^2}{2m}\right)^2 + 2n\tilde{V}_{\text{int}}(\boldsymbol{q})\left(\frac{\hbar^2 q^2}{2m}\right)} \tag{2.23}$$

of these quasi-particles is determined by the fourier-transform $\tilde{V}_{\text{int}}(\boldsymbol{q})$ of a general two-body interaction potential $V_{\text{int}}(\boldsymbol{r})$. For a gas with contact and dipolar interaction, as considered here, we obtain

$$E_{\text{3D}}(q) = \hbar q \sqrt{\left(\frac{\hbar q}{2m}\right)^2 + \frac{gn}{m}\left[1 + \varepsilon_{dd}\left(3\cos^2\alpha - 1\right)\right]} \tag{2.24}$$

with the angle α between dipole axis $\boldsymbol{\mu_m}$ and quasi-momentum $\boldsymbol{q}$ [100]. We note, that a macroscopic approach based on the linearization of the hydrodynamic equations [61, ch. 5] around the equilibrium density and velocity yields the same result.

Similar to the contact-interacting case, that is recovered for $\varepsilon_{\text{dd}} = 0$, there is a transition from the quadratic free-particle regime with energy $\frac{\hbar^2 q^2}{2m}$ for large momenta to the linear *phonon* regime for $q \to 0$. Additionally, the dipolar interaction introduces an anisotropy of the excitation spectrum, as shown in fig. (2.2). For $\varepsilon_{\text{dd}} > 1$, the excitation spectrum becomes imaginary[8] for small momenta and is thus subject to the *phonon instability*,

[8] In fact, the numerical factor of a_{dd} in eq. (2.8) was chosen such that the gas is stable for $\varepsilon_{\text{dd}} \leq 1$.

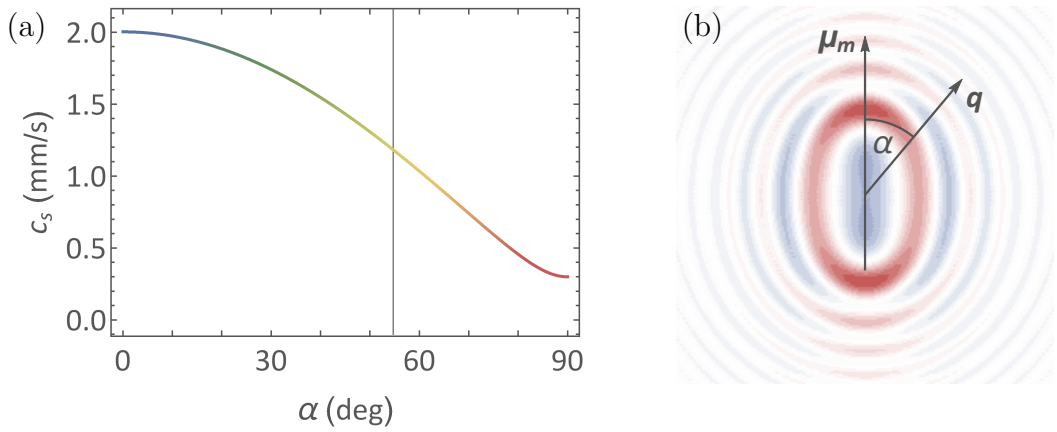

Figure 2.3.: **Speed of sound.** (a) Variation of the speed of sound $c_s(\alpha)$ of an excitation $\boldsymbol{q}$ defining the angle α with respect to the polarization axis $\boldsymbol{\mu_m}$. (b) Anisotropic sound waves emitted from a point-like excitation at the center. Higher and lower density compared to the undisturbed gas are shown in blue and red, respectively [99].

which is known from condensates with attractive contact interaction $g < 0$.
In the long-wavelength limit we can define the speed of sound

$$c_s(\alpha) = \lim_{q\to 0} \frac{E_{3D}(q)}{q} = \sqrt{\frac{gn}{m}}\sqrt{1 + \varepsilon_{dd}\left(3\cos^2\alpha - 1\right)} \tag{2.25}$$

of the gas, which is shown in fig. (2.3a). A consequence of the excitation spectrum of eq. (2.24) is the emission of anisotropic sound waves after a point-like perturbation[9] of the homogeneous gas, as demonstrated in fig. (2.3b). Experimentally, the anisotropic excitation spectrum has been confirmed via Bragg spectroscopy of a chromium condensate with $\varepsilon_{\mathrm{dd}} = 0.15$ [101].

2.3.2. Healing length and vortices

The transition of phonon to free-particle behavior in the excitation spectrum of eq. (2.24) occurs at a specific momentum[10] and thus introduces a characteristic length scale

$$\xi = \frac{1}{q} = \frac{\hbar}{\sqrt{2}m\, c_s(a)} \tag{2.26}$$

[9] A δ-like perturbation in real space leads to an excitation of all momenta. Higher momenta with smaller anisotropy propagate faster and are thus further away from the center.

[10] The expansion of eq. (2.24) for large momenta yields $E_{3D} \approx \frac{\hbar^2 q^2}{2m} + mc_s^2$. Setting both terms equal leads to the definition of ξ.

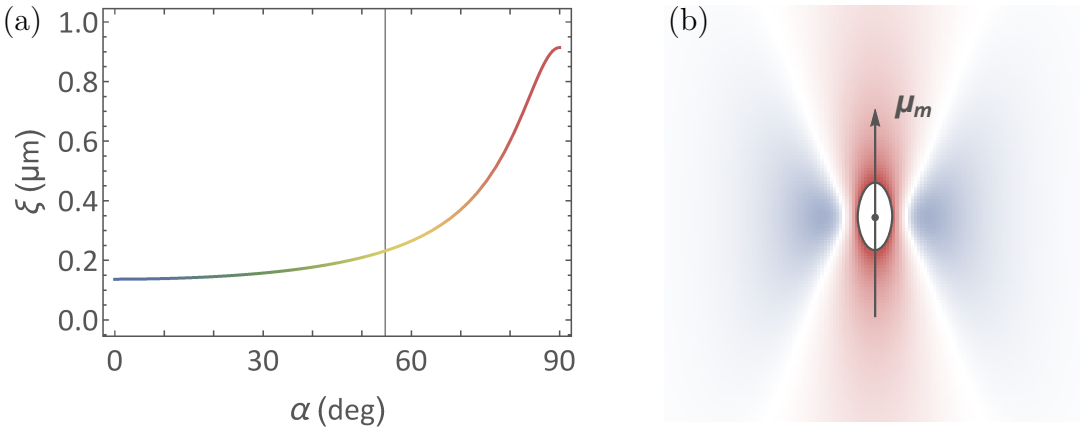

Figure 2.4.: **Healing length.** (a) Plot of the healing length $\xi(\alpha)$ in momentum space according to eq. (2.26). (b) In real space a defect with size $R \ll \xi$ has an anisotropic core (solid line $0.90\,n$) with long-range deformation of the condensate over several ξ. Along the dipole axis $\boldsymbol{\mu_m}$ the density is lower (red) and perpendicular to it the density is higher (blue) compared to the unperturbed condensate [99].

for the interaction in the system, the so-called *healing length*. This is the characteristic scale over which the condensate density distribution "heals" from a local defect, e.g. the edge of a box potential [60, ch. 11.1]. The anisotropy of eq. (2.26) in momentum space leads to a modification of this healing length in real space.

In fig. (2.4) we demonstrate this behavior with a line-like perturbation[11] of the homogeneous condensate. The core around this defect becomes elongated along the dipole axis $\boldsymbol{\mu_m}$. Compared to the unperturbed gas the long-range DDI leads to a decreased density (red) along this axis and increased density (blue) perpendicular to it. Both features extend over several healing lengths and thus induce an anisotropic long-range interaction between defects.

The most prominent example of such defects are quantized vortices in rotating superfluids [60, ch. 5.3]. In the case of non-dipolar condensates the healing length and therefore the vortex core are isotropic. While vortices [18] and vortex lattices [102] have been observed for contact-interacting condensates, dipolar effects of vortices have not been measured up to now. Yet, the deformation of the vortex core [103] and anisotropic long-range interactions between vortices [104], which would lead to vortex patterns with symmetries [103, 105] other than the triangular Abrikosov pattern [106], have been predicted. In ch. 7.2, we investigate the feasibility to observe such effects in our experiment.

[11] A repulsive cylindrical Gaussian potential with radius $R \ll \xi$ perpendicular to the image plane.

2.3.3. Superfluidity and Landau's criterion

In an attempt to explain the superfluidity of liquid helium [12], L. Landau established the seminal connection of the liquid's excitation spectrum and the dissipation in the fluid [107]. This allows us to examine how the excitation spectrum of a dBEC influences the superfluid properties.

For this purpose, we consider an impurity with mass m moving with velocity $\boldsymbol{v}$ in a superfluid. The onset of dissipation is caused by the creation of a single elementary excitation with energy $E(\boldsymbol{q})$ and quasi-momentum $\boldsymbol{q}$ in the fluid. Thus the initial energy and momentum of the impurity

$$\boldsymbol{p}_0 = m\boldsymbol{v} \qquad \text{and} \qquad E_0 = \frac{p_0^2}{2m} = \frac{1}{2}mv^2 \tag{2.27}$$

become

$$\boldsymbol{p}_1 = m\boldsymbol{v} - \boldsymbol{q} \qquad \text{and} \qquad E_1 = \frac{p_1^2}{2m} + E(\boldsymbol{q}) = \frac{1}{2}mv^2 - \boldsymbol{v}\cdot\boldsymbol{q} + \frac{q^2}{2m} + E(\boldsymbol{q}) \tag{2.28}$$

after the excitation process. With the total energy conserved by this process we obtain the relation $\boldsymbol{v}\cdot\boldsymbol{q} = E(\boldsymbol{q})$ under the assumption of a heavy impurity with $m \to \infty$.

Assuming an isotropic fluid, for which velocity $\boldsymbol{v}$ and momentum $\boldsymbol{q}$ are collinear, we arrive at $v = E(\boldsymbol{q})/q$, which is valid for all q. By minimization of the right-hand side with respect to momentum q, we define the critical velocity v_c, which is the lowest v satisfying the equation. This leads to the famous *Landau criterion*

$$v > v_\mathrm{c} = \min_q \left(\frac{E(\boldsymbol{q})}{q} \right) \tag{2.29}$$

for the onset of dissipation in the superfluid. Thereby it becomes evident, that the acquired critical velocity is determined by the excitation spectrum $E(\boldsymbol{q})$ of the fluid. In the case of a non-interacting BEC ($g = \varepsilon_\mathrm{dd} = 0$) the spectrum of eq. (2.24) reduces to the one of a free-particle $E(q) = \frac{\hbar^2 q^2}{2m}$, which yields a critical velocity of zero. A non-interacting BEC is therefore not superfluid, since any moving impurity causes dissipation. In contrast, a contact-interacting BEC ($g > 0, \varepsilon_\mathrm{dd} = 0$) features a critical velocity equal to the speed of sound c_s of eq. (2.25) and is therefore superfluid.

As shown in the previous section, the dipolar excitation spectrum is anisotropic. Consequently, the direction of flow $\boldsymbol{v}$ and quasi-momentum $\boldsymbol{q}$ do not necessarily coincide [108].

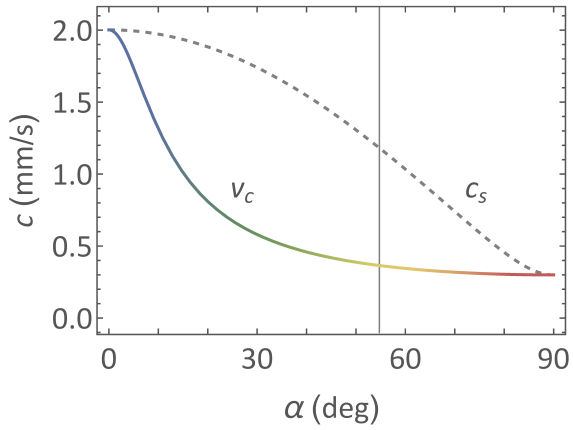

Figure 2.5.: **Critical velocity.** Angular dependence of critical velocity $v_c(\alpha_v)$ in eq. (2.32) (solid) derived via the generalized Landau criterion and the speed of sound in the gas $c_s(\alpha_q)$ in eq. (2.25) (dashed). They both coincide only for directions parallel and perpendicular to the magnetic field with the critical velocity being lower in general. The vertical line marks the magic angle [99].

Therefore we decompose $\boldsymbol{v} = v \cdot \hat{\boldsymbol{v}}$, which leads to the generalized form

$$v > v_c = \min_{\boldsymbol{q}} \left(\frac{E(\boldsymbol{q})}{\hat{\boldsymbol{v}} \cdot \boldsymbol{q}} \right) \tag{2.30}$$

of the Landau criterion. Here, the minimization additionally covers all possible directions of momentum $\boldsymbol{q}$. Like the dipolar interaction the presented dispersion relation eq. (2.24) has rotational symmetry. Therefore the final expression only depends on the angle α_v of $\hat{\boldsymbol{v}}$ with respect to the polarisation axis $\hat{\boldsymbol{z}}$. Similarly, we define $\alpha_q = \alpha$ of $\boldsymbol{q}$ with respect to $\hat{\boldsymbol{z}}$. Since the dispersion relation of a stable condensate ($\varepsilon_{\mathrm{dd}} \leq 1$) is monotonic the problem simplifies to the minimization of the angle-dependent part

$$\frac{\sqrt{1 + \varepsilon_{dd} \left(3 \cos^2 \alpha_q - 1\right)}}{\cos\left(\alpha_v - \alpha_q\right)} \tag{2.31}$$

with respect to α_q, which yields

$$\frac{1}{v_c(\alpha_v)^2} = \frac{\sin(\alpha_v)^2}{c_\perp^2} + \frac{\cos(\alpha_v)^2}{c_\parallel^2} \tag{2.32}$$

with the speed of sound $c_\parallel = c_s(0\,\mathrm{deg})$ and $c_\perp = c_s(90\,\mathrm{deg})$ [108]. Therefore the critical velocity only coincides with the speed of sound for flow directions $\hat{\boldsymbol{v}}$ parallel ($\alpha_v = 0\,\mathrm{deg}$) or orthogonal ($\alpha_v = 90\,\mathrm{deg}$) to the polarization axis and is lower for intermediate angles.

The angular dependence is shown in fig. (2.5), where the critical velocity is compared to the speed of sound.
This result is analogous to the propagation of light in an uniaxial birefringent crystal [109, ch. 6.3.]. For an extraordinary ray the direction of momentum $\hat{\boldsymbol{k}}$ and group velocity $\hat{\boldsymbol{v}}$ differ in general, which is equivalent to the case here and also leads to eq. (2.32). The underlying mechanism is the minimization of the optical path length in an anisotropic medium due to Fermat's principle.

2.3.4. Roton excitations

While the previous section covers the critical velocity due to the excitation of phonons in a homogeneous gas, the properties of excitations are profoundly changed when the gas is confined in one direction. This leads to a distinct excitation spectrum, first discovered in ref. [110].
In the following, we develop the excitation spectrum for a quasi-two-dimensional (quasi-2D) gas along the lines of [111, 112]. For this purpose we add a harmonic trapping potential $V_{\text{ext}} = \frac{1}{2}m\omega_z^2 z^2$ along the polarization axis $\hat{\boldsymbol{z}}$, which introduces a length scale $l_z = \sqrt{\hbar/m\omega_z}$, known as the harmonic oscillator length, to the system. For strong confinement compared to the chemical potential $\mu = (g + 2g_{\text{dd}})n \ll \hbar\omega_z$ the condensate is in the quasi-2D regime and thus restricted to the harmonic oscillator ground state, where excitations along this direction are exponentially suppressed. Unlike the case for a real 2D system, there is still a finite extent l_z along the polarization axis. Averaging the momentum-space dipolar interaction of eq. (2.10) along this axis[12] then yields the dipolar interaction

$$\tilde{V}_{\text{dd}}^{\text{2D}}(q_\perp) = \frac{g_{\text{dd}}}{\sqrt{2\pi}l_z} F_\perp\left(\frac{q_\perp l_z}{\sqrt{2}}\right) \tag{2.33}$$

for in-plane excitations with momentum $q_\perp$ and we introduced

$$F_\perp(x) = 2 - 3\sqrt{\pi}x \exp(x^2)\operatorname{erfc}(x) \tag{2.34}$$

depending on the complementary error function $\operatorname{erfc}(x) = 2\pi^{-1/2}\int_x^\infty \mathrm{d}t \exp(-t^2)$. The function $F_\perp(x)$ monotonously decreases from a value of $F_\perp(0) = 2$ via $F_\perp(1/\sqrt{2}) = 0$ to

[12] For the density we choose an ansatz of form $n(\boldsymbol{r}) = n(\rho)\exp(-z^2/l_z^2)/\sqrt{\pi}l_z$ with polar coordinate ρ. We then calculate the interaction energy $E_{\text{int}} = \frac{1}{2(2\pi)^3}\int \mathrm{d}^3q\, \tilde{n}(\boldsymbol{q})\tilde{V}_{\text{dd}}(\boldsymbol{q})\tilde{n}(-\boldsymbol{q})$ in momentum space to make use of the convolution theorem. The separation of axial and transversal components q_z and $q_\perp$, respectively, in the density $\tilde{n}(\boldsymbol{q}) = \tilde{n}(q_\perp)\exp(-q_z^2 l_z^2/4)$ and the interaction potential $3\cos(\alpha)^2 - 1 = 3q_z^2/(q_z^2 + q_\perp^2) - 1$ then yields eq. (2.33) under the remaining transversal integral after subsequent integration along the q_z axis.

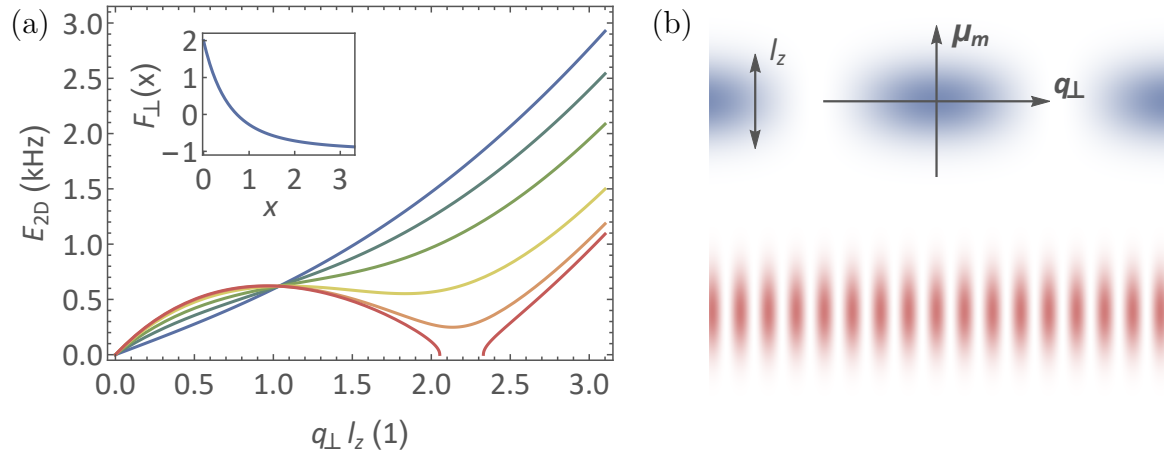

Figure 2.6.: **Excitation spectrum of a quasi-two-dimensional gas.** (a) Excitation energy E_{2D} over in-plane quasi-momentum $q_\perp$ of eq. (2.35) for ε_{dd} values of 0, 1, 2, 3, 3.4 and 3.5 (blue to red) [99]. For increasing ε_{dd} the Roton-Maxon spectrum, a distinct local maximum and minimum at finite momentum, develops. For larger dipolar interaction this mode becomes unstable. The inset shows eq. (2.34), describing the dependence of the dipolar interaction on the reduced momentum $x = q_\perp l_z/\sqrt{2}$. (b) Schematic of a phonon with $x \ll 1$ (top) or $x \gg 1$ (bottom), where dipoles are accumulated in a predominantly repulsive and attractive configuration, respectively. This effect is the reason to a hardening and softening in the excitation spectrum.

-1 for $x \to \infty$, as shown in the inset of fig. (2.6a). Consequently, the dipolar interaction $\tilde{V}_{dd}^{2D}$ depends on the modulus of the in-plane quasi-momentum $q_\perp$ and becomes attractive for $q_\perp > \sqrt{2}/l_z$. In analogy to the picture in fig. (2.2b) for the homogeneous case, we can understand this effect in terms of an accumulation of dipoles in an attractive configuration in real space, as illustrated in fig. (2.6b). With such dipolar interaction the excitation spectrum reads

$$E_{2D}(q_\perp) = \hbar q_\perp \sqrt{\left(\frac{\hbar q_\perp}{2m}\right)^2 + \frac{g n_0}{m}\left[1 + \varepsilon_{dd}\, F_\perp\left(\frac{q_\perp l_z}{\sqrt{2}}\right)\right]}\,. \tag{2.35}$$

with the peak density $n_0 = n_{2D}/\sqrt{2\pi} l_z$ defined by the in-plane density n_{2D}. Considering the phonon instability for $q_\perp \to 0$, we acquire the stability criterion $g + 2g_{dd} > 0$. Thus, the dipolar interaction can stabilize the gas against an attractive contact interaction and for the case of $\varepsilon_{dd} \gg 1$ against a phonon or global collapse.

In comparison to the monotonous dispersion relation eq. (2.24) of the homogeneous gas the behavior here is conceptually different due to the dependence on the modulus of momentum $q_\perp$. As can be seen in fig. (2.6a), for a certain range of ε_{dd} values the spectrum develops a peculiar shape featuring a local minimum and maximum resembling the *Roton-*

Maxon spectrum of liquid helium [107, 110, 113]. In particular, the quasi-particle related to the local minimum of the excitation spectrum is called a *roton*. For larger $\varepsilon_{\mathrm{dd}}$, the excitation spectrum becomes imaginary, indicating an additional finite-wavelength instability, leading to a local collapse of the gas. This is a very intriguing feature of dipolar condensates, since the roton introduces a natural length scale for self-organization of the system. Unfortunately, such density wave states are not stable within mean-field theory [114].

Although derived for a quasi-2D gas here, the softening of excitations due to confinement is a general feature. An illustrative example are classical ferrofluids, that consist of suspended ferromagnetic particles. When magnetized by an external magnetic field surface excitations become soft [115], which leads to the *Rosensweig instability* and subsequent pattern formation [116, 117]. In the realm of ultracold gases, there are extensive numerical studies for finite-size condensates with weak three-dimensional confinement (i. e. $\mu \gg \hbar\omega_k$ with $k = x, y, z$). Condensates with radial symmetry can have biconcave density distributions, with softened *angular roton* modes featuring non-zero angular momentum [118, 119]. Such excitations lead to the spontaneous symmetry breaking during the collapse dynamics [120, 121].

In the droplet experiments presented in [1, 2, 4, 5], this effect leads to a modulational instability followed by fragmentation of the condensate into multiple quantum droplets. The population of a roton mode prior to the collapse dynamics was experimentally confirmed by the observation of finite-momentum peaks in time-of-flight measurements of quenched dipolar erbium condensates [122]. Both experiments are subject to highly non-trivial dynamics, that strongly deviates from the case of weak perturbations on top of a uniform gas, as presented in this section. Therefore a full numerical treatment including finite-size effects and dynamics is needed to describe the actual experiments, which we are going to introduce in section 2.5.

Recalling the Landau criterion in eq. (2.29), the critical velocity of a superfluid is determined by its excitation spectrum. In a similar way as initially predicted by Landau [107] and later measured [113] for liquid helium, the critical velocity for the quasi-2D dipolar gas is determined by the excitation of a roton[13]. In both systems the critical velocity is thus lower compared to the speed of sound given by the phonon branch. For a dipolar gas, the reduction of the critical velocity due to the softening of a roton mode was pointed out in [123]. When tilting the magnetic field towards the plane of the quasi-2D condensate, the excitation spectrum additionally becomes anisotropic, as mentioned in the previous section, and is still influenced by the roton mode [124].

[13] Given that the dipolar interaction is sufficiently strong, such that $E(q)/q$ for the phonon ($q \to 0$) is larger than for the roton mode, see eq. (2.29).

2.4. The trapped gas: Variational Method

In the previous section we have introduced the concept of confinement, that modifies the properties of the system. Experimentally, quantum gases are typically trapped by focused laser beams, which are well-approximated by a three-dimensional harmonic potential [125]. In the following, we develop a framework to describe both the ground state and dynamics based on the eGPE in eq. (2.21) with an external trapping potential of the form

$$V_{\text{ext}}(r,z) = \frac{1}{2}m(\omega_r^2 r^2 + \omega_z^2 z^2) \tag{2.36}$$

characterized by radial and axial trapping frequencies ω_r and ω_z. Owing to the radial symmetry of the dipolar interaction with respect to the $\boldsymbol{\mu_m} \parallel \hat{\boldsymbol{z}}$ axis, we can restrict the analysis to the radially-symmetric case. Since there are no exact analytical solutions of the eGPE with a harmonic potential, we resort to an approximate analytical approach, the *variational ansatz*. With this method, we exploit the physics of dipolar BECs. Introducing quantum fluctuations then leads to the description of dipolar quantum droplets in the subsequent section.

2.4.1. Variational Ansatz

In the interaction-dominated regime condensates become large, the density profile varies smoothly, and kinetic energy can be neglected. This is known as the *Thomas-Fermi* approximation, which leads to an inverted parabola for the density distribution, that can be derived analytically [60, ch. 11.2]. While a typical dysprosium BEC in our experiment is well-described by this approach, we aim for a description that suits both BEC and quantum droplets. For the latter, the radial size is on the order of the healing length and kinetic energy cannot be neglected.

Another possibility is a gaussian density distribution, which is the exact solution for a non-interacting BEC in a harmonic trap [126]. This ansatz includes the kinetic energy and is thus a good approximation for small interactions. For this method, we insert a gaussian trial wavefunction of the form

$$\psi_{\text{g}}(r,z) = \sqrt{\frac{N}{\pi^{3/2}\sigma_r^2\sigma_z}}\exp\left(-\frac{r^2}{2\sigma_r^2} - \frac{z^2}{2\sigma_z^2}\right) \tag{2.37}$$

in the energy functional eq. (2.22) of the eGPE, such that we obtain the total energy of

the condensate

$$E(\sigma_r, \sigma_z) = \frac{1}{4} N \frac{\hbar^2}{m} \left[2\sigma_r^{-2} + \sigma_z^{-2}\right] + \frac{1}{4} N m \left[2\omega_r^2 \sigma_r^2 + \omega_z^2 \sigma_z^2\right] + \frac{1}{2(2\pi)^{3/2}} \frac{g N^2}{\sigma_r^2 \sigma_z} \left[1 - \varepsilon_{\mathrm{dd}} f\left(\frac{\sigma_r}{\sigma_z}\right)\right] + \frac{2^{5/2}}{5^{5/2}\pi^{9/4}} \frac{g_{\mathrm{qf}} N^{5/2}}{(\sigma_r^2 \sigma_z)^{3/2}} \tag{2.38}$$

depending on the two variational parameters σ_r and σ_z [53, 55]. The contributions, in order, are due to the quantum pressure, harmonic potential, contact & dipolar interactions, and quantum fluctuations. This way, the non-local term Φ_{dd} of the dipolar interaction in eq. (2.21) reduces to an analytical geometry-dependent function

$$f(\kappa) = \frac{1 + 2\kappa^2}{1 - \kappa^2} - \frac{3\kappa^2 \operatorname{arctanh}\left(\sqrt{1 - \kappa^2}\right)}{(1 - \kappa^2)^{3/2}}, \tag{2.39}$$

which only depends on the aspect ratio $\kappa = \sigma_r/\sigma_z$ of the cloud [75, 127]. As shown in fig. (2.7a), this function decreases monotonously from $f(\kappa \to 0) = 1$ with a largely attractive dipolar interaction to $f(\kappa \to \infty) = -2$, where the interaction is repulsive. Minimization of $E(\sigma_r, \sigma_z)$ with respect to the variational parameters then yields an approximate solution of the ground state. With this approach the shape of the density distribution is fixed and thus the choice of the trial function influences the deviation from the real ground state. Nevertheless, it yields important qualitative insight, as we are going to show in the subsequent sections.

The variational approach presented here was successfully used to describe the ground state properties [128] and collective excitations [129, 130] of the first contact-interacting BECs. Later, it was extended to include the dipolar interaction [80, 131, 132], and more recently, quantum fluctuations [62, 63]. Finally, this method has proven useful to study the ground state and excitations of quantum droplets [52, 53, 55].

2.4.2. Dipolar BECs: Magnetostriction and Instability

In this section, we demonstrate general effects of the dipolar interaction on a trapped BEC, which were observed in seminal studies on ^{52}Cr dBECs in our group [31–35].

The dipolar interaction leads to a dependence of the total energy in eq. (2.38) on the function $f(\kappa)$ in eq. (2.39), with $\kappa = \sigma_r/\sigma_z$ being the cloud aspect ratio. In general, states with $\kappa < 1$ have lower energy compared to a condensate with contact interactions only, where the aspect ratio of trap λ and cloud κ are equal. With the dipolar interaction, the minimization of eq. (2.38) to find the ground state then yields $\kappa < \lambda$, which is shown

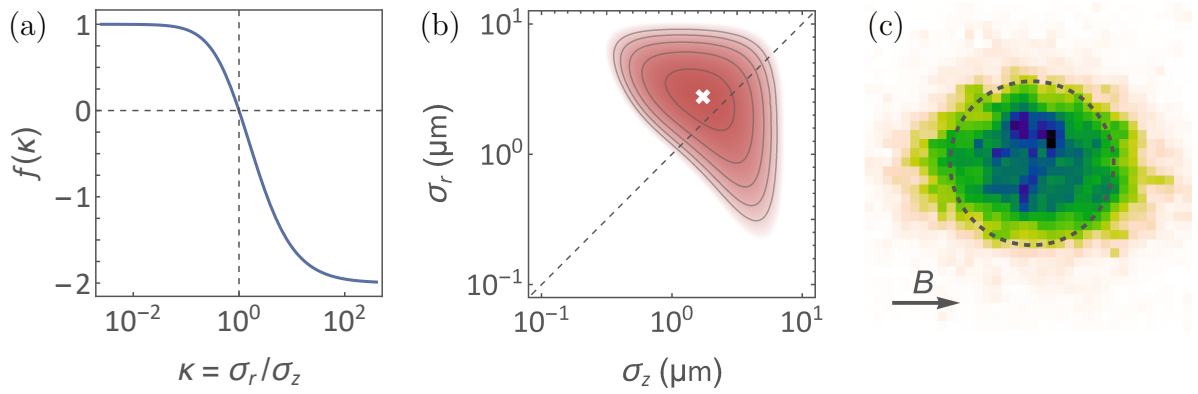

Figure 2.7.: **Magnetostriction of a dBEC.** (a) Structure function f of eq. (2.39) over cloud aspect ratio $\kappa = \sigma_r/\sigma_z$. Values $\kappa \ll 1$ correspond to a cigar-shaped cloud, where the averaged dipolar interaction is attractive and $f \to 1$. For pancake-shaped condensates ($\kappa \gg 1$) it is repulsive and $f \to -2$. (b) Energy landscape $E(\sigma_r, \sigma_z)$ of eq. (2.38) with a local minimum (white cross) at $\sigma_r = 1.7\,\mu\text{m}$ and $\sigma_z = 2.8\,\mu\text{m}$ in a spherical trap [99]. With an aspect ratio $\kappa \approx 0.6$ the cloud is elongated along the magnetic field compared to the isotropic case ($\kappa = 1$, dashed line). (c) Magnetostriction of a ^{162}Dy BEC in the experiment. The trapping potential is isotropic in the imaging plane (indicated by the dashed circle), and the cloud extends along the magnetic field.

in fig. (2.7b). Accordingly, the dipolar interaction leads to an elongation of the condensate along the magnetic field. This effect is called *magnetostriction* and can be observed in situ in our experiment, see fig. (2.7c). The relation $\kappa(\lambda)$ between cloud and trap aspect ratio is non-trivial. In fig. (2.8a) we show the ratio κ/λ for $N = 10^4$ atoms (blue) and in the limit of $N \to \infty$ (red). The deviation from the isotropic case $\kappa = \lambda$ is strongest around $\lambda = 1$.

A consequence of magnetostriction is the modification of the stability criterion $\varepsilon_{\text{dd}} < 1$, which we derived in ch. 2.3.1 for the homogeneous gas. In fig. (2.8b), we show the critical scattering length a_{crit} for the stability of the dBEC in an anisotropic trap with trap aspect ratio λ. For scattering lengths below this value, the minimum in eq. (2.38) vanishes and the gas collapses, since the two-body interactions become attractive. Experimentally, magnetostriction during the time-of-flight dynamics [32, 33] and the trap-dependent stability [34, 133] have been observed in seminal studies on ^{52}Cr dBECs in our group. In addition, a so-called *d-wave collapse* characterized by a transient cloverleaf-like density distribution was observed after a quench to an unstable scattering length $a_s < a_{\text{crit}}$ [35]. For the stability diagram in fig. (2.8b) we restricted the calculation to the mean-field interactions, i.e. neglected quantum fluctuations ($g_{\text{qf}} = 0$), to reproduce the mentioned chromium results. There, the dipolar interaction is weaker ($a_{\text{dd}} = 16\,a_0$) compared to

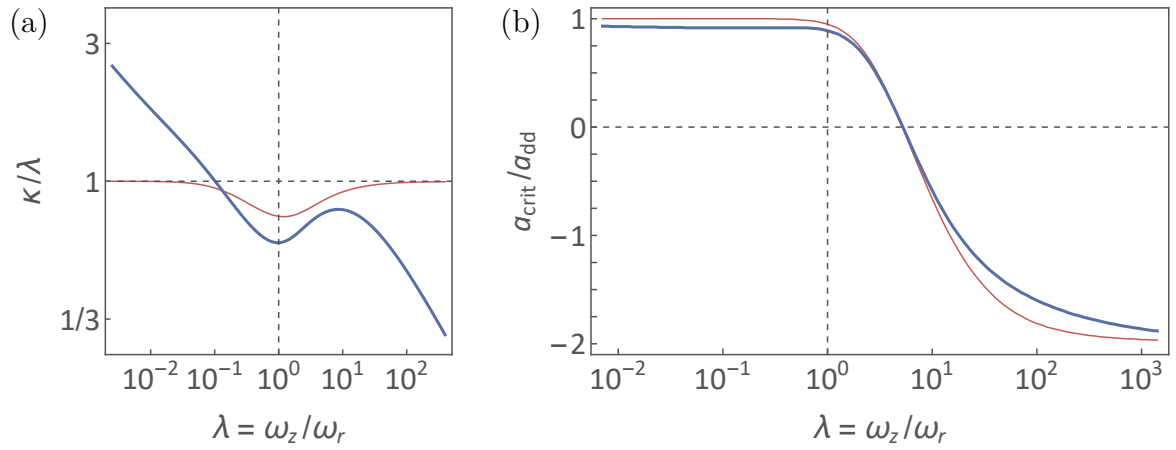

Figure 2.8.: **Instability in an anisotropic trap.** (a) Cloud aspect ratio κ over trap aspect ratio λ for $N = 10^4$ atoms (blue) and in the $N \to \infty$ (red) limit. Magnetostriction is pronounced for isotropic traps around $\lambda = 1$ and strongly depends on the atom number. (b) On the mean-field level, the deformation leads to an instability depending on the trap aspect ratio κ. For a scattering length a_s below the critical value a_crit a dipolar BEC collapses [99].

dysprosium and a Feshbach resonance was used to lower the scattering length a_s to a comparable value [33, 134]. Increasing with both interaction parameters, the quantum fluctuations are far too weak and can safely be neglected for the density range probed in these experiments.

2.4.3. Quantum Droplets

Compared to chromium, dysprosium has a larger magnetic moment and mass, which leads to a dipolar length a_dd, that is an order of magnitude larger. Naturally, a dysprosium condensate is in the regime where scattering length a_s and dipolar length are comparable, without the need for a Feshbach resonance to tune the former. This leads to stronger quantum fluctuations, that become important at accessible number densities on the order of $10^{21}\,\mathrm{m}^{-3}$. In the following, we explore the *dipolar quantum droplets* that emerge from the interplay of mean-field interactions and quantum fluctuations. The variational method is also suited to derive some basic droplet properties and compare them to a normal dBEC [52, 53, 55].

Figure (2.9a, c) show the energy landscapes of eq. (2.38) for various scattering lengths in a trap with an aspect ratio $\lambda = 1$ (a) and 3 (c). Comparing the ground state solutions (white cross) for $a_s = 100\,a_0$ (top), we find that the condensate aspect ratio is modified by the trap, as explained in the previous section. When the scattering length is decreased to $50\,a_0$ (bottom), both solutions for the different traps have shifted to smaller radial

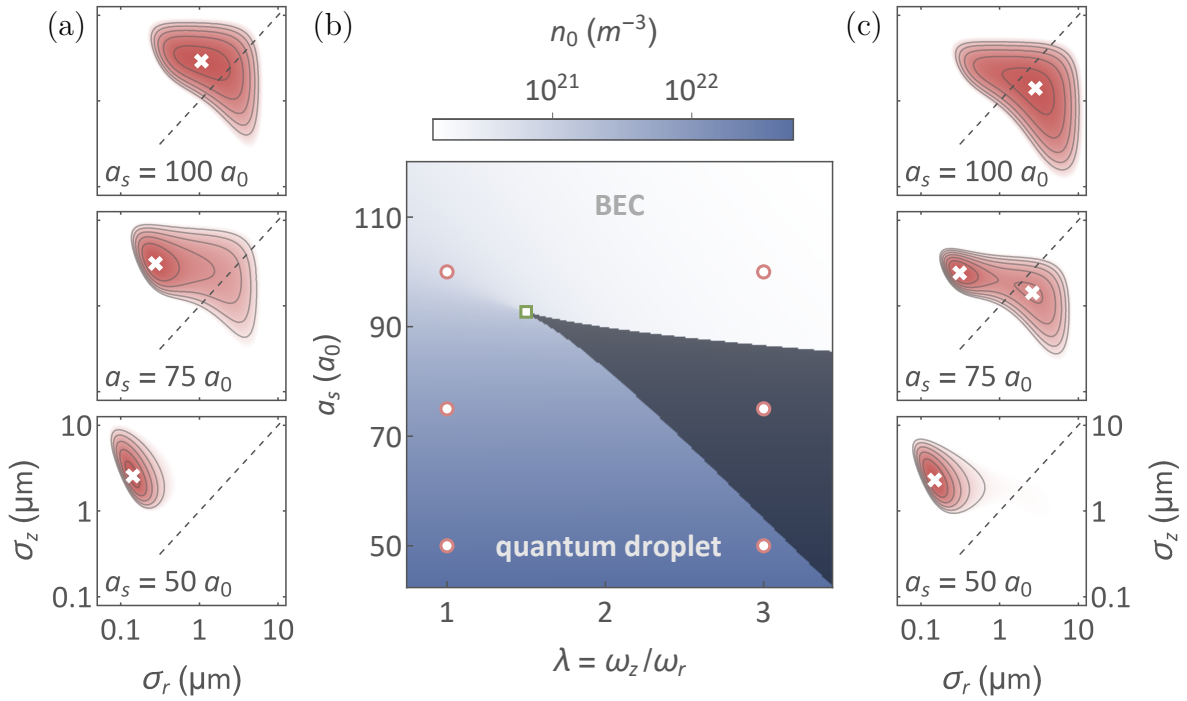

Figure 2.9.: **BEC and droplet solutions with the variational ansatz.** (a,c) Energy landscapes $E(\sigma_r, \sigma_z)$ of eq. (2.38) for various scattering lengths and a trap aspect ratio $\lambda = 1$ (a) or $\lambda = 3$ (c), respectively. Local minima are marked with a white cross. (b) Peak density n_0 of the ground state solution given by these minima. For $\lambda > \lambda_c$ there exists a bistable region with two local minima (dark area). The critical point (green rectangle) is located at $\lambda_c = 1.5, a_c = 93\,a_0$. For $\lambda < \lambda_c$ there is a crossover from the BEC ($a > a_c$) to the droplet ($a < a_c$) regime. In the bistable region, the transition from BEC to droplet is associated with a discontinuous peak density [99].

size σ_r, while having a comparable axial size σ_z. This is the quantum droplet state, that has more than an order of magnitude larger density compared to a BEC. In this regime characterized by $\varepsilon_{\mathrm{dd}} > 1$ and $\kappa = \sigma_r/\sigma_z \ll 1$, the dipolar interaction is stronger than the contact interaction, which results in an attractive residual two-body interaction. The latter is compensated by the quantum fluctuation term. This behavior is in stark contrast to a dBEC, where the residual two-body interaction is repulsive and gets compensated by the trapping potential. This fundamental difference makes the droplets liquid-like, which we are going to investigate later. For now, we note that the solution is almost independent of the surrounding trapping potential. Interestingly, in the intermediate regime (exemplified for $a_{\mathrm{s}} = 75\,a_0$) the solutions for both trap parameters are qualitatively different. When lowering the scattering length, the computed local minimum continuously shifts to smaller radial size for $\lambda = 1$. In the case for $\lambda = 3$ two local minima of the energy

functional coexist indicating a bistability. The peak density n_0 for the acquired solutions is shown in fig. (2.9b). The bistability (dark region) exists above a critical trap aspect ratio $\lambda_c = 1.5$ (green rectangle, critical scattering length $a_c = 93\,a_0$), with a value depending on parameters like atom number and mean trapping frequency [99].

Experimentally, we encountered multiple droplets [1] after a quench of the scattering length from a stable BEC with $a_s > a_c$ (white region) into the bistable regime $a_s < a_c$ (dark region) in a $\lambda = 3$ trap. There, the quantum gas is subject to a modulational instability, which is a dynamic effect and cannot be reproduced by an ansatz with a single gaussian wavefunction. For the full description and dynamics, we therefore resort to numerical studies of the eGPE, that are described in ch. 2.5. By performing such quench experiments for various values of λ, we measured the critical aspect ratio $\lambda_c = 1.87(14)$ for $N = 6000$ dysprosium atoms in a comparable trap [6]. This value is in agreement with simulations yielding $\lambda_c = 2.0$ for these parameters. By reshaping the trap to $\lambda < \lambda_c$ prior to the lowering of the scattering length, we can exploit the crossover to create single droplets deterministically in the experiment. This was a requirement to observe self-bound droplets [3], which we are going to describe in ch. 6. As mentioned, this discussion only covers a single smooth wavefunction. For the description of ground states with multiple droplets [5], we extended the variational ansatz presented here to two droplets, see ch. 4.

For now, we focus on the qualitative differences between the BEC (where we choose e.g. $a_s = 140\,a_0$) and droplet ($a_s = 70\,a_0$) in fig. (2.10a) showing the mentioned crossover region for $\lambda = 1$. For the droplet, the peak density n_0 is an order of magnitude larger, owing to a smaller radial size σ_r. The main difference lies in the energy contributions to the total energy E_{tot}, which we separate in single-particle contributions $E_1 = E_{\mathrm{kin}} + E_{\mathrm{ext}}$ of quantum pressure and external potential, the mean-field interactions $E_2 = E_{\mathrm{con}} + E_{\mathrm{dip}}$ given by both contact and dipolar interaction, and the beyond mean-field contribution E_{qf}. As shown in fig. (2.10b), the total energy $E_{\mathrm{tot}}/N = 22\,\mathrm{nK}$ of the BEC is positive and we obtain a dominant single-particle contribution $E_1 = 0.63\,|E_{\mathrm{tot}}|$, a minor contribution $E_2 = 0.33\,|E_{\mathrm{tot}}|$ from interactions and a negligible beyond-mean-field correction $E_{\mathrm{qf}} = 0.04\,|E_{\mathrm{tot}}|$. A positive interaction energy E_2 points to an on average repulsive interaction. In contrast, owing to the higher density and smaller aspect ratio, the interactions in a quantum droplet are attractive and dominant with $E_2 = -5.1\,|E_{\mathrm{tot}}|$. This value is almost compensated by quantum fluctuations with $E_{\mathrm{qf}} = +3.2\,|E_{\mathrm{tot}}|$, while the single-particle contribution $E_1 = +0.9\,|E_{\mathrm{tot}}|$ has a minor role. Although argued before, here it becomes evident, that quantum fluctuations are crucial in the description of quantum droplets. We emphasize, that the total energy $E_{\mathrm{tot}}/N = -40\,\mathrm{nK}$ is negative, which points towards a self-bound state [53, 55], since it does not rely on any trapping potential. We observed

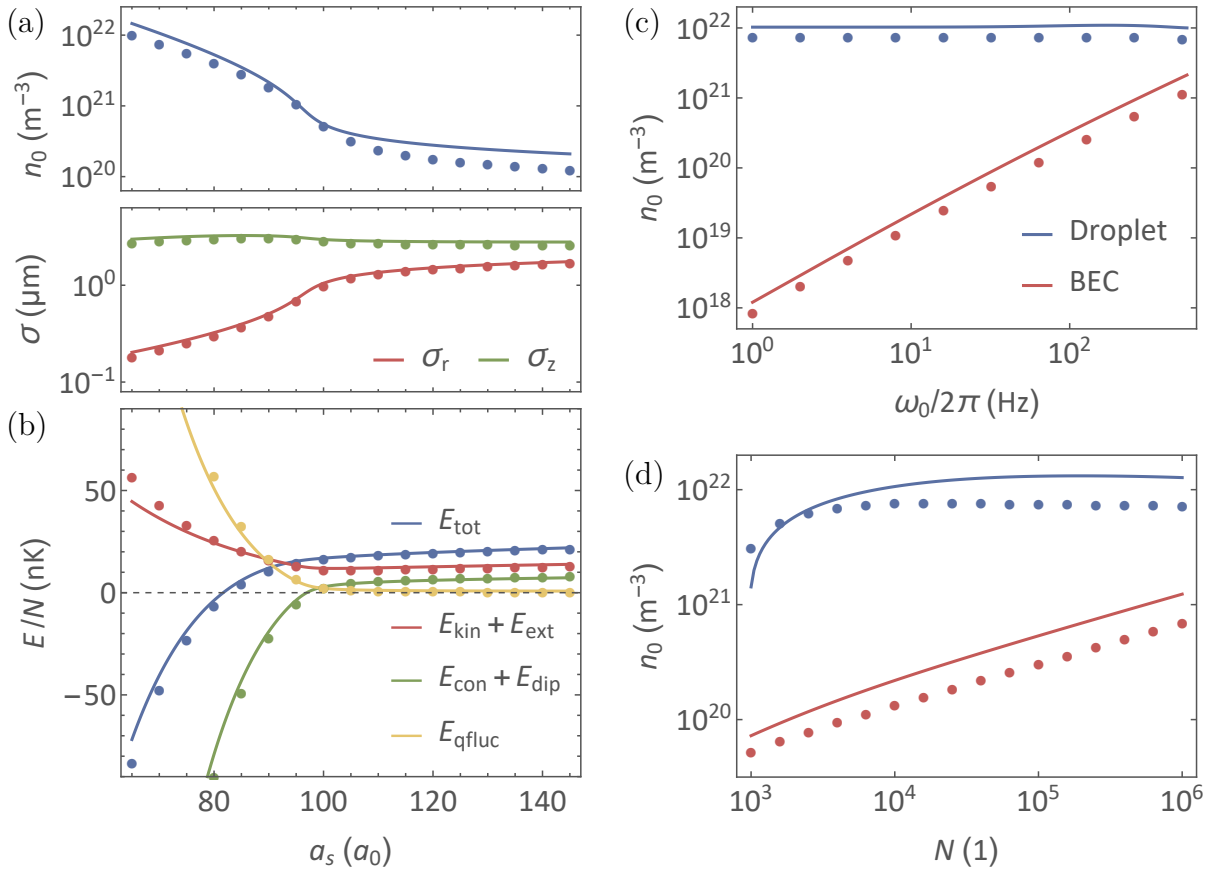

Figure 2.10.: **Properties of BEC and droplet in a spherical trap.** We show peak density n_0 and cloud sizes $\sigma_{r,z}$ (a) as well as various energy contributions (b) over the scattering length a_s. For the latter we compare the total energy E_{tot} (blue) of eq. (2.38) to the single-particle contributions $E_{\text{kin}} + E_{\text{ext}}$ (red) of quantum pressure and external potential, the sum $E_{\text{con}} + E_{\text{dip}}$ (green) of contact and dipolar interaction energy and the beyond-mean field contribution E_{qfluc} (yellow). For large scattering length a_s we find the BEC solution (red) and for small scattering length the quantum droplet solution (blue). For both solutions (assuming $a_s = 140\,a_0$ and $70\,a_0$, respectively) the peak density n_0 is shown for varying mean trap frequency ω_0 (c) and atom number (d) in order to depict the qualitative difference in the two regimes. We compare numerical simulations (points) to the variational ansatz (lines). See [99] for further parameters.

self-bound dipolar quantum droplet experimentally [3] and further discuss these in ch. 6. Studying the dependence of the peak density n_0 on both mean harmonic trap frequency ω_0 and atom number N in fig. (2.10c), we find the known scaling $n_0 \propto (N\omega_0^3)^{2/5}$ derived in the Thomas-Fermi regime [60, ch. 11.2] for the BEC solution ($a_s = 140\,a_0$, red). The droplet case ($a_s = 70\,a_0$, blue) is remarkably different, since the peak density is almost independent of the confinement. Therefore it is incompressible within this parameter range. The situation is similar for the dependence on atom number, where we find a

plateau for $N \geq 10^4$ atoms. In ch. 2.5, we will find that the density distribution becomes flat due to increasing surface tension. For smaller atom numbers, the attractive residual two-body interactions E_2 compete with the quantum pressure lowering the density until a critical atom number N_c, where the droplet solution vanishes.

Incompressible liquids are typically self-bound and characterized by a fixed peak density and finite surface tension. The behavior presented here is analogous to a droplet of liquid helium [67, 135, 136], which has orders of magnitude higher density. In analogy to this quantum liquid, we call a dysprosium condensate in the droplet regime a *dilute quantum liquid*. While the former are spherical in free space, dipolar *quantum droplets* have an intrinsic elongation due to the anisotropic dipolar interaction. This of course also changes the excitation spectrum, which we derive in the following section.

2.4.4. Collective excitations

The collective excitations of a quantum gas allow for precise spectroscopic measurements of the underlying interactions. For the pioneering BEC experiments [137–139], measurements of such excitations verified the applicability of mean-field theory for contact-interacting BECs. In the case of the scissors mode, it was a strong hint towards superfluidity of the interacting condensate [140]. In the following, we present the lowest-lying collective oscillations in the BEC to droplet crossover regime and point out the derivation of the mode frequencies within the Lagrangian formalism based on [7, 80].

Figure (2.11a) illustrates the motion of the cloud for these modes. The monopole mode M, also called the compression mode, corresponds to a simultaneous in-phase oscillation of the sizes $\sigma_{x,y,z}$ and therefore leads to an oscillation of the peak density of the gas. In contrast, the two quadrupole modes are surface modes preserving the peak density. Q_1 is characterized by an out-of-phase oscillation of radial σ_x, σ_y and axial size σ_z for the dipole axis $\boldsymbol{\mu_m} \parallel \hat{\boldsymbol{z}}$. Q_2 features a radial out-of-phase oscillation between σ_x and σ_y preserving the axial size σ_z along the symmetry axis. For a contact-interacting condensate in a spherical trap with mean trap frequency ω_0, the two are degenerate at a frequency of $\sqrt{2}\omega_0$ derived in the Thomas-Fermi regime [60, ch. 12.2]. In this situation, the monopole mode frequency is $\sqrt{5}\omega_0$. For a dBEC the quadrupole degeneracy is lifted due to magnetostriction, and thus the frequencies depend on the aspect ratio of the condensate. Lastly, the scissors mode S_xz corresponds to an oscillation of the condensate symmetry axis about the dipole axis, which is described by the angle θ between the two axes in the xz-plane.

In order to calculate the corresponding frequencies, we introduce additional time-dependent

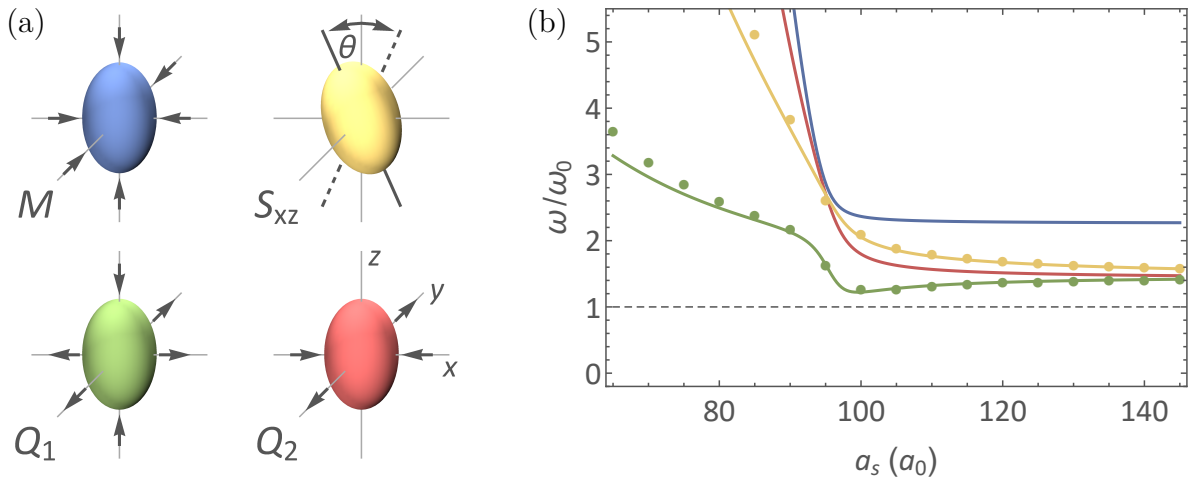

Figure 2.11.: **Excitation spectrum in the BEC to droplet crossover.** (a) Lowest-lying excitations of a dBEC. The monopole mode M corresponds to a compression simultaneous compression along all axes. The scissors mode S_{xz} is a rotation of the condensate around the dipole orientation $\boldsymbol{\mu_m} \parallel \hat{\boldsymbol{z}}$ in the xz-plane. There are also two quadrupole modes characterized by out-of-phase oscillations with a component along the magnetic field (Q_1) and the mode Q_2 where the quadrupole motion is restricted to the xy-plane. Adapted from [132, fig. 1]. (b) Excitation frequency ω in units of the mean trap frequency ω_0. By variation of the scattering length in a spherical trap ($\lambda = 1$) the crossover from a BEC to a droplet can be analyzed. Around $a_s \approx 95\,a_0$ the crossover to the droplet occurs. Below this value the modes M, S_{xz} and Q_2 bend up sharply, while Q_1 remains the lowest mode [99]. We compare numerical simulations (points) to the variational ansatz (lines).

parameters to the gaussian ansatz in eq. (2.37). This ansatz reads

$$\psi_{\mathrm{g}}(\boldsymbol{r}, t) = \sqrt{\frac{N}{\pi^{3/2}\sigma_x\sigma_y\sigma_z}} \exp\left[\sum_{k=x,y,z}\left(-\frac{k'^2}{2\sigma_k^2} + ik'^2\beta_k(t)\right) + ix'z'\Omega\right] \tag{2.40}$$

with the dynamical parameters β_k along the three dimensions and Ω, which allows for a rotation

$$x' = x\,\cos(\theta) + z\,\sin(\theta) \qquad y' = y \qquad z' = -x\,\sin(\theta) + z\,\cos(\theta) \tag{2.41}$$

of the cloud with respect to the dipole axis $\boldsymbol{\mu_m} \parallel \hat{\boldsymbol{z}}$ in the xz-plane. It is important to note, that these degrees of freedom need to allow for the particular mode under investigation. By introducing additional parameters $\beta_{x,y,z}$ along the three dimensions, we can thus study the monopole and both quadrupole modes [55, 83] presented in fig. (2.11a). The angle θ between the cloud symmetry axis and the dipole axis, then additionally allows for the scissors mode oscillation [7]. In order to derive the equations of motion for the sizes and

this angle, the ansatz eq. (2.40) is inserted in the Lagrangian density

$$\mathcal{L} = \frac{i\hbar}{2}\left(\psi\partial_t\psi^* - \psi^*\partial_t\psi\right) + \frac{\hbar^2}{2m}|\nabla\psi|^2 + V_{\text{ext}}|\psi|^2 + \frac{1}{2}g|\psi|^4 + \frac{1}{2}|\psi|^2\Phi_{\text{dd}} + \frac{2}{5}g_{\text{qf}}|\psi|^5 \quad (2.42)$$

shown in [55]. From this, we calculate the Lagrangian $L = \int\mathcal{L}\,\mathrm{d}\boldsymbol{r}$ and derive the Euler-Lagrange equations for the parameters

$$\beta_k = \frac{m}{2\hbar\sigma_k}\frac{\mathrm{d}\sigma_k}{\mathrm{d}t} \quad \text{and} \quad \Omega = -\frac{m}{\hbar}\frac{\sigma_x^2 - \sigma_z^2}{\sigma_x^2 + \sigma_z^2}\frac{\mathrm{d}\theta}{\mathrm{d}t}\,. \quad (2.43)$$

The equations of motion for the sizes σ_k and angle θ of the cloud then follow by replacing for β_k and Ω. The collective excitation frequencies can be obtained by linearization of the system, which yields eq. (8) and (9) in [55] for mono- and quadrupole modes, respectively, and eq. (1) in [7] for the scissors mode. For the former, this approach also allows to extract the normalized mode geometry γ, i.e. the relative oscillation amplitudes along the three axes, which we are going to analyze in the following.

In fig. (2.11b) we show the calculated collective excitation frequencies over varying scattering length a_{s} in the BEC to droplet crossover. For a comparison with the static properties in this range, see fig. (2.10). Around the transition at $a_{\text{s}} \approx 95\,a_0$, the frequencies of monopole mode M, radial quadrupole mode Q_2, and scissors mode S_{xz} bend up sharply owing to the larger density. The axial quadrupole Q_1 shows a weaker scaling of the mode frequency in the droplet regime, and thus remains the lowest-lying mode. Entering the regime where the gas becomes increasingly incompressible we would naively expect a stronger scaling of M compared to both quadrupole modes $Q_{1,2}$, that should behave similarly. The reason is the oscillation of the peak density for the monopole mode, which is related to the compressibility of the gas.

In order to clarify this inconsistency, we analyze the mode geometry in the BEC and droplet regime corresponding to a scattering length of $a_{\text{s}} = 140$ and $70\,a_0$, respectively. As mentioned, the radial quadrupole mode Q_2 corresponds to an equal out-of-phase contribution along the x and y direction, while there is no oscillation along z, resulting in $\gamma_{Q_2}(a_{\text{s}}) = \frac{1}{\sqrt{2}}\{1, -1, 0\}$. The latter is constant throughout the crossover, since the interactions and thus the cloud are radially symmetric in the spherical trap. In contrast, the monopole mode M is modified by the change of aspect ratio. Due to magnetostriction in the BEC regime the mode geometry $\gamma_M = \{0.47, 0.47, 0.74\}$ is slightly anisotropic. In the droplet regime, it becomes an approximate radial monopole mode with $\gamma_M = \{0.71, 0.71, 0.04\}$, since the radial and axial contributions decouple due to the large aspect ratio of the cloud. This also affects the axial quadrupole mode Q_1, where

the mode geometry $\gamma_{Q_1} = \{-0.53, -0.53, 0.67\}$ in the BEC regime changes to an approximate axial monopole mode with $\gamma_{Q_1} = \{-0.03, -0.03, 0.99\}$ in the droplet regime. Finally, in the droplet regime the sizeable aspect ratio leads to a larger excitation energy of modes M and Q_2 with dominant radial character compared to the mode Q_1 with dominant axial character [55]. This way, we can understand the qualitative difference of the two quadrupole modes. The presented behavior hints towards a much higher radial compressibility of the droplet compared to the axial one owing to the large aspect ratio of the droplet.

In experiments, a small shift of the axial quadrupole mode frequency due to the dipolar interaction was observed with chromium dBECs [36]. In the realm of quantum droplets, the applicability of the eGPE was confirmed by measurements of the lowest-lying excitation Q_1 for a quantum droplet of erbium atoms [56]. In ch. 5, we present our measurements of the collective excitations of a ^{164}Dy droplet [7], which we use to extract the scattering length a_s.

2.5. Numerical simulations

While we gain a lot of insight from the approximate solution of the eGPE, there are still open questions that cannot be answered by the variational ansatz presented in the previous section. By design this approach is limited to the density distribution given by the trial wavefunction. Thus it cannot describe the predictions of biconcave ground states [118], as well as transient structures in the collapse dynamics [35, 120, 121]. In particular, the variational ansatz cannot capture the dynamics of the modulational instability and the subsequent fragmentation into multiple droplets we encountered in the first droplet experiment [1]. Additionally, classical ferrofluids show a rich variety of phases with selforganised patterns [141], that might prove to exist for its quantum counterpart as well.

In order to address such effects, a numerical solver for the eGPE on a three-dimensional grid was conceived and realized during this thesis. The numerical details, implementation, and instructions on the usage of the program are presented in appendix A. With this tool, we can exploit every aspect of the eGPE. In principle it offers — up to numerical errors — exact solutions of eq. (2.21) for the ground state and the dynamics, with the only drawback of large simulation times. Since experiments are limited to a certain parameter space, such a tool is especially useful to test predictions within these.

We want to emphasize, that this tool has been crucial to shape our understanding of dipolar quantum gases. As such, it contributed to various publications [3–6, 8] as well as

PhD theses [142, 143]. In this thesis, 21 figures are based on numerical simulations. In the following, we demonstrate effects that become accessible with this tool.

2.5.1. Ground states

The ground state for a given configuration of external potential and interactions can conveniently be computed by imaginary time evolution [144, app. A]. This way, we obtain the ground state wavefunction and can calculate properties like the peak density, sizes as well as the energy contributions of eq. (2.22). In fig. (2.10) we compare the numerical simulations (points) to the variational method with a gaussian ansatz (solid) throughout the crossover region between BEC and droplet. While we find overall good agreement, there are obvious deviations in the peak density due to the deviation of the exact density distribution from the gaussian. In fig. (2.12a) we therefore show the calculated density profiles (solid) and, as mentioned in the previous section, recover the limits of a gaussian ($N = 1 \times 10^3$ atoms, dotted) and a Thomas-Fermi parabola (64×10^3 atoms, dashed) for small and large interactions, respectively[14]. The peak density increases with the atom number as expected for a gaseous BEC.
The case of the self-bound quantum droplet in fig. (2.12b) is more interesting. Here, we find a gaussian density distribution for $N = 1 \times 10^3$ atoms. For larger atom numbers the peak density increases and then saturates for $N \gtrsim 10^4$ atoms at $n_0 \approx 8 \times 10^{21}\,\mathrm{m}^{-3}$. In this saturated regime, the droplet develops a constant bulk density with a finite surface thickness. This behavior is typical for the liquid state emerging from the interplay of repulsive and attractive interactions. Consequently, we find it in various systems for a wide density range. Examples are the related ultracold Bose-Bose mixtures stabilized by quantum fluctuations [48], droplets of liquid helium [67, 136], simple *Lennard-Jones* liquids [145, 146], and atomic nucleii described by the macroscopic *liquid drop model* [147, ch. 1].
In addition, the long-range character of the dipolar interaction gives rise to another class of phenomena, that are known from classical ferrofluids [141]. In ch. 4, we discuss the influence of confinement, which leads to ground states featuring multiple droplets.

2.5.2. Dynamics

With this numerical method, we can model any time-dependence of external parameters, e.g. the magnetic field direction or the external potential, and study the related dynamics

[14] In relation to the quantum pressure. For the former this contribution is dominant compared to the interactions, while it can be neglected in the Thomas-Fermi regime.

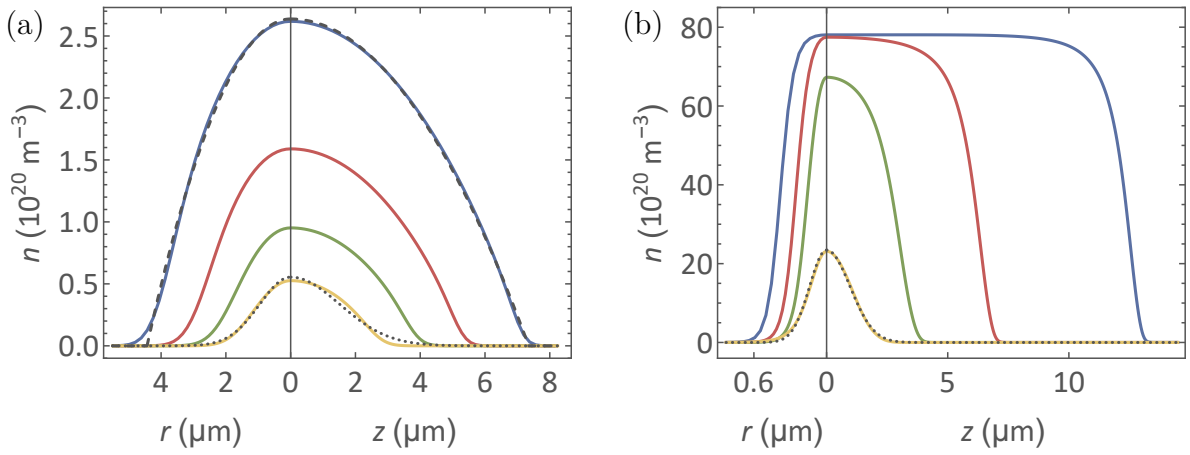

Figure 2.12.: **Density distribution of a dBEC and a self-bound droplet** for $N = \{1, 4, 16, 64\} \times 10^3$ (yellow to blue) atoms. For a gaseous dipolar BEC (a) the peak density n_0 increases with atom number N. Due to the dipolar interaction, there is magnetostriction in the spherical trap. For large interactions and atom number, the density profile is well described by a Thomas-Fermi parabola (dashed). In the other limit for small interactions, it can be approximated by a gaussian (dotted) [99]. In contrast, for a self-bound quantum droplet (b) the peak density saturates at $n_0 \approx 8 \times 10^{21}\,\mathrm{m}^{-3}$ for $N \gtrsim 10^4$ atoms and it grows axially due to increasing surface tension, exemplifying the liquid-like behavior. Note the rescaled radial axis. Close to the critical atom number the density profile is well described by a gaussian (dotted). The scattering length is $a_s = 70\,a_0$, and there is no external potential.

by real time evolution of the eGPE. An example is the moving laser beam we use to measure the superfluid behavior of the dBEC in ch. 7. Collective excitations can be extracted by monitoring the condensate after a small quench of the trapping potential, as pointed out later. For now, we focus on the dynamics of the dBEC after a quench of the scattering length. With chromium condensates, this leads to a d-wave collapse [35], where numerical studies have been key to understand the dynamics. In this spirit, we examine the *modulational instability* causing the fragmentation of a single dBEC into multiple droplets [1, 2, 4]. We emphasize, that the ground state is a single droplet within the experimental parameter range, and thus the fragmentation process is purely dynamical.

Modulational instability

The fragmentation into multiple droplets is triggered by a quench of the scattering length to lower values, which in turns leads to a larger equilibrium density and dipolar strength $\varepsilon_{\mathrm{dd}}$. In steady state, both effects lead to the rotonization of the dBEC, which is the underlying mechanism of the instability, see ch. 2.3.4. The softening of modes with finite momenta k leads to a local collapse of the dBEC. In our system with finite size σ_z along

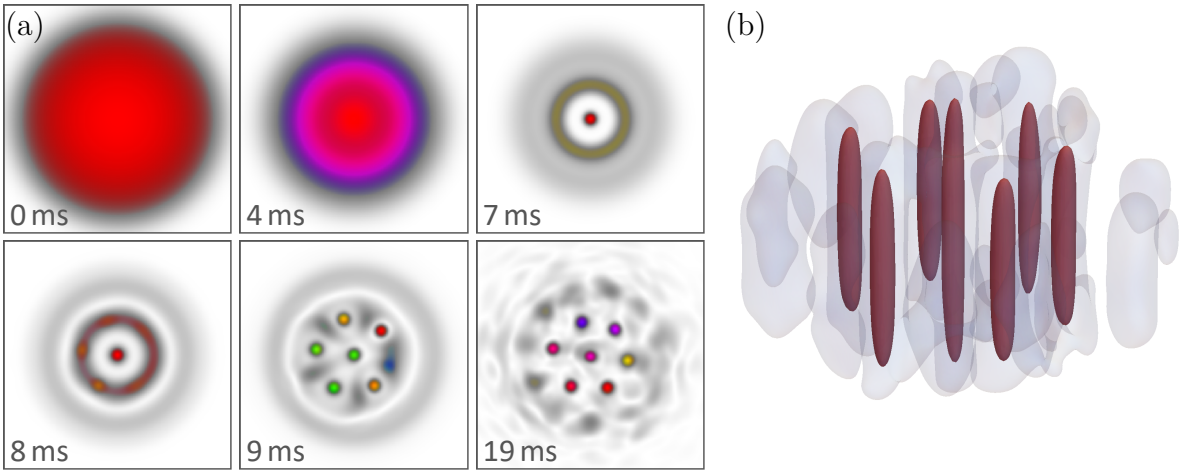

Figure 2.13.: **Modulational instability and droplet creation.** (a) Evolution of condensate density and phase after a quench of the scattering length from $a_s = 140$ to $70\,a_0$ at $t = 0\,\mathrm{ms}$. We use $N \approx 18 \times 10^3$ dysprosium atoms in a trap with mean frequency $\omega_0 = 2\pi \times 70\,\mathrm{Hz}$ and aspect ratio $\lambda = 3$. The field of view is $(12\,\mu\mathrm{m})^2$ and the color code with white-gray-hue is proportional to the logarithm of the density with a hue determined by the phase of the condensate. (b) Isosurfaces of the density distribution in the last panel with $0.01\,n_0$ (gray) and $0.2\,n_0$ (red).

the dipole axis, the contributing modes with $k\,\sigma_z \approx 1$ are not well-defined, and lead to the instability we describe in the following.

For the simulation, a dBEC of $N = 15 \times 10^3$ dysprosium atoms with scattering length $a_s = 140\,a_0$ is prepared in its ground state. In order to model thermal fluctuations, we add ≈ 3400 of atoms in randomly Boltzmann-weighted excited states corresponding to $T = 50\,\mathrm{nK}$, see appendix A.1. At $t = 0\,\mathrm{ms}$ we quench the scattering length instantaneously to $a_s = 70\,a_0$ and compute the real time evolution of the eGPE for the subsequent 20 ms. Figure (2.13a) shows the condensate density and phase for various times. At $t = 0\,\mathrm{ms}$ we acquire a stable condensate with uniform phase. The quench to lower scattering length and thus larger equilibrium density leads to a rapid decrease in size and a radial density modulation emerges at $t = 4\,\mathrm{ms}$. It leads to the formation of a single droplet surrounded by a torus at $t = 7\,\mathrm{ms}$, see also [120]. Subsequently, the ring undergoes an angular collapse [121], and splits up into multiple droplets at $t = 9\,\mathrm{ms}$. Unlike the mean-field approach predicting a rapid loss of atoms in these references, the droplets are stable within the eGPE and repulsive with respect to each other. The position of the droplets that emerge along the transient torus is seeded by the initial fluctuations rendering the droplet creation a stochastic effect. While the single droplets show a uniform phase, there is fast dephasing between neighboring droplets within few ms due to a difference in atom number and thus chemical potential. 10 ms later, the droplets arrange within their equilibrium distance, which is illustrated in fig. (2.13b). Since the inter-droplet interaction is repulsive and

isotropic in the plane, they arrange in triangular patterns. With a finite energy barrier for the recombination, these states are metastable, which prevents the system from reaching the ground state of a single droplet, see the previous section.

Such a simulation recreates both the formation time of $\sim 7\,\mathrm{ms}$ and the droplet patterns we observed in the seminal experiment [1]. Introducing three-body losses, the observed droplet lifetime can be reproduced additionally [54]. At this point, we also want to give credit for the early computational contributions, that relied on a non-existent repulsive three-body interaction instead of quantum fluctuations as the stabilization mechanism [49–51]. Being a competing theory at the time, these were able to recreate the experiment nicely and motivated the development of our own numerical simulations.

The modulational instability in an elongated geometry like a waveguide is very similar and leads to a line of multiple droplets, as observed in [2]. In such a configuration, the population of finite-momentum modes prior to the collapse dynamics was experimentally confirmed by time-of-flight measurements of quenched dipolar erbium condensates [122].

Collective excitations

Other dynamic effects like collective excitations can be extracted by monitoring the size of the cloud after a small quench of e.g. the trap [55], as shown in fig. (2.11b) for the lowest-lying quadrupole and the scissors mode. There, the deviation in the droplet regime stems from the fact, that the density profile is not a gaussian, as assumed with the variational method. Such an approach is typically limited to small perturbations of the ground state and thus only excites the lowest energy modes. In order to derive the full spectrum, the time-dependent GPE can be linearized around the ground state solution. Within the Bogoliubov theory, the Bogoliubov–de Gennes equations can be derived, which are then solved numerically in order to obtain the excitation energies. This way, the full spectrum of a cylindrical dBEC [148, 149] and a self-bound droplet [150] have been calculated. As expected, this approach recovers the lowest-lying modes we obtained with the variational ansatz in the last section.

Interestingly, there is a major difference in comparison to droplets of Bose-Bose mixtures [48]. For these, the excitation energies of all modes are larger than the threshold $-\mu$ for particle emission, in a certain atom number range above the critical atom number N_c. In this regime, any residual excitation due to, e.g., finite temperature leads to the evaporation of atoms and thus is expected to finally cool the droplet to zero temperature. In contrast, for dipolar droplets the energy of the lowest modes is well below this threshold and thus a full evaporation should not be possible.

2.5.3. Beyond the eGPE

So far we discussed numerical solutions of the eGPE, that includes the Lee-Huang-Yang correction to the chemical potential within a local-density approximation, see ch. 2.2.2. Although there is good agreement with the experiment, this approach raises the question whether higher-order terms or an approach beyond the local-density approximation need to be included in some scenarios. While a more refined microscopic theory for the description of quantum droplets needs to be developed, we can resort to Quantum Monte Carlo studies, where all of these effects are naturally included.
Within the path-integral ground state Monte Carlo formalism, the stabilization mechanism due to quantum fluctuations has been confirmed qualitatively [151]. Further investigations using various Monte Carlo methods predict ground states of multiple droplets with periodic boundaries [152, 153], harmonic confinement [154], and in a 2D geometry [155] featuring off-diagonal long-range order. All of these approaches suffer from the immense computational complexity of the Monte Carlo approaches and are thus limited to a few hundred atoms, which in turn renders larger dipolar interactions necessary to have sizeable effects. More importantly, they typically do not include a realistic atomic interaction potential, e.g. of van der Waals-type, and only assume a hard wall or a repulsive r^{-12} term to describe the short-range physics.
Yet, with a more realistic scattering potential and densities matching the experiment, quantitative studies could be important benchmarks for the applicability of the eGPE. In a collaboration with the authors from [155], we plan to investigate the discrepancy of the critical atom number for the self-bound droplet.

Chapter 3

Experimental Apparatus

After we introduced the reader to the theory for ultracold dipolar bosons, which gives rise to quantum droplets and a variety of interesting dipolar effects in dBECs, it is time to turn to the experiment. With this machine we cool dysprosium atoms to quantum degeneracy, manipulate their internal or external degrees of freedom and image the resulting density distribution.

The whole apparatus including the laser systems has been thoroughly described in [69]. Additional theses describe our phase-contrast imaging technique [142, 156] and the dipole-trap setup for the creation of a single droplet [143]. Basic laser cooling techniques are covered in the book by C. Foot [157]. In the following, we briefly describe the properties of dysprosium and its advantages for experiments with ultracold atoms, then we explain the recent changes to the apparatus, and finally outline the preparation of a dBEC with our setup.

3.1. Dysprosium

The element dysprosium belongs to the lanthanides series of chemical elements, characterized by an open $4f$-shell. The large natural abundance of two bosonic isotopes, ^{162}Dy and ^{164}Dy, and two fermionic ones, ^{161}Dy and ^{163}Dy, makes it a versatile choice for the field of ultracold atoms [158]. As mentioned earlier, the electronic configuration is $[\mathrm{Xe}]\, 4f^{10}\, 6s^2$ with a ground state $^5\mathrm{I}_8$. The bosons have a vanishing nuclear spin $I = 0$, while the fermions possess a nuclear spin $I = {}^5/_2$, which results in the hyperfine levels $F = {}^{11}/_2, \ldots, {}^{21}/_2$ of the ground state. The sizeable total angular momentum $J = 8$ leads to a magnetic moment $\mu_\mathrm{m} \approx 10\mu_\mathrm{B}$ and thus the largest magnetic dipole-dipole interaction

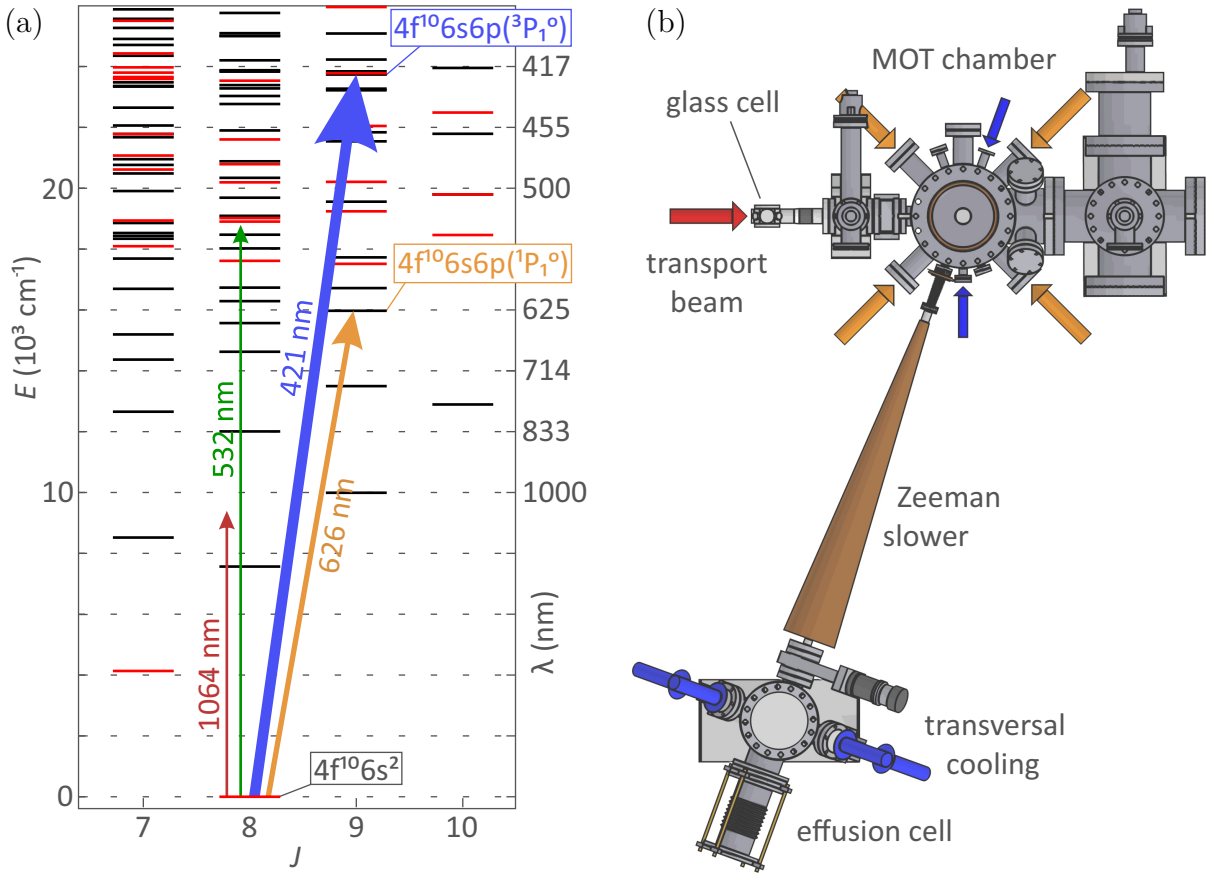

Figure 3.1.: **Laser cooling of dysprosium.** (a) Energy levels in dysprosium. The ground state $4f^{10}6s^2$ is even. We use the $J = 8 \rightarrow 9$ transitions near 421 nm and 626 nm for laser cooling in a Zeeman slower and a magneto-optical trap (MOT). Also shown are the dipole trap wavelengths 532 nm and 1064 nm, that are far detuned from the dominant blue transition. (b) Schematic of the full setup to create cold samples of dysprosium. After a Zeeman slower with transversal cooling, atoms are trapped in the MOT and then transported to the glass cell. In there, quantum degeneracy is reached by further laser and evaporative cooling.

amongst stable isotopes in the periodic table[1].

The atomic energy spectrum is depicted in fig. (3.1a), showing a strong optical transition at $\lambda_{\text{blue}} = 421\,\text{nm}$ with a linewidth of $\Gamma_{\text{blue}} = 2\pi \times 32.2(8)\,\text{MHz}$ [159] and a weaker optical cycling transition at $\lambda_{\text{orange}} = 626\,\text{nm}$ with a linewidth of $\Gamma_{\text{orange}} = 2\pi \times 136(4)\,\text{kHz}$ [160]. In the presented apparatus, this combination allows for fast pre-cooling to intermediate temperatures with the former and subsequent cooling to temperatures of $10^{-5}\,\text{K}$ with the latter [161]. Additionally, the strong line in the blue is beneficial for imaging of the atoms,

[1] We compare the coefficient $m\mu_{\text{m}}^2$ of the dipolar interaction in eq. (2.7). Tb has a similar magnetic moment at slightly smaller mass compared to Dy. The actinides Bk, Cf and Es would have a $1.3-1.6$ times stronger dipolar interaction, with the caveat of being radioactive [69]

since the resolution of an optical system is proportional to the wavelength of the light [109, ch. 4]. Both Nd:YAG wavelengths of 532 and 1064 nm, where high-power lasers are available, are red-detuned with respect to the dominant transition at 421 nm and thus can be used as optical dipole traps (ODTs) [125]. Finally, both BECs [40] and Fermi gases [41] had been realized before our experiment was conceived, indicating favorable scattering properties at low temperatures.
For these reasons, dysprosium is an optimal choice for the study of dipolar effects with ultracold atoms.

3.2. Setup

In order to decouple the sample from the environment, experiments with ultracold atoms are carried out in ultra-high vacuum chambers and are manipulated with external magnetic or electric fields and laser beams. The full setup shown in fig. (3.1b) allows for the cooling to quantum degeneracy. It includes a high-temperature effusion cell, a Zeeman slower directed at the MOT chamber, and a glass cell where we reach quantum degeneracy and conduct the experiments. In the following we only list the recent changes to the machine and the optics. For a thorough description of the apparatus see [69, 142, 143, 156].

Crossed ODT

The two optical dipole traps, which we use in a crossed configuration for forced evaporative cooling have been rebuilt based on large-mode-area fibers[2]. Aiming for fiber input powers of $> 20\,\mathrm{W}$, there is substantial heating of the fiber due to imperfect coupling with $\sim 70\%$ efficiency of the incident beam. For this reason we attached a copper heat sink to the part of the fiber where the power is dissipated and actively stabilize its temperature with a peltier element. Compared to the old fibers, which were prone to strong polarization drifts and were burned on a regular basis, we achieve stable operation with a persistent coupling efficiency and did not observe polarization drifts over the course of one year.
For ODT1, which is superimposed with the transport beam, we use a round beam with a focused waist of $37\,\mu\mathrm{m}$ to maximize mode-matching with the former. The maximum power is $P = 13.6\,\mathrm{W}$ measured in front of the glass cell. In contrast, ODT2 is elliptical with waists of 38 and $120\,\mu\mathrm{m}$ along $\hat{\boldsymbol{z}}$ and ODT1, respectively, and a measured maximum

[2] ODT parts: Laser `Coherent Mephisto Mopa 55W`, fiber `NKT aeroGUIDE-Power`, collimators `Schäfter Kirchhoff 60FC-SMA-T-23-A18-03`. Prior to this, we used the fibers `OZ Optics PMJ-A3HPC,A3HPC-1064-10/125-5AS-2-1-LMA` with collimators from the same manufacturer

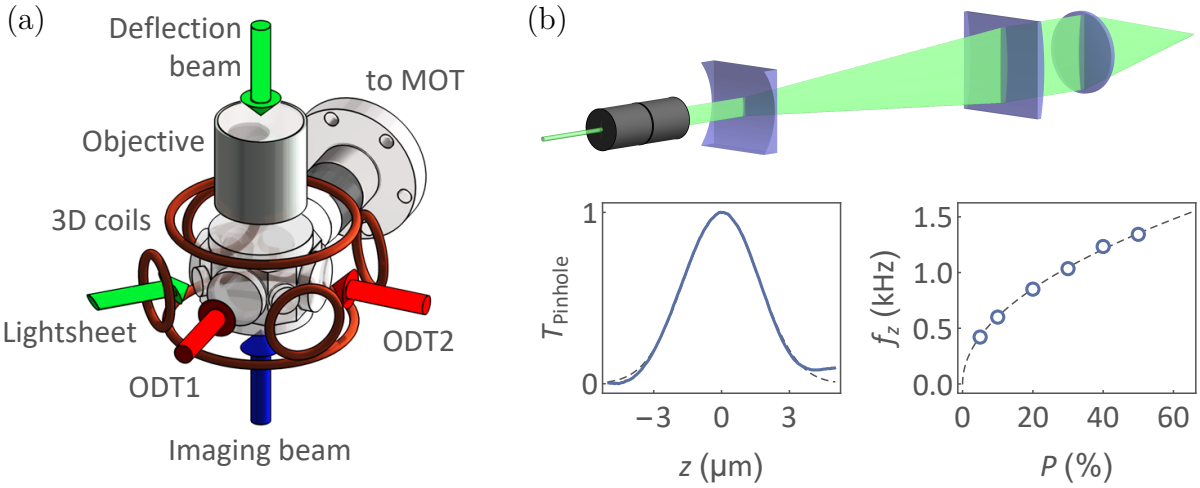

Figure 3.2.: **Schematic of glass cell and lightsheet.** (a) For the manipulation and imaging of the atoms, we employ two dipole traps ODT1 & 2 at 1064 nm for forced evaporative cooling to quantum degeneracy. An additional lightsheet along the diagonal gives strong confinement along $\hat{\boldsymbol{z}}$ and a deflection beam can be used to write time-averaged potentials. The objective with an NA of 0.34 is used for in situ imaging. Not shown are the Doppler cooling at λ_{orange} and low-resolution imaging with λ_{blue} along ODT2. (b) Our lightsheet setup creates a highly-elliptical beam with two mounted prism pairs and a cylindrical telescope, which is then focused on the atoms by a plano-convex lens. With the measured waist of 3.3(1) μm we reach trap frequencies up to 2 kHz.

power of $P = 10.5\,\text{W}$. With the combination of the two, we achieve a trap aspect ratio $\lambda \approx 3$. As shown in the previous chapter, this is necessary to prevent a strongly-dipolar BEC, i.e. $\varepsilon_{\text{dd}} > 1$, from forming droplets with an order of magnitude smaller lifetime.

Lightsheet

We employ a highly elliptical beam, a so-called *lightsheet*, to have strong confinement along the $\hat{\boldsymbol{z}}$ direction in the experiment. The setup[3] is shown in fig. (3.2b), where the beam from a large-mode-area fiber with a waist of 450 μm is expanded by a factor 16 along the z direction and shrinked by a factor 4 perpendicular to it. Focussing this beam with a single $f = 100\,\text{mm}$ plano-convex lens yields a waist of $w_z = 3.3(1)$ μm measured by recording the transmission through a 1 μm pinhole that is moved through the beam by a piezo mirror. Mounted prism pairs have the advantage to magnify the beam by a factor

[3] Lightsheet parts: Laser `Coherent Verdi V10`, fiber `NKT aeroGUIDE-Power`, collimators `Schäfter+Kirchhoff 60FC-SMA-T-23-A15-01`, two mounted anamorphic prism pairs `Thorlabs PS883-A`, a 4:1 telescope of `Thorlabs LJ1996L1-A` & LK1431L1-A, and a single $f = 100\,\text{mm}$ lens `Thorlabs LA1050-A` to focus on the atoms.

4 over a short distance of 31 mm, which should improve the mechanical stability of the system, and the disadvantage of 85% transmission only. Indeed, compared to a first setup relying on a design with ordinary lenses, we see a valueable improvement of the pointing stability. In the experiment, we reach trap frequencies of $f_z = 2\,\mathrm{kHz}$, fitting the expected $f_z \propto \sqrt{P}$ scaling with respect to beam power P, where 100% correspond to a power of $\sim 250\,\mathrm{mW}$. At the highest powers there is substantial heating lowering the lifetime of a dBEC by an order of magnitude. With the lightsheet and the two ODTs above, we can realize almost round traps ($f_x \approx f_y$) with a trap aspect ratio of $\lambda = f_z/\sqrt{f_x f_y}$ up to 33 along the magnetic field axis. For such strong confinement, we realize effective tuneability of the dipolar interaction by tilting the magnetic field in ch. 4. For future experiments, we recommend to control the beam pointing with a piezo-driven mirror, as manual alignment with such a small waist can be cumbersome.

Electro-optical deflector

The microscope objective[4] we use for imaging is further designed to focus a tight trap at $\lambda = 532\,\mathrm{nm}$ on the atoms. In conjunction with an electro-optical deflector (EOD) system[5] the *deflection* beam can be used to write time-averaged potentials, as realized in [156], where the setup is thoroughly described. For the experiment in ch. 7.1, we use it to drag an attractive potential at constant speed through a dBEC in order to measure its superfluid properties. For the current setup the beam waist is $\approx 1.5\,\mu\mathrm{m}$ yielding a deflection radius of almost $4\,\mu\mathrm{m}$. In order to obtain reproducible results, we trigger the start of the beam movement with the experiment control, fixing the phase of the stirring sequence in between runs, see [162] for the implementation. We additionally realized a repulsive deflection beam with a $\lambda = 405\,\mathrm{nm}$ laser[6], that is superimposed with the attractive beam on a dichroic mirror, and shall be used to create vortices in a dBEC, as outlined in ch. 7.2.

Phase-Contrast Imaging

Our imaging technique based on [163] is thoroughly described in [156]. With a magnetic field $\boldsymbol{B} \parallel \hat{\boldsymbol{z}}$ pointing along the beam, linearly polarized light decomposes into equal parts of σ_- and σ_+ light. With an atom in the stretched state $m_J = -8$ of the $J = 8$ ground

[4] Microscope objective: Custom design by `Special Optics` with an effective focal length of $f = 25\,\mathrm{mm}$ and a numerical aperture of 0.34. We achieve a resolution of $0.99(3)\,\mu\mathrm{m}$ at $\lambda_{\mathrm{blue}} = 421\,\mathrm{nm}$ [156].

[5] Deflector parts: Both the two deflectors `Conoptics M311A` with 1.5 mrad deflection, and the pockels cell `Conoptics M350-50C-01` with 350:1 extinction are equipped with 200 kHz drivers and controlled by a real-time processing system `ADwin Gold II`.

[6] Based on a `Thorlabs L405P150` laser diode with 150 mW power in a custom housing.

state the former couples to the $m_{J'} = -9$ state. For the σ_+ transition to the $m_{J'} = -7$ state, the coupling and thus the resulting phase shift of the atoms is suppressed by a factor of ~ 150 due to the difference in Clebsch-Gordan coefficients. This setup can be seen as an interferometer, relying on the differential phase shift of these two polarizations. The detuning Δ of the imaging laser from the resonance at λ_{blue} is proportional to the inverse phase shift and chosen such, that we operate the interferometer on the slope of the first interference fringe. In the experiment, it is in the range $\Delta/\Gamma_{421} = 5$ to 50 depending on the column density of the object along the imaging beam. This way, our imaging technique relies on a magnetic field pointing along the imaging beam with a linear polarization [156]. In order to image atoms with tilted magnetic fields[7] $B < 1.4\,\text{G}$, we ramp up the fast coils along $\hat{\boldsymbol{z}}$ to $\sim 10\,\text{G}$ within $100\,\mu\text{s}$ prior to imaging. This way, the density distribution is unaffected during the imaging phase, while still having a sufficient projection of the magnetic field along the imaging beam.

Magnetic Field

For the experiments in chapters 5 and 4 we tilted the magnetic field and modulated the field angle with large "cage" coils around the glass cell. Designed to compensate the surrounding magnetic field, these only reach magnetic fields below 2 G and are slow limiting a 90°-tilt of the magnetic field in the xy-plane to $\sim 3\,\text{ms}$. The amplitude of the magnetic field is important, since there are convenient Feshbach resonances located around 5 and 7 G for ^{162}Dy and ^{164}Dy, respectively. The measurements in ch. 4 were limited by the narrow Feshbach resonance in use.
To circumvent such problems, we added two sets of coils in the xy-plane around the glass cell [164], see fig. (3.2a). Paired with a bipolar current source[8], we reach a magnetic field of 10 G from DC up to a cut-off frequency of 500 Hz. With these, we have control of the magnetic field on the sub-mG level. Calibration of these coils with radiofrequency spectroscopy shows a deviation of less than 5 mG from the expected linear behavior over the $\pm 10\,\text{G}$ range, which we attribute to magnetic field noise and drifts of the surrounding electronics and magnetic fields.

3.3. Cooling to quantum degeneracy

The typical preparation cycle of an ultracold sample starts with a gaseous beam of dysprosium atoms, that is emitted from an effusion cell heated to $T = 1250\,°\text{C}$. This beam

[7] For the experiments presented here, we exploit a narrow Feshbach resonance located at 1.326(3) mG.
[8] Driver: `Highfinesse BCS 4A/5V` with $< 2.5 \times 10^{-5} I_{\text{max}}$ current stability and reproducibility

is then decelerated in a Zeeman slower with λ_{blue} to a final velocity of $\approx 14\,\text{m/s}$. Then, atoms are slow enough to be captured in a narrow-line magneto-optical trap (MOT) operated at λ_{orange} with a Doppler temperature $T_{\text{D}} = 3.3\,\mu\text{K}$ [161]. In order to increase the atom number by a factor 3-4 we additionally apply Doppler cooling after the effusion cell reducing the transversal velocity. This increases the flux of atoms, that are emitted into the solid angle of the MOT. This way, we typically capture $N = 10^8$ atoms of either bosonic isotope at a detuning of $\Delta = -35\,\Gamma_{\text{orange}}$ and a final temperature of $T = 12\,\mu\text{K}$ after compression of the MOT. Around 2×10^7 of these are loaded into an ODT operated at $\lambda = 1070\,\text{nm}$, resulting in temperatures of $T = 180\,\mu\text{K}$ due to recompression. With the focussing lens mounted on an air-bearing stage, we transport the atoms in this beam to the glass cell.

A schematic of the setup around the glass cell is depicted in fig. (3.2a). From the transport beam we load the atoms in a crossed optical dipole trap of the two focused beams ODT1 and ODT2. The former is mode-matched with the transport beam to increase the loading efficiency, while the latter is elliptical. We subsequently apply Doppler cooling with λ_{orange} reaching $18\,\mu\text{K}$ with 2×10^6 atoms left. We then lower the power in both beams exponentially for forced evaporative cooling of the thermal atoms. Finally, we obtain almost pure dBECs with $N_{^{164}\text{Dy}} = 1 \times 10^4$ or $N_{^{162}\text{Dy}} = 3 \times 10^4$, respectively. Such a dBEC is the starting point for the experiments conducted in this thesis.

In the experiments with the lightsheet, we ramp it up to $\sim 200\,\text{Hz}$ during the evaporative cooling to ensure smooth loading, since it is much smaller than the crossed ODT.

Chapter 4

Striped states with tilted dipoles

Our initial observation of multiple stable quantum droplets [1] immediately raised the fundamental question of supersolidity in this system. While the internal gauge symmetry of a BEC is broken due to a common superfluid phase, the density modulation of these states would additionally break the translational symmetry. The multi-droplet system would thus be a density-modulated superfluid, which was coined a *supersolid*. In contrast to recent claims of supersolidity, where the period of the density modulation is imprinted by an external light field [165, 166] and superfluidity itself has not been shown, in our system the density modulation is due to the intrinsic interaction of the atoms. This has an important consequence, because it allows for finite-wavelength phonons with a defined excitation spectrum, which is not the case for the mentioned systems. Other sates, where anisotropy plays a crucial role, are stripe phases known from superconducting materials [167], which have also been predicted for dipolar system in two dimensions [168].

In this chapter, we review our advances towards the realization of such a supersolid state, which resulted in the publication [5]. First, we show the existence of "striped states" as the ground state of a system of dipoles in an anisotropic trapping potential. We demonstrate that these collectively ordered states break the symmetry along an axis perpendicular to the confinement extending prior theoretical work predicting only single-droplet ground states [54]. In the experiment, we study such an ensemble of dipoles in a constrained geometry. We demonstrate the effective tuning of the mean-field dipolar interaction by tilting the magnetic field in this geometry and additionally gain control over the number of created droplets with the underlying trapping potential. With this tool we observe such striped states with higher droplet numbers than theory predicts. We finally conduct expansion measurements to investigate the coherence properties and outline a way to establish phase coherence of the whole system.

4.1. Ground state in an anisotropic trap

Dipolar quantum droplets share many properties of other liquids, as shown in the previous chapter. Yet, there is a peculiarity owing to the binding mechanism mediated by the attractive dipolar interaction. If a droplet of a usual liquid is compressed along one direction, it deforms conserving the volume and thus the density. For a dipolar droplet that is compressed along the polarization axis, a deformation of the anisotropic density distribution lowers the mean-field dipolar interaction and thus weakens the binding mechanism, which leads to strong frustration. For this reason, states with multiple droplets might have lower energy than the single-droplet states in confined geometries.
In order to verify this idea, we perform semi-analytical calculations in a first step. For this purpose we extend the ansatz presented in ch. 2.4 and introduce the wavefunction

$$\psi_{\mathrm{g}}(x,y,z) = \sqrt{\frac{N_{\mathrm{d}}}{\pi^{3/2}\bar{\sigma}^3}}\exp\left(-\frac{x^2}{2\sigma_x^2}-\frac{y^2}{2\sigma_y^2}-\frac{z^2}{2\sigma_z^2}\right) \tag{4.1}$$

of a single anisotropic droplet with N_{d} atoms and mean size $\bar{\sigma} = (\sigma_x\sigma_y\sigma_z)^{1/3}$. In order to derive the total energy E of a state with two equal droplets separated by a distance d, we insert the wavefunction at the positions $x = \pm d/2$ in the energy functional of eq. (2.22). The total energy

$$\begin{aligned} E(\sigma_x,\sigma_y,\sigma_z,d) &= E\Big[|\psi_{\mathrm{g}}(x-d/2,y,z)|^2 + |\psi_{\mathrm{g}}(x+d/2,y,z)|^2\Big] \\ &= \frac{1}{4}N\frac{\hbar^2}{m}\left[\sigma_x^{-2}+\sigma_y^{-2}+\sigma_z^{-2}\right] + \frac{1}{4}Nm\left[\omega_x^2\left(\sigma_x^2+\frac{1}{2}d^2\right)+\omega_y^2\sigma_y^2+\omega_z^2\sigma_z^2\right] \\ &\quad + \frac{1}{4(2\pi)^{3/2}}\frac{gN^2}{\bar{\sigma}^3}\left[1+\exp\Big(-\frac{1}{2}u^2\Big)-\varepsilon_{\mathrm{dd}}\Big(f(\kappa_x,\kappa_y)+\mathcal{I}_{\mathrm{dip}}(\kappa_x,\kappa_y,u)\Big)\right] \\ &\quad + \frac{2^{5/2}}{5^{5/2}\pi^{9/4}}\frac{g_{\mathrm{qf}}N^{5/2}}{\bar{\sigma}^{9/2}}\mathcal{I}_{\mathrm{qf}}(u) \end{aligned} \tag{4.2}$$

for an atom number $N = 2N_{\mathrm{d}}$ is thus determined by the size of the single droplets $\sigma_{x,y,z}$ and the distance d, which define the aspect ratios $\kappa_k = \sigma_k/\sigma_z$ and the rescaled distance $u = d/\sigma_x$, respectively. While the first two terms covering the quantum pressure and the harmonic potential are linear with respect to the number of droplets, the other terms depend on the overlap of the two wavefunctions. For $d = 0$ we recover the solutions of a single droplet [53, 55]. In this case, the integral

$$\mathcal{I}_{\mathrm{dip}}(\kappa_x,\kappa_y,u) = \exp\Big(-\frac{1}{2}u^2\Big) - 3\frac{\kappa_x\kappa_y}{(1-\kappa_x^2)^{3/2}}\int_0^{\sqrt{1-\kappa_x^2}}\mathrm{d}\xi\,\frac{\xi^2\exp\Big(-\frac{u^2}{2}\frac{\kappa_x^2\xi^2}{(1-\kappa_x^2)(1-\xi^2)}\Big)}{\sqrt{1-\xi^2}\sqrt{1-\xi^2\frac{1-\kappa_y^2}{1-\kappa_x^2}}} \tag{4.3}$$

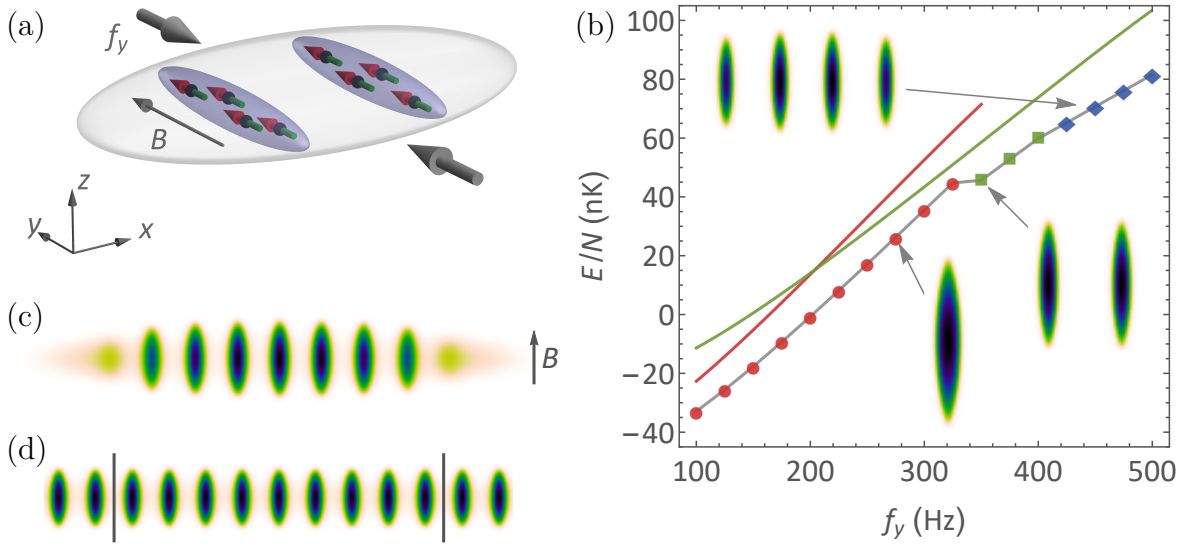

Figure 4.1.: **Striped ground states.** (a) The schematic shows a double droplet configuration in the proposed harmonic trap. (b) Total energy per atom E_{tot}/N for single (solid red) and double (solid green) droplet solutions obtained from a variational ansatz. For $f_y \gtrsim 200\,\mathrm{Hz}$ the state with two droplets has lower energy than a state with a single droplet. Numerical simulations of the extended Gross-Pitaevskii equation, see eq. (2.21), predict a higher number of droplets for increasing f_y in the ground state. Insets show the integrated column density along $\hat{\boldsymbol{z}}$ for ground states with one (red dots), two (green squares) and four (blue diamonds) droplets. (c) The ground state for $f_y = 800\,\mathrm{Hz}$ consists of several droplets. The finite density between the droplets indicates an overlap of the single droplet wavefunctions. (d) For a similar system with periodic boundary conditions along $\hat{\boldsymbol{x}}$ ($f_x = 0$) the ground state exhibits the same density modulation, thus breaking the continuous translational symmetry. Vertical lines represent the edge of the box. See text for further parameters.

for the dipolar interaction reduces to the well-known geometry-dependent function

$$f(\kappa_x, \kappa_y) = \mathcal{I}_{\mathrm{dip}}(\kappa_x, \kappa_y, 0) = 1 - \frac{3\kappa_x\kappa_y}{(1-\kappa_x^2)^{3/2}} \int_0^{\sqrt{1-\kappa_x^2}} \mathrm{d}\chi \frac{\chi^2}{\sqrt{1-\chi^2}\sqrt{1-\chi\frac{1-\kappa_y^2}{1-\kappa_x^2}}} \tag{4.4}$$

for zero distance [169, 170]. Additionally, we define the integral

$$\mathcal{I}_{\mathrm{qf}}(u) = \frac{2}{\sqrt{\pi}} \exp\left(-\frac{5}{8}u^2\right) \int_0^\infty \mathrm{d}v\, e^{-v^2} \cosh\left(\sqrt{\frac{2}{5}}uv\right)^{5/2} \tag{4.5}$$

with $\mathcal{I}_{\mathrm{qf}}(0) = 1$ for the quantum fluctuations term.

With this ansatz we can compare the energy of the single droplet and double droplet

states. For this initial consideration, we choose $N = 10^4$ atoms of ^{164}Dy with dipolar length a_{dd}, scattering length $a_{\mathrm{s}} = 70\,a_0$ in accordance with the measurements in the next chapter, and a harmonic potential with frequencies $f_x = 70\,\mathrm{Hz}$, $f_y = 10 - 500\,\mathrm{Hz}$ and $f_z = 1\,\mathrm{kHz}$. For this parameter range, we indeed find local minima of the energy in eq. (4.2) at both $d = 0$ and $d > \sigma_x > 0$. These correspond to the solutions for a single (red solid) and double droplet state (green solid), respectively, as shown in fig. (4.1b) for varying confinement f_y. For $f_y \gtrsim 200\,\mathrm{Hz}$ the ground state changes from the single-droplet to the double-droplet state. This confirms the presented idea of confinement-induced frustration leading to a density-modulated ground state.

We therefore expect to find ground states with even higher droplet numbers for increasing confinement. In order to confirm this behavior, we resort to exact numerical simulations which we use to compute the ground state as presented in ch. 2.5. Within the parameter range of fig. (4.1b), we indeed find states with a single (red dots), two (green squares) or even four droplets (blue diamonds) represented by exemplary insets showing the column density integrated along $\hat{\boldsymbol{z}}$. In the simulations, the transition from a single to a double droplet state occurs at a higher confinement[1] of 340 Hz.

Higher confinement along the droplet axis, see fig. (4.1c) for a state with $f_y = 800\,\mathrm{Hz}$, and higher atom number leads to a larger number of droplets in the ground state. Increasing the confinement further, we find a BEC phase without any density modulation.

In order to highlight that this is a general phenomenon, we eliminate the confinement along the $\hat{\boldsymbol{x}}$ direction and study the system with periodic boundary conditions. As shown in fig. (4.1d), we find the same transition to a density-modulated ground state, where we assume a linear density $n_x = 800\,\mu\mathrm{m}^{-1}$ and a harmonic potential with frequencies $f_x = 0$, $f_y = 800\,\mathrm{Hz}$ and $f_z = 1000\,\mathrm{Hz}$. In the BEC phase, this system features a continuous translational symmetry, which is broken by the transition to the density-modulated ground state. The corresponding length-scale is determined by the interplay of interactions and confinement along the polarization axis. In previous experiments, the ground state was always a single droplet because of the weak confinement [1, 2], although we observed multiple droplets.

The discovered density-modulated states are especially interesting, because they share a common phase throughout the stripes in the framework of the eGPE. Since the latter is free of fluctuations, which would likely break this phase link, we need to investigate the coherence properties with a different approach. Therefore we develop a more suited model based on the description of BECs in double-well potentials with tunable tunneling later. We note, that the ground states in fig. (4.1c,d) have a finite density between the

[1] The simple model of the variational ansatz does not take into account the exact potential landscape of the interaction with the neighboring droplet.

droplets, which would allow to establish the phase link, and turn to the experiment for now.

4.2. Tuning the mean-field DDI

In order to realize the necessary highly anisotropic trapping potentials experimentally we added a lightsheet with strong confinement along $\hat{\boldsymbol{z}}$, which is described in ch. 3.2. With this setup we gain the ability to tune the mean-field dipolar interaction, as defined in eq. (2.16). With a magnetic field along $\hat{\boldsymbol{z}}$ most of the atoms are in a side-by-side configuration where the DDI is repulsive, while it becomes attractive for a magnetic field perpendicular to $\hat{\boldsymbol{z}}$ in the lightsheet plane. In the first set of experiments we study this effect in a highly oblate cylindrical trap ($f_x \approx f_y \ll f_z$). Starting with the experimental cycle in ch. 3.3, we prepare a dBEC of ^{164}Dy with $\approx$ 5000 atoms at a temperature $T \approx 30\,\mathrm{nK}$ (30 % thermal fraction) and a magnetic field pointing along $\hat{\boldsymbol{z}}$. We then ramp up the lightsheet within 50 ms to increase the f_z confinement and simultaneously reshape the trap in the xy plane to the desired frequencies f_x and f_y with the infrared beams. As sketched in fig. (4.2a), we subsequently tilt the magnetic field at a constant amplitude B and rate $\dot{\beta} = 0.33\,\mathrm{deg/ms}$ by an angle β with respect to the $\hat{\boldsymbol{z}}$ axis[2].
Tilting the magnetic field, we observe magnetostriction, as explained in ch. 2.4. While the effect has been reported in time-of-flight experiments [32] with ^{52}Cr, this is the first in situ observation. As shown in fig. (4.2b), we subsequently observe a sharp transition at the angle β_c to a state with a single or double droplet configuration. In order to quantitatively define this angle, we utilize the Fourier transform of the acquired phase-contrast images. For an image I of the integrated density distribution, we compute the spectrum $|\mathcal{F}(I)|^2$ and sum all values in a band of width $\Delta k_{y(x)} = 4\,\mu\mathrm{m}^{-1}$ along the $\hat{\boldsymbol{x}}$ or $\hat{\boldsymbol{y}}$ axis, respectively. We then define the fourier anisotropy A_FT as the difference of these sums normalized by the sum over the disjunct area of both bands. This way, it only relies on the anisotropy of the fourier transform and is independent of atom number. We plot A_FT over the tilt angle β in fig. (4.2b) along with the empirical fit function $A_\mathrm{FT}(\beta) \propto \arctan\left(\frac{\beta-\beta_\mathrm{c}}{w}\right)$, which we use to extract both the critical angle β_c and width w for the transition to the droplet phase. We define the uncertainty of β_c by the quadratic sum of the fit error and the width w. With the presented approach, we have a reliable marker for the transition and avoid to use a fit function, that would need to cover both a single and a double droplet configuration.
For the first measurement in fig. (4.2c), we fix the magnetic field amplitude $B = 1240(5)\,\mathrm{mG}$

[2] We verified experimentally, that the acquired results do not change for tilt rates $\dot{\beta} \leq 0.4\,\mathrm{deg/ms}$.

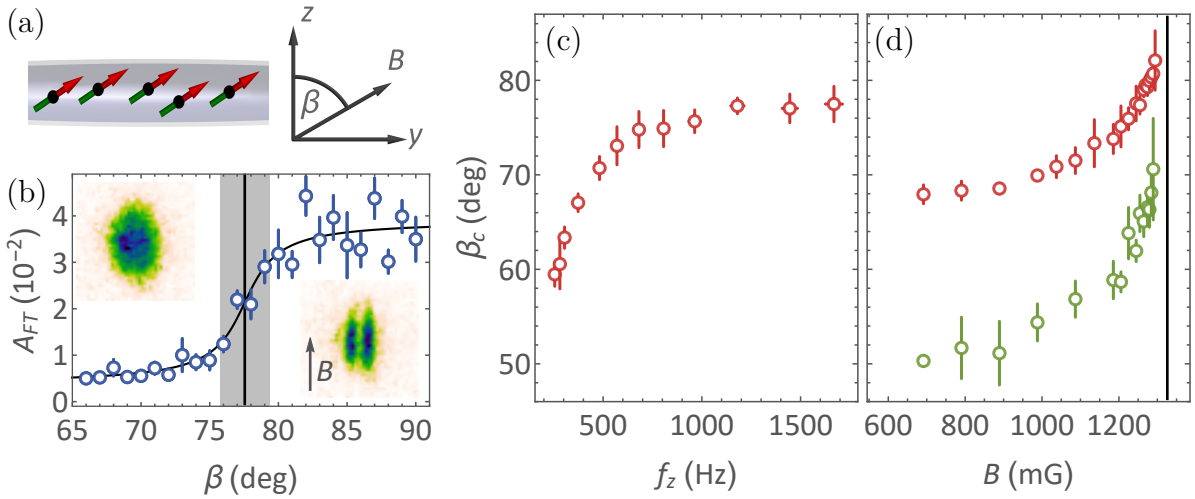

Figure 4.2.: **Tuning the mean-field dipolar interaction.** (a) Schematic of dipolar atoms strongly confined along the $\hat{\boldsymbol{z}}$ direction with a magnetic field tilted under an angle β with respect to the confinement axis. (b) Determination of the critical angle β_c via the Fourier anisotropy A_{FT}. The gray bar marks the corresponding error, insets show a BEC elongated by magnetostriction (left) and a double droplet state (right). (c) Critical tilt angle β_c over $\hat{\boldsymbol{z}}$ trap frequency for varying light sheet power and fixed magnetic field amplitude. In (d), the dependence on the scattering length is shown by changing the magnetic field B for $f_z = 950(10)\,\mathrm{Hz}$ (red) and $300(10)\,\mathrm{Hz}$ (green). The Feshbach resonance at $B_0 = 1326(3)\,\mathrm{mG}$ with width $\Delta = 8(5)\,\mathrm{mG}$ [1] is marked.

and measure the critical angle β_c for varying lightsheet confinement $f_z = 255(15)$ to $1669(43)\,\mathrm{Hz}$ in an almost cylindrical trap with transversal frequencies $f_x = 46(1) - 53(2)\,\mathrm{Hz}$ and $f_y = 46(1) - 60(2)\,\mathrm{Hz}$ in this range. Thus, the trap aspect ratio is $\lambda = f_z/\sqrt{f_x f_y} = 5.5(4) - 29.6(8)$. Within this configuration, β_c saturates for $f_z \gtrsim 900\,\mathrm{Hz}$, such that the dipolar interaction becomes independent of the confinement along $\hat{\boldsymbol{z}}$.

In a second set of experiments shown in fig. (4.2d), we choose a fixed confinement $f_z = 950(10)\,\mathrm{Hz}$ (red) and $300(10)\,\mathrm{Hz}$ (green) with $f_x = f_y = 50(5)\,\mathrm{Hz}$ and $48(5)\,\mathrm{Hz}$, respectively. We vary the magnetic field $B = 692(4)$ to $1294(4)\,\mathrm{mG}$ in the vicinity of a Feshbach resonance at $B_0 = 1326(3)\,\mathrm{mG}$ with width $\Delta = 8(5)\,\mathrm{mG}$ [1]. According to $a_\mathrm{s}/a_\mathrm{bg} = 1 + \Delta/(B_0 - B)$ [71] we therefore tune the scattering length in the range $a_\mathrm{s}/a_\mathrm{bg} = 1.01$ to 1.25. Approaching the Feshbach resonance, the critical angle β_c increases for both curves and seems to diverge close to the resonance, which is reminiscent of the scaling of the scattering length in this region. The obvious upper limit is $\beta_\mathrm{c} = 90\,\mathrm{deg}$ with $a_\mathrm{s} > a_\mathrm{dd}$, where the condensate is stable for any field direction.

With these two measurements we demonstrate the tuneability of the mean-field dipolar interaction Φ_dd. Due to the strong confinement, we can prepare a stable BEC initially and

then drive the transition to the droplet phase by this magnetic field tilt in a controlled way.

4.3. Metastable states in the experiment

In the next set of experiments, we approach the setting of the theory section in order to investigate the predicted states. Therefore, we use the procedure of the previous section and additionally reshape the trapping potential in the xy plane prior to the magnetic field tilt. We vary the transversal trap aspect ratio $\lambda_{xy} = f_x/f_y = 0.19$ to 2.36, such that the mean trap frequency $\bar{f} = (f_x f_y f_z)^{1/3}$ is kept constant. With a fixed $f_z = 945(5)\,\mathrm{Hz}$, we adjust the transversal frequencies in the range $f_x = 25(1) - 75(2)\,\mathrm{Hz}$ and $f_y = 128(2) - 32(1)\,\mathrm{Hz}$.

Above the critical angle, we observe states with one to four droplets with a total atom number of 1000-3000 and an additional $\approx$ 6000 thermal atoms. In fig. (4.3) we show exemplary single-shot in situ images for various aspect ratios, as well as the mean number of droplets (blue) averaged over 11 realizations in dependence of the aspect ratio λ_{xy} and the tilt angle β. We integrate the images along the vertical direction $\hat{\boldsymbol{y}}$ and use a peak detection algorithm counting the number of droplets. While the critical tilt angle β_c (red dots) is almost independent of the aspect ratio, the number of droplets increases with decreasing λ_{xy}. For $\lambda_{xy} > 1$ the trap is elongated along the projection of the polarization axis in the xy plane, and a single droplet forms. For $\lambda_{xy} < 1$, we frustrate the system along this direction, which leads to the creation of multiple droplets. For $\beta \gg \beta_\mathrm{c}$, the finite droplet lifetime lowers the mean droplet number due to three-body losses[3]. Unlike in the previous droplet experiments, we hereby gain control of the number of droplets we create with this sequence.

As expected from the theoretical investigation the number of droplets increases with larger confinement f_y, i.e. for smaller λ_{xy}, along the magnetic field component in the plane. We confirm this scenario with numerical simulations of the experimental sequence starting with $N = 5000$ atoms. Other parameters are the scattering length $a_\mathrm{s} = 70\,a_0$ and the loss coefficient $L_3 = 1.25 \times 10^{-41}\,\mathrm{m}^6/\mathrm{s}$ [3], which we report in appendix B. We thereby prepare a BEC at a magnetic field angle $\beta \ll \beta_c$ via imaginary-time evolution of the eGPE. Subsequently, the angle is tilted at a constant speed of $\dot{\beta} = 0.33\,\mathrm{deg/ms}$ in real-time evolution. At the critical angle β_c we observe the transition to one or multiple droplets depending on the transversal trap aspect ratio λ_{xy}. A marker for this transition is the combined two-body energy E_con+E_dip that becomes negative for $\beta \geq \beta_c$ (red dots).

[3] At the given tilt rate $\dot{\beta}$, it takes 60 ms to cover the range $\beta = 70 - 90\,\mathrm{deg}$.

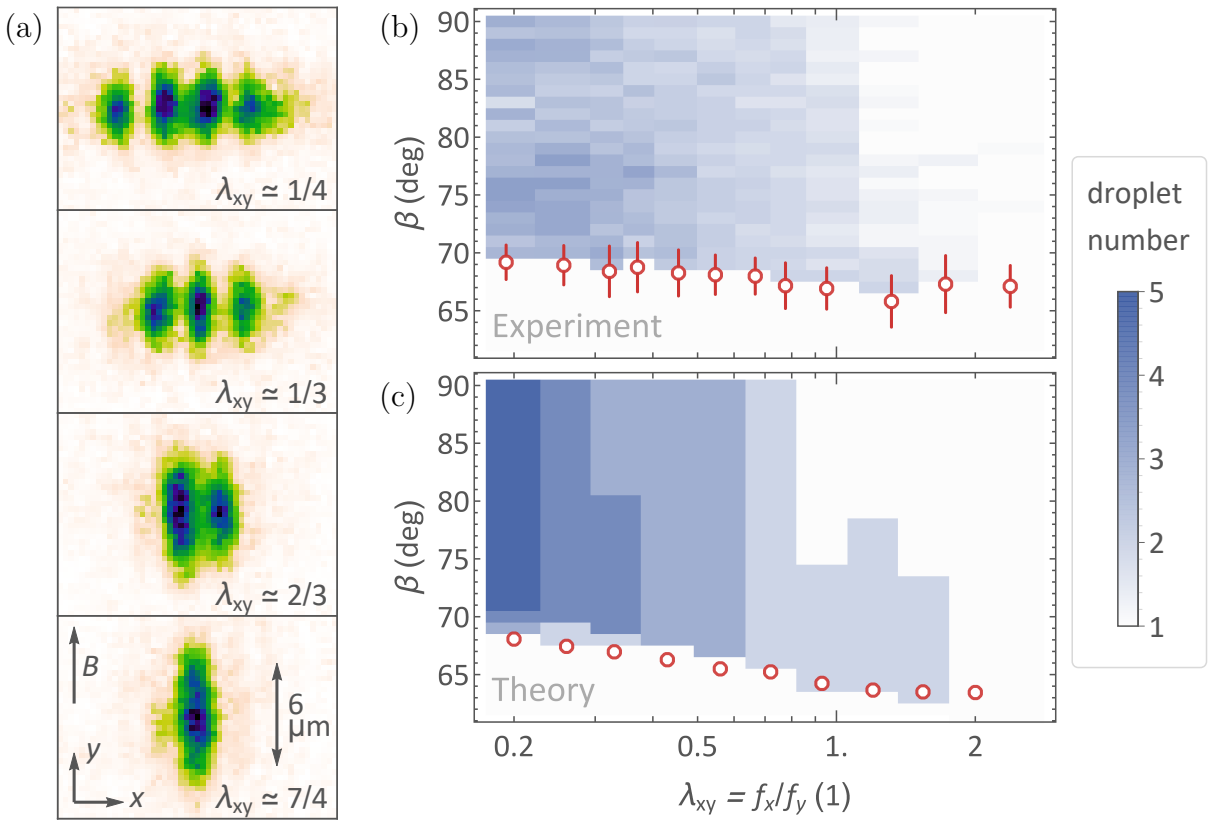

Figure 4.3.: **Striped states observed in an anisotropic trap.** (a) Example single-shot in situ images for varying transversal trap aspect ratio $\lambda_{xy} = f_x/f_y$. (b) Critical tilt angle β_c (red circles) and average number of droplets over λ_{xy}. We observe multiple droplets for $\lambda_{xy} \lesssim 1$ and single ones for $\lambda_{xy} \gtrsim 1$. Data is taken for $B = 905(5)\,\mathrm{mG}$ at a trap frequency of $f_z = 945(5)\,\mathrm{Hz}$ and averaged over 11 realizations. (c) Dynamic simulations of the eGPE confirm the creation of multiple droplets for conditions where a single droplet is the ground state. Simulation parameters are similar to the experiment, see main text.

The simulations, which are shown in fig. (4.3c), recreate all features of the experiment and shows overall good agreement. The number of droplets is slightly higher, which we attribute to the choice of the starting atom number and the loss coefficient, since the number of droplets increases with larger atom number at the time of droplet creation, i.e. for $\beta = \beta_c$. Due to atom loss of the single droplets two of these can merge into a single one, lowering the droplet atom number for $\beta \gg \beta_c$.

Although we observe these striped states experimentally and recreate the behavior within the framework of the eGPE, the ground state for the experimental parameters is still a single droplet, which we obtain via imaginary-time evolution of the eGPE. Since the fragmentation is a dynamic effect of the eGPE, we conclude that the BEC undergoes

the modulational instability, which we explained in ch. 2.5.2 and observed in previous publications [1, 2, 4]. Here, we induce the instability by the modification of the DDI rather than the scattering length. Therefore, the observed states are likely excited metastable states, since the strong repulsion between neighboring droplets prevents a decay to the ground state. We emphasize, that this modulational instability prohibits the preparation of the ground state in general. Additionally, there is no straight-forward way to determine whether an experimental state is the ground state.

4.4. Coherence Properties

Although we cannot prepare a striped ground state experimentally, we are able to create multi-droplet states, that might feature similar coherence properties as the predicted states. In prior experiments [2], where we observed fringe patterns, we confirmed a coherent phase relation extending throughout the droplet. In the following, we therefore focus on the phase relation between neighboring droplets focusing on the simplest realization of two droplets. In close analogy to the physics of condensates in double-well potentials [171], we therefore conduct interference experiments. For two wave packets with local phase θ_1 and θ_2, the interference pattern after expansion results in a fringe pattern with a phase $\theta = \theta_2 - \theta_1$ relative to the envelope. To ensure, that this simple behavior is not modified by an additional long-range interaction, we conducted numerical expansion simulations for the experimental parameters, which confirm this scenario.
With the methods described in the previous sections, we prepare a state with two droplets and let them expand for 8 ms. For the experimental parameters, the droplet is close to the self-bound regime [3], where the radial expansion is slow. Thus, we intentionally "blow up" the droplets by increasing the scattering length with a magnetic field ramp from $B = 1245(5)\,\mathrm{mG}$ to $B = 1313(5)\,\mathrm{mG}$ during the first 2 ms of the expansion. With absorption imaging, we then obtain interference images like the ones shown in fig. (4.4a), where the fringe spacing is well above the optical resolution. In order to analyze these, we integrate along the polarization direction $\hat{\boldsymbol{y}}$ and fit the function

$$n_{\mathrm{int}}(x) \propto \Big[1 + v\cos(k(x - x_0) + \theta)\Big] \exp\left(-\frac{(x - x_0)^2}{2\sigma^2}\right) \tag{4.6}$$

corresponding to a cosine-modulated Gaussian. This way, we obtain the central position x_0 and width σ of the Gaussian as well as the fringe visibility $v \in [0, 1]$ and relative phase $\theta \in [0, 2\pi)$ of the modulation. By definition, θ is thus given by the phase of the fringe pattern with respect to the distribution's center of mass. In fig. (4.4b), we show

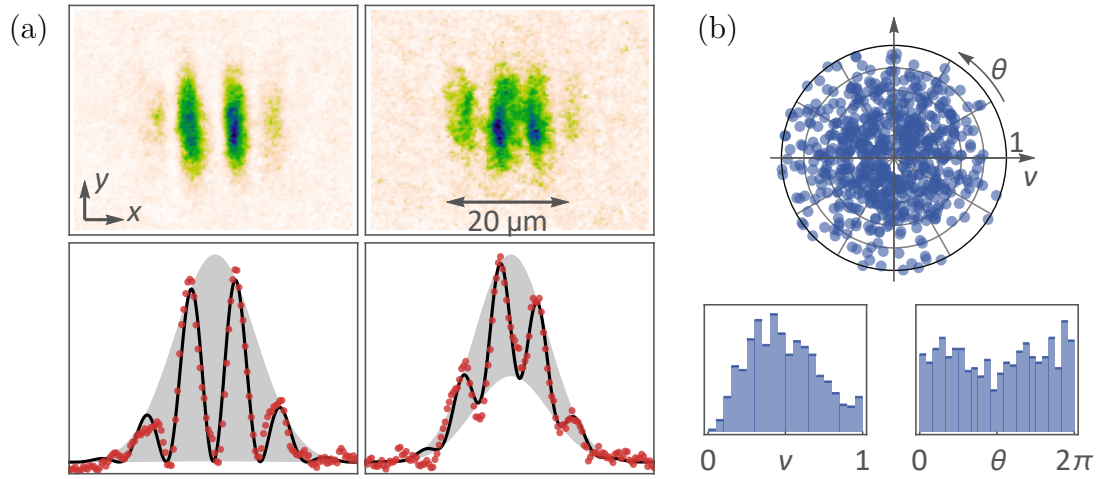

Figure 4.4.: **Interference patterns after 8 ms of expansion.** (a) Two example realizations with absorption image (top) and integrated density (bottom) showing fringes. We extract the phase θ with respect to the center of mass of the distribution. (b) Polar plot and histograms of relative phase θ and visibility v for 650 atom distributions. There is no preferred phase visible indicating that there is no phase coherence between the droplets.

650 experimental realizations (v, θ) starting from a $\lambda_{xy} = 1/4$ trap with 3 or 4 droplets initially. For a phase-coherent sample we would expect a preferred value of the phase, which is clearly not visible in the data. A configuration with only two droplets shows the same random distribution of relative phase θ and therefore no sign of phase coherence. The absence of a fixed phase relation between droplets is caused by the modulational instability, we discussed in ch. 2.5.2. Its stochastic nature leads to fluctuations in the atom number of neighboring droplets and additional phase noise. The difference in chemical potential then results in a random relative dephasing of the droplets.

Nevertheless, the desired phase link could be established by tunneling of atoms. In order to describe this effect, we exploit the framework of bosonic Josephson junctions [171, 172]. Using the variational ansatz in eq. (4.2) for two droplets, we develop a two-state model along the lines of [172], that was also used to study self-induced bosonic Josephson junctions of dBECs in toroidal traps [173]. Within this framework, we define the wavefunction

$$\phi_{1,2} = \frac{1}{\pi^{3/4}\bar{\sigma}^{3/2}} \exp\left(-\frac{(x \pm d/2)^2}{2\sigma_x^2} - \frac{y^2}{2\sigma_y^2} - \frac{z^2}{2\sigma_z^2}\right) \tag{4.7}$$

normalized to $\int \mathrm{d}^3 r \, |\phi_{1,2}|^2 = 1$. The model yields the on-site interaction term

$$\begin{aligned} E_\mathrm{C} &= \int \mathrm{d}^3 r \left[g \, |\phi_1|^4 + g_\mathrm{qf} \sqrt{\frac{N}{2}} \, |\phi_1|^5 + \left(|\phi_1|^2 + |\phi_2|^2 \right) \int \mathrm{d}^3 r' V_d \, |\phi_1'|^2 \right] \\ &= g \frac{1}{(2\pi)^{3/2} \bar{\sigma}^3} + g_\mathrm{qf} \frac{2 N^{1/2}}{5^{3/2} \pi^{9/4} \bar{\sigma}^{9/2}} - g_\mathrm{dd} \frac{f(\kappa_x, \kappa_y) + \mathcal{I}_\mathrm{dip}(\kappa_x, \kappa_y, u)}{(2\pi)^{3/2} \bar{\sigma}^3} \end{aligned} \tag{4.8}$$

with on-site contributions for the contact and dipolar mean-field interactions as well as a beyond-mean-field term. Being long-range, we additionally include the dipolar inter-site interaction. In contrast, the tunneling term

$$\begin{aligned} E_\mathrm{J} &= N \int \mathrm{d}^3 r \, \phi_1 \left(-\frac{\hbar^2 \nabla^2}{2m} + V_\mathrm{ext} \right) \phi_2 \\ &= -\frac{\hbar^2 N}{4m} \exp\left(-\frac{u^2}{4} \right) \left[\sum_{k=x,y,z} \left(\sigma_k^{-2} + \frac{m^2 \omega_k^2}{\hbar^2} \sigma_k^2 \right) - \frac{u^2}{2\sigma_x^2} \right] \end{aligned} \tag{4.9}$$

is a measure for the wavefunction overlap. Hence, it scales exponentially with the rescaled distance $u = d/\sigma_x$. With these terms at hand, we can estimate the energy scales of both quantum and thermal fluctuations in comparison to the tunneling energy. Within this simple analysis, the phase link between two droplets should be robust against phase fluctuations due to quantum noise for $|E_\mathrm{J}/E_\mathrm{C}| > 1$ and $E_\mathrm{J}/k_\mathrm{B}T > 1$ for thermal fluctuations [174]. With dipolar quantum droplets, E_C can be negative due to the dipolar interaction and takes very low values of $|E_\mathrm{C}| \ll 1\,\mathrm{nK}$. For the experimental parameters shown here, the hopping term $E_\mathrm{J} \ll 1\,\mathrm{nK}$ is negligible compared to the finite temperature of $T \sim 50\,\mathrm{nK}$ in the experiment. This prediction matches our experimental observation of a random distribution of relative phases.

In order to increase the tunneling, we propose to tune the trap frequency f_x along the tunneling direction, see fig. (4.5). For $f_x \ll f_z$, the droplet sizes are hardly affected and the on-site term E_C is almost constant. In contrast, we can control the distance between the droplets, which allows to tune the tunneling term E_J by six orders of magnitude well above the competing energy scales. To the far right, the corresponding frequency is $E_\mathrm{J}/h > 1\,\mathrm{kHz}$, which corresponds to tunneling times much faster than the lifetime of $\sim 300\,\mathrm{ms}$ for a trapped droplet.

Yet, we need to highlight the conceptual difference compared to contact-interacting BECs in fixed double-well potentials. For the quantum droplet, the trapping potential of a single particle is given by the interplay of interactions. As we have seen in fig. (2.12), the wavefunction can significantly deviate from a Gaussian with a well-known scaling away

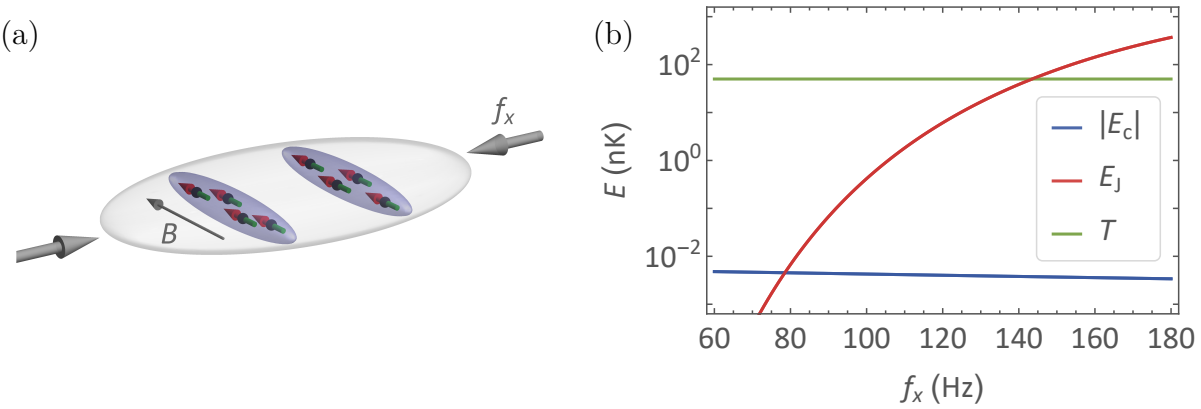

Figure 4.5.: **Tuning the coherence properties.** On-site interaction E_C (red) of eq. (4.8) and hopping term E_J (green line) of eq. (4.9) for varying confinement f_x perpendicular to the magnetic field. This way the distance between droplets is varied and thus E_J can be tuned over several orders of magnitude. The shape of the droplet wavefunction is not altered keeping E_C almost constant. The values are computed with the variational ansatz for $N = 10^4$ atoms and a confinement $f_y = 300\,\mathrm{Hz}$, where the double-droplet solution is the ground state. We also show the typical temperature $T = 50\,\mathrm{nK}$ of the experiment.

from the droplet at $x > \sigma_x$. With the tunneling term depending on the wavefunction overlap, we therefore need to investigate the double-droplet system numerically.
For this purpose, we prepare a double droplet state with $N_\mathrm{d} = 2000$ atoms each, which is the ground state in a trap with frequencies $f_x = 100\,\mathrm{Hz}$, $f_y = 1000\,\mathrm{Hz}$, and $f_z = 500\,\mathrm{Hz}$. To describe the dynamics, we define the atom number imbalance $z = (N_1 - N_2)/(N_1 + N_2)$ for the two droplets with numbers N_1 and N_2 as well as the relative phase θ. The time-evolution with fixed $z = 0$, $\theta = 0$ of the system in the ground state is trivial. At $t = 0\,\mathrm{ms}$, we set the number imbalance to $z = 0.1$, which is a typical number we observe in the experiment, in order to bring the system out of equilibrium and induce the dynamics. With a distance of $d \approx 2.0\,\mu\mathrm{m}$, there is negligible tunneling and the number imbalance z is preserved, see blue line in fig. (4.6a). Consequently, the difference in chemical potential leads to dephasing, such that the relative phase θ increases linearly at a constant rate. Residual oscillations stem from the breathing motion of the droplets. This behavior is thus compatible with the experimental observation of an incoherent sample. In order to re-establish phase coherence, we thus proposed to increase the trap frequency f_x. Therefore, we prepare the previously described state at $f_x = 100\,\mathrm{Hz}$ and in the time $t = 0 - 100\,\mathrm{ms}$ linearly increase the transversal trapping to frequencies of $f_x = 180$ (red), 210 (green) or 230 Hz (yellow) and follow the evolution for another 100 ms. Thereby we lower the inter-droplet spacing[4], which leads to oscillations of the number imbalance z and complex

[4] The equilibrium distances are 1.4, 1.3 and 1.2 µm, respectively, for the described frequencies f_x.

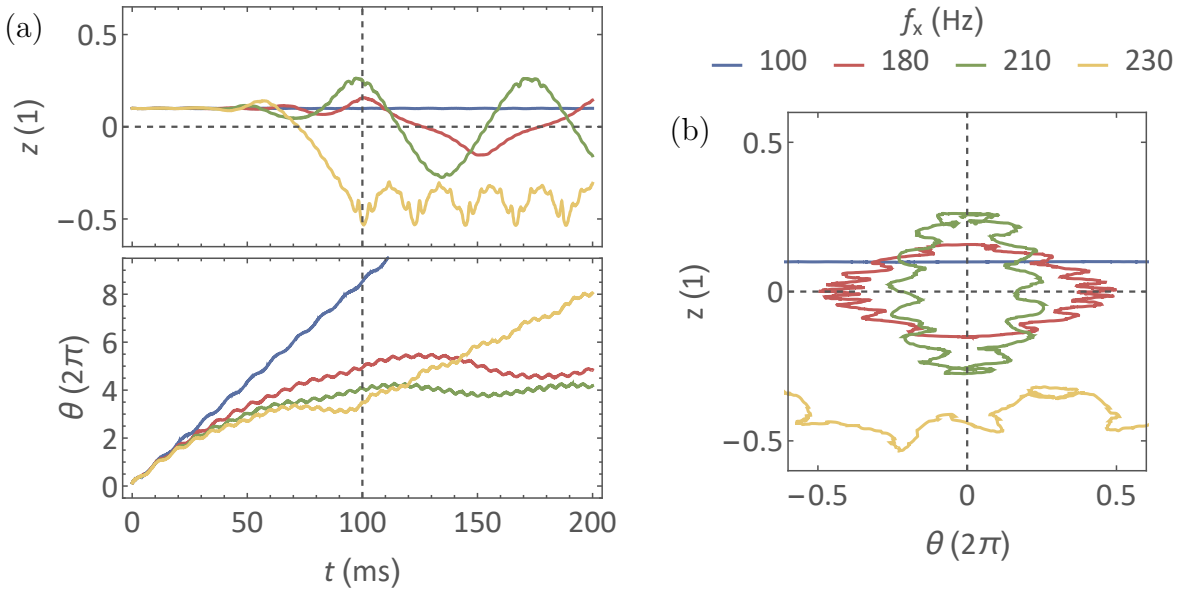

Figure 4.6.: **Coherence properties in simulations.** (a) Evolution of atom number imbalance z and relative phase θ for two droplets with $N = 4000$ atoms in total and an initial imbalance $z = 0.1$. Within the first 100 ms, the transversal trapping f_x is ramped from 100 Hz to various final values inducing the dynamics. (b) Phase-space representation (θ, z) for the last 100 ms with re-centered phase θ. For final frequencies of $f_x = 180$ and 210 Hz we observe coherent Josephson oscillations.

behavior of the relative phase θ, as shown in fig. (4.6a).

Inspired by [172], we classify the dynamics in the phase-space representation (θ, z) in fig. (4.6b), which we extract for the time $t = 100 - 200$ ms with a constant trapping potential. For negligible tunneling, e.g. $f_x = 100$ Hz (blue), the droplets behave classically with a relative phase independent of the number imbalance. For 180 (red) and 210 Hz (green), we obtain coherent *Josephson oscillations* between phase and number imbalance, described by an ellipse in this representation[5]. In this coherent regime, we find frequencies of up to ~ 15 Hz for the exchange of particles and phase. As a consequence, the intrinsic relationship dictates a small initial number imbalance z in order to realize small fluctuations of the relative phase θ. A larger confinement f_x gives a faster frequency due to increased tunneling rates with a "squeezed" relative phase, but also leads to an increased variation of the number imbalance, that finally results in *self-trapping* of the droplets. In this regime, exemplified by $f_x = 230$ Hz (yellow), a small droplet coexists next to a larger one with little variation around $z \approx -0.4$. Due to the large difference in chemical potential, this again leads to dephasing.

[5] As mentioned, residual oscillations are due to the droplets "bouncing" in the trap.

The situation is different, when we introduce three-body losses to this process. For the investigated parameters in the range $f_x = 180$ to $230\,\mathrm{Hz}$, phase-coherent states with a relative phase $\theta \approx \pi$ in conjunction with small oscillations on the number imbalance $z < 0.05$ seem to emerge. For lower confinement of $f_x = 100\,\mathrm{Hz}$ the two droplets merge into a single one. Although it seems to contradict our previous observations, such a phase locking was also predicted for BECs in double-well potentials [172]. Yet, in order to properly understand this effect, a systematic numerical study over a wider parameter range is necessary.

Chapter 5

Scissors mode of a droplet

Atomic nuclei exhibit giant dipole resonances, which were observed in the 1950s [175, 176]. In a semi-classical picture these correspond to an out-of-phase *electric* dipole oscillation of the proton with respect to the neutron density distributions. In an attempt to generalize this idea for deformed nuclei with anisotropic nucleon distributions, a simple rigid-rotor model was formulated in the 1980s [177]. It predicted a *magnetic* dipole resonance, that was then measured in ^{156}Gd [178], and later coined the *scissors mode*. Within this picture, it corresponds to a rotational out-of-phase oscillation of the proton with respect to the neutron density distribution, as sketched in fig. (5.1a). The Hamiltonian features a potential $V = \frac{1}{2}c\theta^2$ of a torsion spring at angle θ, which couples the proton and neutron density distributions. The spring constant c is determined by the separation energy of both constituents, which also gives rise to the asymmetry term in the semi-empirical mass formula [179]. Typical resonance frequencies are $\sim 10^{21}$ Hz with angles of a few degrees.

In the context of ultracold atoms, an analogue of the scissors mode was predicted for contact-interacting BECs in an anisotropic trap [180]. For this system, the rotation under an angle θ of the anisotropic atomic density distribution with respect to the trap symmetry axis, gives rise to a similar term $\propto \theta^2$ within linear response. Therefore, a sudden rotation of the latter results in an oscillation of the density distribution with respect to the fixed trapping potential, see fig. (5.1b).

For such a rotating system[1], the moment of inertia Θ determines the oscillation frequency. Due to its irrotational character the moment of inertia of the superfluid differs from the classical rigid-body value, which makes measurements of the scissors mode important markers for superfluidity independent of the microscopic details of the system [60, ch. 14]. By measurements of the scissors mode frequency, the occurrence of superfluidity in

[1] For simplicity, we assume a differential equation $\Theta\ddot{\theta} = -\tilde{c}\,\theta$ with resonance frequency $\omega_0 = \sqrt{\tilde{c}/\Theta}$.

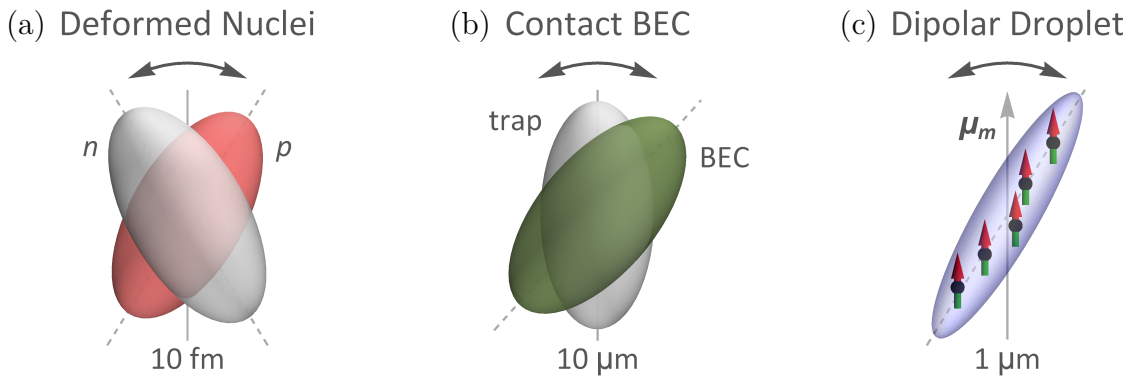

Figure 5.1.: **Systems possessing a scissors mode** along with the typical system size. (a) In deformed nucleii, the scissors mode corresponds to an rotational out-of-phase oscillation of both the proton (red) and neutron (white) density distributions. (b) For a contact interacting BEC, the symmetry axis of the density distribution (green) rotates with respect to the anisotropic trapping potential (white). (c) For a dipolar BEC or quantum droplet the density distribution oscillates with respect to the polarization axis. Angles are exaggerated for clarity, (a) and (b) are adapted from [179, fig. 56].

deformed heavy nucleii [181] and contact-interacting BECs [140] have been confirmed. For dipolar condensates, the scissors mode is conceptually different from the latter, since the dipolar interaction breaks the rotational symmetry. Thus, the density distribution oscillates with respect to the polarization axis, as shown in fig. (5.1c). Based on our publication [7], we develop the description of the scissors mode for dipolar quantum droplets and present its measurements in this chapter. First, we review the sum-rule approach to derive the scissors mode frequency. Experimentally, we modulate the magnetic field angle to drive the scissors mode of a trapped droplet. In addition, we excite the lowest-lying collective mode of the droplet by a diabatic rotation of the magnetic field angle. By comparison to the equations of motion derived in ch. 2.4.4, from these measurements we finally extract a value of $a_{\mathrm{bg}} = 69(4)\, a_0$ for the background scattering length of ^{164}Dy.

5.1. Sum-rule approach

While we introduced an analytical approach to derive the scissors mode frequency in ch. 2.4.4, we outline a more elegant derivation based on *sum rules* developed by our collaborators M. Isoard and S. Stringari.
Like in the experiment, we consider the polarization axis along $\hat{\boldsymbol{y}}$ breaking the rotational invariance in the xy plane due to magnetostriction, see ch. 2.4.2. In this setting, the scissors mode corresponds to an angular oscillation around $\hat{\boldsymbol{z}}$, which is excited by the

angular momentum operator

$$\hat{L}_z = \sum_{k=1}^{N} \left(r_x\, p_y - r_y\, p_x\right)_k \tag{5.1}$$

for N particles. Employing linear response theory [60, ch. 7], we define the moments

$$m_k = \hbar^{k+1} \int_{-\infty}^{+\infty} \mathrm{d}\omega\, \omega^k S(\omega) \tag{5.2}$$

of the dynamic structure factor $S(\omega)$ for the angular momentum operator. This approach yields a rigorous upper bound

$$\hbar\omega_{\mathrm{sc}} = \sqrt{\frac{m_1}{m_{-1}}} \tag{5.3}$$

for the scissors mode frequency. In general, the moments can only be evaluated by solving the Schrödinger equation for the corresponding Hamiltonian. Fortunately, there is a sum rule relating the energy-weighted moment m_1 to the set of commutators $\frac{1}{2}\left\langle[\hat{L}_z,[\hat{H},\hat{L}_z]]\right\rangle$. For the Hamiltonian we assume a cylindrical trapping potential in the xy plane, such that only the dipolar interaction breaks the rotational symmetry and all other terms commute with $\hat{L}_z$. This way, we obtain

$$m_1 = \frac{\hbar^2}{2}\Big(\langle V_{\mathrm{dd}}^x\rangle - \langle V_{\mathrm{dd}}^y\rangle\Big) \qquad \text{with} \qquad V_{\mathrm{dd}}^\alpha(\boldsymbol{r}) = \frac{\mu_0\mu_{\mathrm{m}}^2}{4\pi}\frac{1-3\alpha^2/r^2}{r^3} \tag{5.4}$$

corresponding to eq. (2.7) for dipoles oriented along the axis $\alpha = \{x, y, z\}$ and the expectation value defined as $\langle A\rangle = \int \mathrm{d}\boldsymbol{r}'\mathrm{d}\boldsymbol{r}\, n(\boldsymbol{r})A(\boldsymbol{r}-\boldsymbol{r}')n(\boldsymbol{r}')$. Using the gaussian ansatz of eq. (2.37) for three dimensions, the moment finally reads

$$m_1 = \frac{\hbar^4 N^2}{\sqrt{2\pi}m\bar{\sigma}^3}\, a_{\mathrm{dd}} \left[f\Big(\frac{\sigma_x}{\sigma_y},\frac{\sigma_z}{\sigma_y}\Big) - f\Big(\frac{\sigma_y}{\sigma_x},\frac{\sigma_z}{\sigma_x}\Big)\right] \tag{5.5}$$

with the geometry-dependent function $f(\kappa_1,\kappa_2)$ defined in eq. (4.4). In contrast, the inverse energy-weighted moment is determined by the static response of the system to a perturbation of form $-\omega\hat{L}_z$. It is therefore given by the moment of inertia

$$\Theta = 2m_{-1} = \frac{1}{2}mN\frac{\left(\sigma_y^2-\sigma_x^2\right)^2}{\sigma_y^2+\sigma_x^2} \tag{5.6}$$

evaluated with the gaussian ansatz for a superfluid. Finally, we obtain

$$\omega_{\mathrm{sc}}^2 = \frac{4\hbar^2 N a_{\mathrm{dd}}}{\sqrt{2\pi} m^2 \bar{\sigma}^3} \frac{\sigma_y^2 + \sigma_x^2}{\left(\sigma_y^2 - \sigma_x^2\right)^2} \left[f\left(\frac{\sigma_x}{\sigma_y}, \frac{\sigma_z}{\sigma_y}\right) - f\left(\frac{\sigma_y}{\sigma_x}, \frac{\sigma_z}{\sigma_x}\right) \right] \tag{5.7}$$

for the frequency of the scissors mode of an anisotropic dBEC in an isotropic trap. In contrast to the contribution

$$\omega_{\mathrm{sc}}^2 = \frac{\sigma_y^2 + \sigma_x^2}{\sigma_y^2 - \sigma_x^2} \left(\omega_x^2 - \omega_y^2\right) \tag{5.8}$$

from an anisotropic trap breaking the symmetry [180], the former scales with both atom number and dipolar interaction strength.

For a contact-interacting BEC, there is no dipolar interaction ($a_{\mathrm{dd}} = 0$), which results in a size σ_k determined by the trap frequency $\omega_k \propto 1/\sigma_k$. The scissors mode frequency in eq. (5.8) above then reduces to $\omega_{\mathrm{sc}}^2 = \omega_x^2 + \omega_y^2$, which was measured in [140] with a BEC of ^{87}Rb. For a thermal gas, a damped oscillation at two frequencies $|\omega_x \pm \omega_y|$ was observed. The lower frequency stems from the rotational character of the classical gas, as noted in [180]. This experiment was therefore a strong hint for superfluidity of the interacting BEC.

In the following experiments, we are interested in the dipolar contribution in eq. (5.7) and thereby use a cylindrical trap ($\omega_x = \omega_y$), where the contribution from eq. (5.8) vanishes.

5.2. Measuring the scissors mode

Experimentally, we use the method developed in the previous chapter to prepare a single dipolar quantum droplet of ^{164}Dy in a cylindrically symmetric trap with $f_x = f_y = 40(1)\,\mathrm{Hz}$ and $f_z = 950(20)\,\mathrm{Hz}$. After the preparation procedure, the magnetic field points along $\hat{\boldsymbol{y}}$ with a fixed magnitude $B_0 = 800(5)\,\mathrm{mG}$. Due to the strong transverse confinement the droplet phase with a smaller extent along $\hat{\boldsymbol{z}}$ compared to a gaseous condensate is energetically favored. Thus, droplets exist for lower atom numbers compared to a spherical trap due to the strong transverse confinement. Additionally, there are solition solutions, which are stabilized by quantum pressure irrespective of quantum fluctuations, see the phase diagram in [7, Supp. Mat.]. The measurements presented here are carried out in the quantum droplet phase. After the preparation, we parametrically excite the scissors mode by modulating the transverse magnetic field $B_x(t) = B_{x,0} \sin(2\pi f_{\mathrm{mod}} t)$, with an amplitude $B_{x,0} \leq 200\,\mathrm{mG}$ and a frequency f_{mod}. The magnetic field angle in the xy plane is then

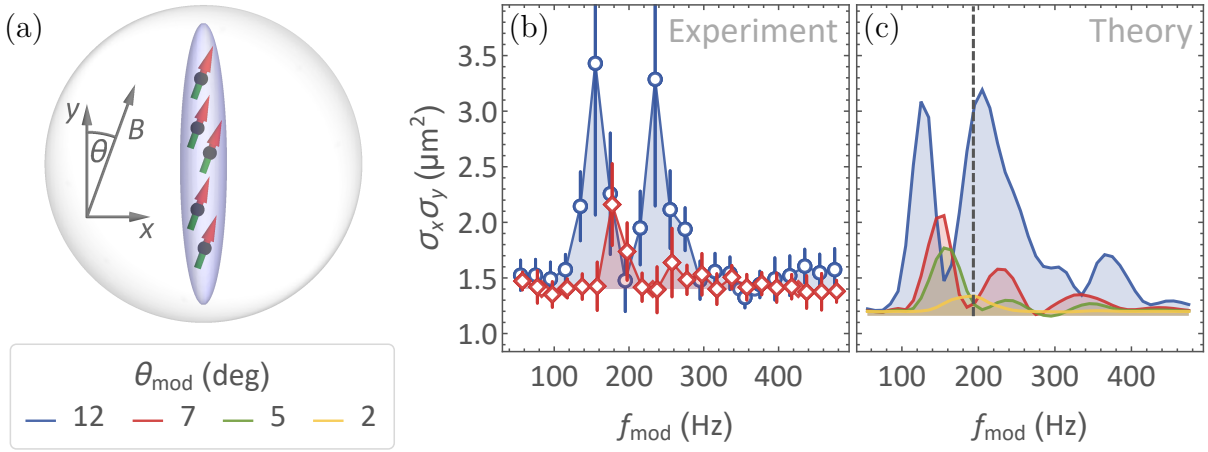

Figure 5.2.: **Exciting the scissors mode.** (a) Sketch of the dipolar droplet in a cylindrical trap, where we modulate the magnetic field angle $\theta(t) \approx \theta_{\mathrm{mod}} \sin(2\pi f_{\mathrm{mod}} t)$. (b) Experimental spectra of the area $\sigma_x\sigma_y$ over a range of modulation frequencies for $\theta_{\mathrm{mod}} = 12\,\mathrm{deg}$ (blue) and $7\,\mathrm{deg}$ (red). (c) Spectra obtained by numerically solving the equations of motion corresponding to eq. (2.43) for the experimental procedure and a scattering length $a_{\mathrm{s}} = 68\,a_0$, see main text. The scissors mode frequency of eq. (5.7) (dashed line) derived in the linear regime coincides with the small-angle response for $\theta_{\mathrm{mod}} = 2\,\mathrm{deg}$ (yellow).

approximated by $\theta(t) \approx B_x(t)/B_0 = \theta_{\mathrm{mod}} \sin(2\pi f_{\mathrm{mod}} t)$, as sketched in fig. (5.2a). In the droplet phase the density is high and the droplet atom number decays from 750 initially to 400 within $\sim 150\,\mathrm{ms}$ due to three-body losses. Therefore we restrict the modulation time to $\Delta t = 20\,\mathrm{ms}$, for which the atom number variations $\Delta N/N \leq 0.1$ are still small. This way, the measurement resolution is fourier-limited to $\Delta f \sim 1/\Delta t = 50\,\mathrm{Hz}$. In order to keep the energy of the "excitation pulse" fixed, we rescale the modulation amplitude $\tilde{\theta}_{\mathrm{mod}} = \theta_{\mathrm{mod}} \sqrt{\frac{100\,\mathrm{Hz}}{f_{\mathrm{mod}}}}$ with the drive frequency f_{mod}.

After the modulation sequence, we image the density distribution via phase-contrast imaging. A Gaussian fit of the form $n(x,y) = \frac{N}{\pi\sigma_x\sigma_y} \exp\left[-x^2/\sigma_x^2 - y^2/\sigma_y^2\right]$ to the central region of the cloud then yields the atom number N as well as the sizes σ_x and σ_y in the imaging plane. We thereby assume a constant density distribution of the remaining thermal fraction in this region. A fit of the sum of two Gaussians for both the droplet and thermal distribution typically gives a lower droplet atom number, differing by 25 % on average. We only quote the former method here, since it is more robust, and account for this effect with a systematic uncertainty $\Delta N/N = 0.25$ on the number of condensed atoms within the droplet. The finite resolution of our imaging system with $1\,\mu\mathrm{m}$ according to the Rayleigh criterion [109, ch. 4], puts a lower limit on the extracted transverse size $\sigma_x \approx 0.6\,\mu\mathrm{m}$ of the droplet with a calculated size of $\approx 0.3\,\mu\mathrm{m}$. Along the other axis, the size is $\sigma_y \sim 1.5\,\mu\mathrm{m}$ typically. The limited excitation time and optical resolution make it

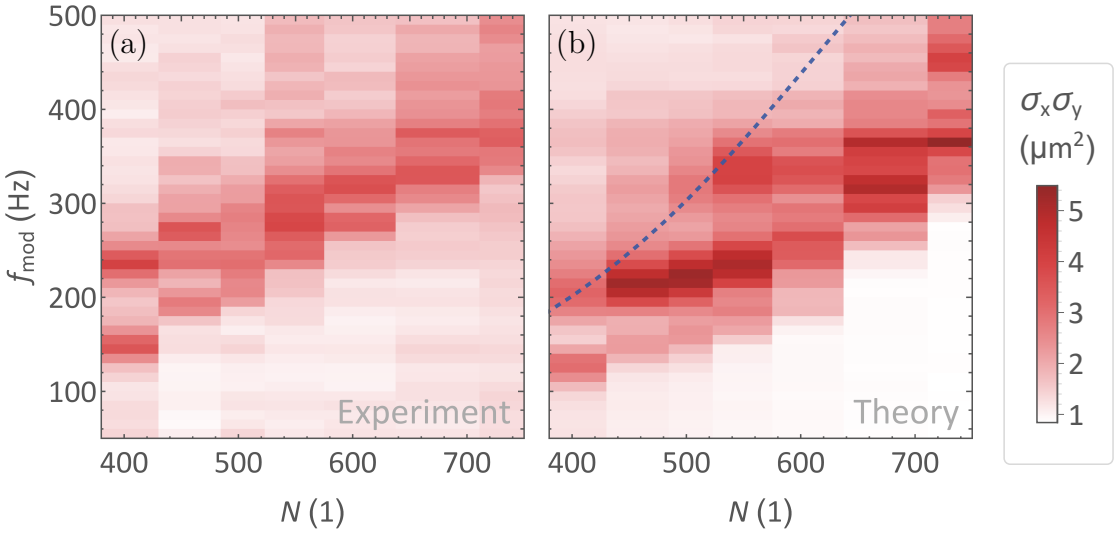

Figure 5.3.: **Modulation frequency over atom number.** (a) Experimental spectra of the droplet area $\sigma_x\sigma_y$ for various atom numbers. (b) Time-dependent theory according to eq. (2.43) for a scattering length $a_s = 68\,a_0$. The dashed line shows the scissors mode frequency of eq. (5.7).

necessary to use large excitation amplitudes θ_{mod} of 7 deg or 12 deg in order to observe an effect, which is clearest in the area $\sigma_x\sigma_y$ of the droplet, where an excitation should lead to a larger value. In fig. (5.2b), we show an example spectrum for a droplet atom number $N = 390(100)$, where multiple peaks appear with a position depending on the modulation amplitude.

As expected, the sum rule approach resulting in eq. (5.7) is only valid in the linear regime. Therefore we derived the equations of motion, as outlined in ch. 2.4.4, that allows for a non-linear coupling to other collective modes. Solving the equations of motion numerically with the experimental excitation scheme for various droplet atom numbers yields the spectra shown in fig. (5.2c). Starting with the lowest amplitude $\theta_{mod} = 2\,\text{deg}$ (yellow), we obtain a single peak recovering the linear scissors mode frequency according to eq. (5.7) (dashed) with a width given by the Fourier limit Δf. With larger excitation amplitude, this peak shifts towards smaller frequency developing additional peaks at larger frequencies. For $\theta_{mod} = 12\,\text{deg}$ (blue) we find two comparable peaks with a splitting of $\sim 100\,\text{Hz}$ and additional smaller features at higher frequency. Comparing to the presented experimental spectra, we find very good agreement for both the shape and peak position. Extending our measurements to the range of accessible atom numbers N yields the spectrum in fig. (5.3) for the largest modulation amplitude. With increasing atom number the two peaks merge into a broad feature and the overall frequency increases. Again, this spectrum is well reproduced by the time-dependent theory. For comparison we again show the scissors mode of eq. (5.7) in the linear regime (dashed), that deviates from the

acquired spectrum especially for large atom number. According to eq. (5.7) we would naively expect the scaling $\omega_{\mathrm{sc}} \propto \sqrt{N}$ for the scissors mode frequency, but there is an implicit dependence on atom number in the sizes $\sigma_{x,y,z}$.
The presented theoretical spectra are calculated for a scattering length $a_{\mathrm{s}} = 68\,a_0$, where we find good agreement with the experiment. In order to extract a value for a_{s} along with a confidence bound, we quantify the deviation of experiment and theory by defining an error function $E = \sum_k \left[(\sigma_x\sigma_y)_{k,\mathrm{exp}} - (\sigma_x\sigma_y)_{k,\mathrm{theo}}\right]^2$ by summing over the difference in droplet sizes for all modulation frequencies k. In order to take systematic deviations like the finite imaging resolution into account, the droplet sizes $(\sigma_x\sigma_y)$ are rescaled by their respective minimum and maximum values prior to subtraction. The derived error is sensitive to the value of the scattering length and we define the confidence interval where the error function takes double the value of the minimum. This way, we obtain a value $a_{\mathrm{s}} = 68(5)\,a_0$ for the scattering length.
We also note that the magnetic field amplitude is chosen far from Feshbach resonances [182], such that the scattering length corresponds to the background value, $a_{\mathrm{bg}} = a_{\mathrm{s}}$, and there is no variation of the scattering length when modulating the magnetic field in the presented way. In the experiment, we additionally confirmed, that a modulation of the magnetic field amplitude with fixed angle yields no visible excitation in the experiment.
As mentioned before, measurements of the scissors mode were used to provide evidence for superfluidity due to a modified moment of inertia. For the quantum droplet the large aspect ratio leads to a well-defined scissors mode, but at the same time a moment of inertia close to the one of a classical rigid body, although being superfluid, such that no clear distinction is possible. Yet, we presented interference fringes of quantum droplets in [2] and the previous chapter, confirming superfluidity of quantum droplets.

5.3. Coupling to other modes

The non-linear coupling to other modes gives rise to the complex spectrum for the scissors mode measurements with large excitation angles. While it complicates the theoretical description, we can also exploit this effect and excite other modes by modulation of the magnetic field angle.
Here, we rapidly rotate the magnetic field by 90 deg in the xy plane, as sketched in fig. (5.4a), which excites the lowest-lying collective mode. Limited by the inductance of the coils surrounding the glass cell, the minimum time to rotate the magnetic field is 3 ms with a constant magnitude of $B_0 = 800\,\mathrm{mG}$. During this rotation, the droplet orientation follows the magnetic field axis almost instantaneously. Limited by the finite resolution of

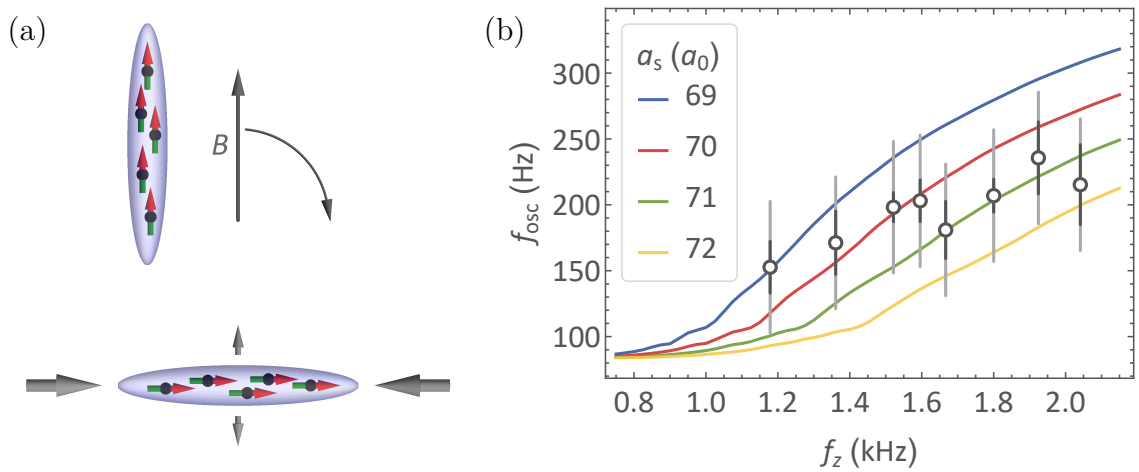

Figure 5.4.: **Excitation of a collective oscillation by a rotation quench.** (a) Schematic of the experiment. We rotate the magnetic field angle by 90 deg within 3 ms. This time is slow enough for the droplet to follow and fast enough to excite the lower quadrupole mode. (b) The oscillation frequency f_{osc} of the axial droplet size for varying lightsheet confinement f_z. The uncertainty is determined by the fit (black) and finite observation time (gray). Lines correspond to the time-dependent variational ansatz for different scattering lengths a_{s}.

the imaging system, which leads to a large uncertainty on the droplet orientation, we do not observe an oscillation of the latter after the magnetic field rotation. Instead, we find a strongly damped oscillation of the droplet's size along the long axis for up to 20 ms. It corresponds to the excitation of the lowest-lying collective mode we presented in ch. 2.4.4, which was also observed in [56].

In fig. (5.4b) we plot the corresponding oscillation frequencies f_{osc} for various values of the transverse confinement f_z, which is adjusted by the lightsheet, and an atom number of 690(150) in the droplet. While the errors on the confinement are negligible, the black error bar shows the squared sum of the standard error and the decay time extracted from a fit to the experimental data. The larger error (gray) corresponds to a 100 Hz bound due to the short observation time.

For the time-dependent theory (colored lines), we take the measured magnetic field angle $\theta(t)$ into account and find qualitatively the same behavior as in the experiment. The extracted frequencies along the long axis also increase with the confinement, yet we find a slightly different slope. A fit to the experimental data yields the best agreement for a scattering length $a_{\mathrm{s}} = 70.5(6.0)\, a_0$. With a similar analysis as in the previous section, we find a frequency uncertainty of $2\, a_0$ and an uncertainty of $5\, a_0$ due to the systematic error of the atom number, resulting in the squared sum of $6\, a_0$.

Both measurements of collective excitations presented in this chapter yield compatible

values for the background scattering length $a_{\mathrm{bg}} = a_{\mathrm{s}}$, since it was measured at a magnetic field magnitude isolated from Feshbach resonances. Combining the two measurements we finally obtain

$$a_{\mathrm{bg}} = 69(4)\, a_0 \tag{5.9}$$

as the error-weighted mean value for ^{164}Dy [183]. Figure (2.11) shows a sizeable difference between the collective modes frequencies in the droplet phase acquired with the Gaussian ansatz compared to the simulations. These stem from the difference in density distribution and thus peak density for the large atom number of $N = 10^4$, cf. fig. (2.12). In contrast, for the atom numbers in the experiment, the density profile is well described by a Gaussian for $N \leq 10^3$ atoms. Putting an upper bound, we compared the frequencies acquired by simulations and the variational ansatz in the linear regime for $N = 10^3$ atoms. In order to match the simulation, we need to shift the scattering length of the variational method by $-1.2\, a_0$ for the lower quadrupole and $+0.1\, a_0$ for the scissors mode frequencies. The systematic error of using the variational method is thus negligible for the range of atom numbers presented in the experiment.
In comparison to other experiments, the value of the scattering length is compatible with $70\, a_0$, which we used for the simulation in fig. (4.3c) yielding good agreement. The measurement of the critical atom number for self-bound droplets points towards a lower value of $62.5(2.4)\, a_0$ [3, 143]. In contrast, measurements with thermal gases yield an error-weighted mean of $92(7)\, a_0$ [11, 184, 185].
In conclusion, we hereby presented a novel tool to excite collective modes by modulation of the magnetic field angle and the first measurement of the scissors mode for a dipolar quantum droplet. The coupling with other fundamental modes of the droplet allows to excite these in the non-linear regime, which we exploit to measure the frequency of the low-lying quadrupole mode. Both measurements yield qualitative agreement with the eGPE and we use the background scattering length a_{bg} as a fit parameter, that yields good agreement for both measurements, but deviates from previous measurements. We discuss this discrepancy in more detail in the following chapter.

Chapter 6

Self-bound droplets

In this chapter, we give additional insight to the experimental observation of self-bound droplets in [3]. While the experimental details have been thoroughly described in a previous thesis [143], we focus on the theoretical side here. We point out, that this observation was only made possible by our own numerical simulations, that were triggered by the discussion of the self-bound state in [55].

In the first section, we explain the nature of the transition from the liquid to the gas phase, which is driven by atom number losses in the experiment. By means of the simulations we thereby gain additional insight in the process. In the subsequent section we analyze the critical atom number for the stability of a quantum droplet we measured in the experiment, which deviates from the prediction of the eGPE. We benchmark this deviation with two theoretical approaches, that include additional finite-temperature effects.

The self-bound object opens new possibilities, but at the same time also imposes new restrictions on the experiment. Thermometry, for example, is not possible with the standard experimental tools. That is why we theoretically exploit the feasibility to immerse a fermionic impurity in the bosonic quantum droplet. These studies were also published in [9], and could be used to measure the temperature of the droplet.

The chapter ends with the discovery of another class of quantum droplet solutions, which emerge for negative dipolar interaction. Due to the anisotropy of the latter, these *pancakelets* are very flat two-dimensional objects.

6.1. Liquid to Gas transition

The most striking property of the liquid-like state, the saturation of the peak density was already shown in fig. (2.12). Here, we reconstruct the behavior of a quantum droplet in the

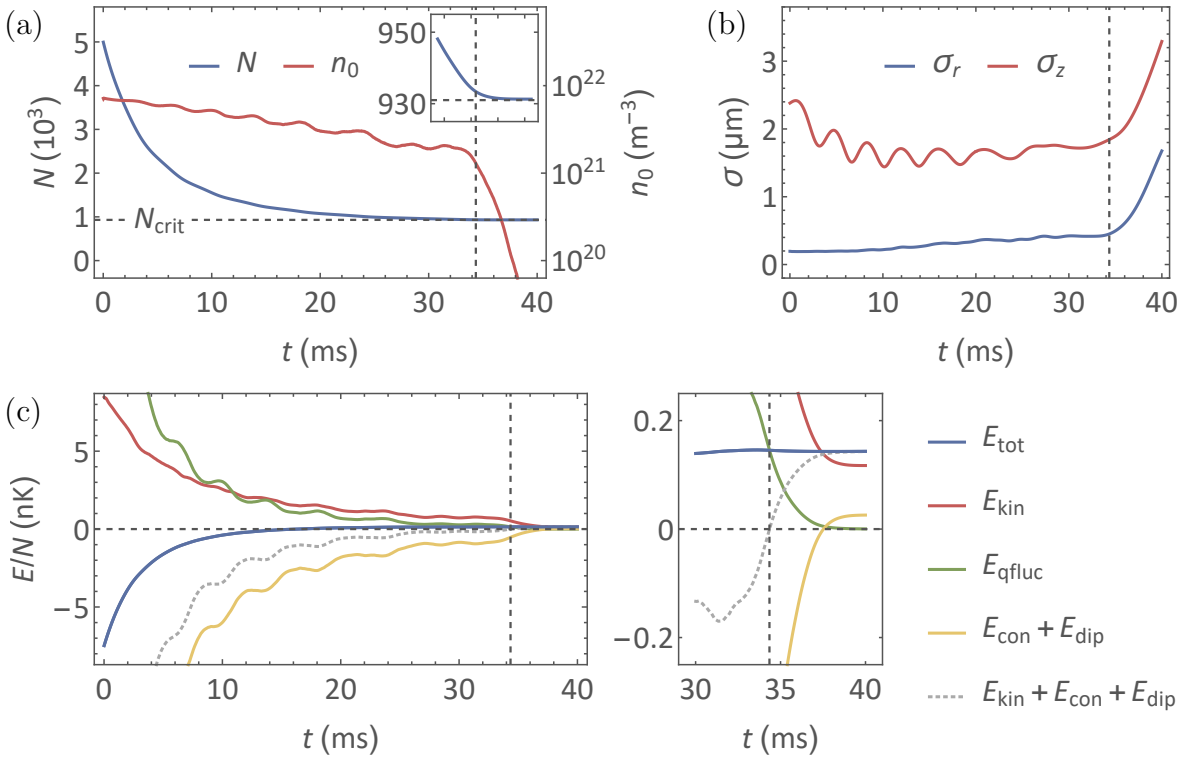

Figure 6.1.: **Self-bound droplet with losses over time.** Simulation of the time-evolution starting with $N = 5000$ atoms in free space. (a) Atom number N (blue) and peak density n_0 (red) over time t. The atom number in the droplet decays almost exponentially until it reaches the critical atom number $N_{\mathrm{crit}} = 931$ (dashed). Since the peak density drops rapidly and suppresses the losses, N is constant afterwards. (b) Radial and axial sizes σ_r (blue) and σ_z (red) with the latter showing the lowest-lying mode of the droplet. (c) Energy contributions over time with total energy E_{tot} (blue) consisting of quantum pressure E_{kin} (red), quantum fluctuations E_{qfluc} (green) and the two-body contributions $E_{\mathrm{con}} + E_{\mathrm{dip}}$ (yellow). The transition from the liquid to the gas phase is determined where $E_{\mathrm{kin}} + E_{\mathrm{con}} + E_{\mathrm{dip}}$ (gray dashed) becomes positive.

experiment [3] by studying its time evolution in simulations. For this purpose we compute the ground state for $N = 5000$ atoms of ^{164}Dy with a scattering length $a_{\mathrm{s}} = 70\,a_0$ and $a_{\mathrm{dd}} = 131\,a_0$ without any trapping potential and subsequently study its evolution with finite three-body losses $L_3 = 1.25 \times 10^{-41}\,\mathrm{m}^6/\mathrm{s}$, see appendix B.

As shown in fig. (6.1a), the decay of the atom number N (blue) is almost exponential up to a point $t_{\mathrm{crit}} \approx 34\,\mathrm{ms}$ (vert. dashed line), where the critical atom number $N_{\mathrm{crit}} = 931$ is reached and the decay stops (inset). While the peak density n_0 (red) only slowly decreased for larger atom number, at this point it drops rapidly, since both the radial and axial sizes σ_r and σ_z increase, see fig. (6.1b). Driven by the decay, we find an oscillation of the axial

size σ_z (red) of the droplet. This corresponds to the lowest-lying quadrupole mode we discussed in ch. 2.4.4, which becomes slower for lower atom number. For a system with losses, this is an important benchmark to determine whether a system is self-bound or actually expanding at very low velocity. If the system can carry out one oscillation of the lowest-lying mode within its lifetime, we call it self-bound.
To understand the underlying process driving the transition to the gas phase, we further study the energy contributions in fig. (6.1c). Initially, the total energy E_{tot} is negative and becomes positive around 17 ms, where the self-bound droplet is still stable [54]. Since the transition occurs much later, we are looking for repulsive terms, that could overcome the combined two-body interaction $E_{\mathrm{con}} + E_{\mathrm{dip}}$ (yellow), which is attractive for the quantum droplet. Since there is a different scaling with density, as can be seen in the eGPE of eq. (2.21), the contribution E_{qfluc} due to quantum fluctuations (green) decays faster than E_{kin} governing the quantum pressure (red), which becomes the leading repulsive term for atom numbers close to N_{crit}. At the point where the density drops, the sum $E_{\mathrm{kin}} + E_{\mathrm{con}} + E_{\mathrm{dip}}$ (dashed gray) turns positive, since the single-particle quantum pressure of the atoms overcomes the residual attractive two-body interactions. Thus, the droplet solution vanishes and the atoms expand in the gas phase. Since the density drops quickly within this "evaporation" three-body losses are suppressed and the atom number stays almost constant afterwards. Therefore, this is where we define the critical atom number N_{crit}, which yields 931 in this example. We note that this approach matches the result $N_{\mathrm{crit}} = 932(12)$, that we usually quote when testing for a stable solution in imaginary time evolution[1]. More importantly, this behavior verifies our experimental measurement of the atom number. There, we took the images at variable times after the droplets evaporated, where the atom number is almost constant [3].

6.2. Critical atom number revisited

The critical atom number for the existence of a self-bound droplet was measured in [3], where we used the strength of the contact interaction, given by the background scattering length a_{bg}, as a fit parameter to match these measurements with the theory of the eGPE. Within this analysis a value $a_{\mathrm{bg}} = 62.5(2.5)\, a_0$ was found [143], which is clearly lower than the measurements of the droplet's collective excitations in ch. 5 yielding $69(4)\, a_0$.
Our experiments are carried out at finite temperatures of a few tens of nanokelvins, which cannot be reproduced by the zero temperature theory of the eGPE. However, thermal fluctuations give rise to a shift of the chemical potential [186, 187], much like the

[1] The error here corresponds to the step in atom number we probe with the simulations.

quantum fluctuations we introduced in ch. 2.2.2. In order to get a first estimate of the effect, we extend the variational ansatz in eq. (2.38) for thermal fluctuations [188], which reads

$$E_{\mathrm{thermal}} = \frac{2^{11/2} m \sqrt{a_{\mathrm{s}}}}{3\hbar^2 \pi^{3/4}} \left(k_{\mathrm{B}} T\right)^2 \mathcal{S}(\varepsilon_{\mathrm{dd}}) \sqrt{N \sigma_r^2 \sigma_z} \tag{6.1}$$

with a function $\mathcal{S}(\varepsilon_{\mathrm{dd}}) = -0.01029\,\varepsilon_{\mathrm{dd}}^4 + 0.02963\,\varepsilon_{\mathrm{dd}}^3 - 0.05422\,\varepsilon_{\mathrm{dd}}^2 + 0.009302\,\varepsilon_{\mathrm{dd}} + 0.1698$. The latter is valid for $\varepsilon_{\mathrm{dd}} \in [0, 2]$ and suppresses thermal effects by a factor ~ 3 for $\varepsilon_{\mathrm{dd}} = 2$ compared to zero dipolar interaction. A similar term derived in ref. [186] follows the same scaling $E_{\mathrm{thermal}} \propto T^2 \sqrt{N a_s}$. In fig. (6.2a), we show the effect on the critical atom number for temperatures of $T = 50\,\mathrm{nK}$ and $100\,\mathrm{nK}$ (red) compared to the reference for zero temperature (black)[2]. In our range of interest $a_{\mathrm{s}} = 60$ to $75\,a_0$, this effect is negligible but becomes important for higher scattering length.

However, there is an additional finite-temperature effect for the scattering properties of dysprosium atoms. Calculations of the scattering amplitude beyond the usual Born approximation give rise to a temperature-dependent enhancement of the DDI [83, 84]. There, the dipolar length a_{dd} increases by $+2\,\%$ ($+10\,\%$) for $T = 10\,\mathrm{nK}$ ($100\,\mathrm{nK}$) compared to the result obtained within the Born approximation. A larger dipolar interaction leads to a lower critical atom number (blue), which is a sizeable effect over the full range of scattering length. In fig. (6.2b), we therefore compare our experimental data set shifted for both background values of the scattering length (gray and green) to the critical atom number obtained with numerical simulations. For the background value of $a_{\mathrm{bg}} = 69(4)\,a_0$ we find good agreement with the $+10\,\%$ enhancement, pointing towards a systematic enhancement of the DDI.

Obviously, such a systematic shift also influences the measurement of the collective modes in ch. 5. Including it in the calculations shown in ch. 2.4.4, we actually find a background value, that is $4\,a_0$ higher compared to the evaluation based on the Born approximation yielding $a_{\mathrm{bg}} = 69(4)\,a_0$. This would in turn lead to a larger deviation from the measurement of the critical atom number for the self-bound droplet supporting our argument of a systematic enhancement of the DDI.

For thermal gases there are three measurements for the background scattering length in ^{164}Dy. These resulted in $a_{\mathrm{bg}} = 92(8)\,a_0$ by cross-dimensional relaxation [184], $91(16)\,a_0$ by molecular association close to a Feshbach resonance [11], and $96(22)\,a_0$ by anisotropic dipolar expansion [185]. The error-weighted mean of these is $a_{\mathrm{bg}} = 92(7)\,a_0$. In these experiments, the value of the total elastic cross section consisting of contact and dipolar

[2] For simplicity, we use the variational ansatz and calculate the atom number, where the total energy is zero. The critical atom number for the existence of the bound state, which we usually quote, is slightly lower.

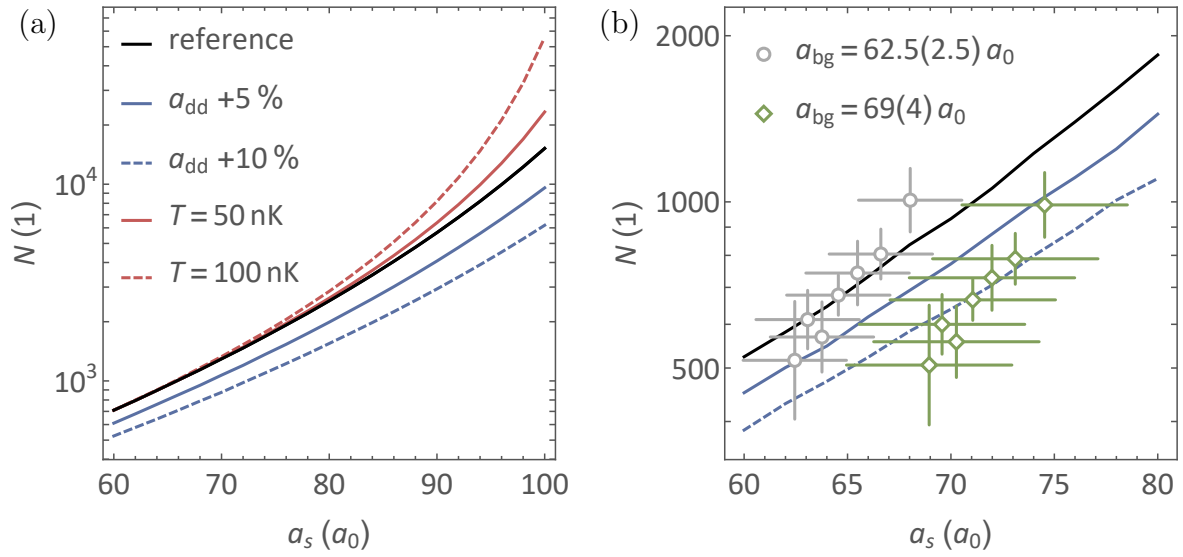

Figure 6.2.: **Critical atom number of a self-bound droplet.** (a) Variational ansatz marking the atom number N yielding zero energy of the droplet for thermal fluctuations (red) at temperatures $T = 50$ and 100 nK in comparison to an enhancement of the dipolar interaction (blue) of $a_{dd}/a_{dd,ref} = 1.05$ and 1.10 for similar temperatures. The reference (black) is the zero temperature theory of the eGPE for $a_{dd,ref} = 131\, a_0$. (b) Comparison with the experimental data for ^{164}Dy [3], where the background scattering length $a_{bg} = 62.5(2.5)\, a_0$ was used as a fit parameter (gray points) to match the eGPE theory (black). Measurements of collective excitations in ch. 5 yield a higher value $a_{bg} = 69(4)\, a_0$ shifting the data (green), which are slightly offset in N for better readability. Theory lines are calculated with numerical simulations. See text for further parameters.

contributions was measured and in a second step the value of $a_{bg} = 92\, a_0$ deduced assuming a fixed $a_{dd} = 131\, a_0$. An enhancement of the DDI would therefore cause a weaker contact interaction for the same cross section. To estimate this effect, we consider the low-temperature dependence of the total cross section in eq. (2.9) and fix the scattering length to our measured value of $a_{bg} = 69\, a_0$, which yields a dipolar length $a_{dd} = 188\, a_0$ recovering the same cross section as the values above. Extrapolating the dipolar enhancement in [84], this value corresponds to a temperature of $\sim 1\,\mu$K, which is typical for such thermal experiments.

Based on this simple estimate, we therefore argue, that the discrepancy in measured scattering length — both in the ultracold and thermal regimes — is caused by the enhancement of the dipolar interaction for finite temperature. Obviously, there are further theoretical studies on the scattering properties of dysprosium atoms for higher temperatures needed to finally conclude this topic.

6.3. Fermionic impurity in a dipolar quantum droplet

In order to examine the effect presented in the previous section, we need to measure the temperature of the droplet. Unfortunately, the standard tool for thermometry is rendered useless for self-bound objects, since it relies on the expansion of the atom distribution after being released from the trap in a time-of-flight experiment. For droplets of liquid helium the immersion of impurities permitted remarkable insights in their properties [189]. They are even used as spectroscopic environments cooling single molecules and clusters to cryogenic temperatures. Inspired by this development, we study the immersion of a fermionic dipolar impurity in a bosonic quantum droplet. The following considerations have been published in [9] with greater detail.

Accordingly, we are interested in the study of a Bose-Fermi mixture with dominant DDI. In its most general form within second quantization, the full Hamiltonian $\hat{H} = \hat{H}_\mathrm{f} + \hat{H}_\mathrm{b} + \hat{H}_\mathrm{bf}$ of the system consists of the intraspecies contributions

$$\hat{H}_\mathrm{f} = \frac{\hbar^2}{2m_\mathrm{f}} \int \mathrm{d}\boldsymbol{r}\, \nabla\hat{\psi}_\mathrm{f}^\dagger \cdot \nabla\hat{\psi}_\mathrm{f} \;+\; \frac{1}{2}\int \mathrm{d}\boldsymbol{r}\, \mathrm{d}\boldsymbol{r'}\, \hat{\psi}_\mathrm{f}^\dagger(\boldsymbol{r'})\hat{\psi}_\mathrm{f}^\dagger(\boldsymbol{r})\, U_\mathrm{ff}(\boldsymbol{r}-\boldsymbol{r'})\, \hat{\psi}_\mathrm{f}(\boldsymbol{r})\hat{\psi}_\mathrm{f}(\boldsymbol{r'}) \tag{6.2}$$

for fermions and similarly for bosons, and the interspecies interaction

$$\hat{H}_\mathrm{bf} = \frac{1}{2}\int \mathrm{d}\boldsymbol{r}\, \mathrm{d}\boldsymbol{r'}\, \hat{\psi}_\mathrm{f}^\dagger(\boldsymbol{r'})\hat{\psi}_\mathrm{b}^\dagger(\boldsymbol{r})\, U_\mathrm{bf}(\boldsymbol{r}-\boldsymbol{r'})\, \hat{\psi}_\mathrm{b}(\boldsymbol{r})\hat{\psi}_\mathrm{f}(\boldsymbol{r'})\,. \tag{6.3}$$

As shown in ch. 2, the predominant interactions for ultracold dipolar atoms are the contact interaction of eq. (2.5) and the DDI of eq. (2.7). The cross section of the former vanishes for fermions in identical spin states due to the Pauli principle.

We are interested in the immersion of few fermions N_f in a droplet with many bosons $N_\mathrm{b} \gg N_\mathrm{f}$. In this limit, we neglect any back-action of fermions on the bosonic droplet state. Scaling with atom number, the interspecies interaction is thus much larger than the fermionic intraspecies DDI. Furthermore, the bosons are subject to quantum depletion [190], which is small even for quantum droplets that are stabilized by quantum fluctuations [53, 55]. This way, we neglect any interaction of depleted bosons with fermions and the intraspecies DDI of fermions. We estimate the order of magnitude of these effects later.

With this simplification the bosonic quantum droplet is not modified by the fermions, and we can describe it with our usual tool, the eGPE, to obtain the bosonic density distribution $n_\mathrm{b}(\boldsymbol{r})$ and ground state energy E_b. For the interspecies interaction $\hat{H}_\mathrm{bf}$ we follow the mean-field approach and thus replace the bosonic operator $\hat{\psi}_\mathrm{b}(\boldsymbol{r})$ by the wavefunction

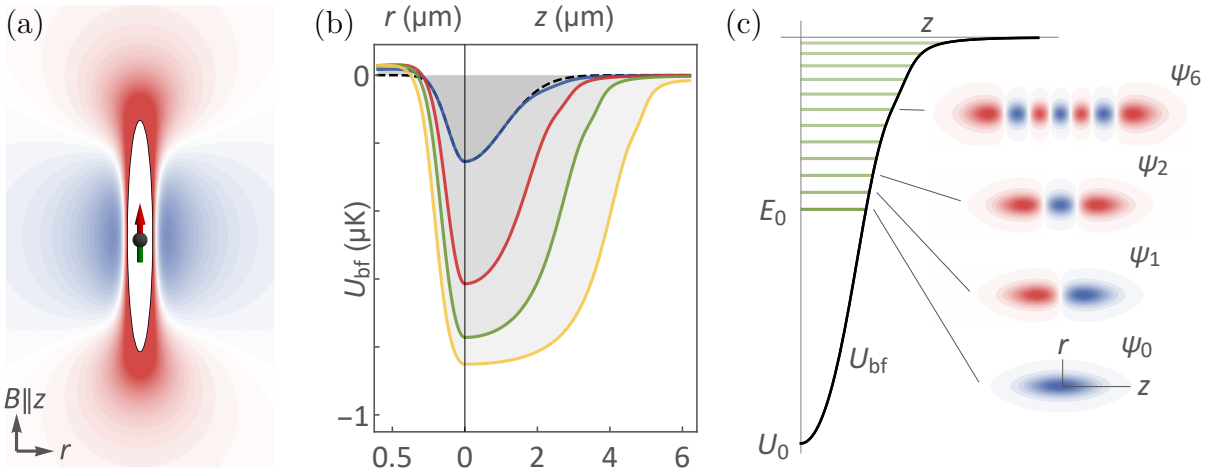

Figure 6.3.: **A fermionic impurity in a quantum droplet.** (a) Schematic of a dipolar fermion in a quantum droplet (white ellipse). The long-range interaction potential is attractive (red) axially and repulsive radially (blue). (b) Calculated mean-field trapping potentials $U_{\mathrm{bf}}(r,z)$ according to eq. (6.5) for a interspecies scattering length $a_{\mathrm{bf}} = 70\,a_0$, a_0 being the Bohr radius, and different atom numbers $N_{\mathrm{qd}} = \{1,2,4,8\}\times 10^3$ (blue to yellow) of the droplet. The dipolar interaction leads to deviations from a Gaussian density profile (dashed). (c) Bound states of an impurity for $N_{\mathrm{qd}} = 1500$ and $a_{\mathrm{bf}} = 70\,a_0$. The axial potential $U_{\mathrm{bf}}(r=0,z)$ is plotted (black) along with the bound state energy E_{s} (green). Insets show example wavefunctions $\psi_s(r,z)$, which resemble harmonic oscillator eigenstates. Having ground state character radially, these are effectively one-dimensional systems.

$\psi_{\mathrm{b}} = \sqrt{n_{\mathrm{b}}(\boldsymbol{r})}$, which yields the Hamiltonian

$$\hat{H} = E_{\mathrm{b}} + \int \mathrm{d}\boldsymbol{r}\left[\frac{\hbar^2}{2m_{\mathrm{f}}}\nabla\hat{\psi}_{\mathrm{f}}^{\dagger}\cdot\nabla\hat{\psi}_{\mathrm{f}} + \frac{1}{2}\hat{\psi}_{\mathrm{f}}^{\dagger}\hat{\psi}_{\mathrm{f}}\,U_{\mathrm{bf}}(\boldsymbol{r})\right] \tag{6.4}$$

depending on the Bose-Fermi interaction potential. The latter reads

$$U_{\mathrm{bf}}(\boldsymbol{r}) = g_{\mathrm{bf}}\,n_{\mathrm{b}}(\boldsymbol{r}) + \int \mathrm{d}\boldsymbol{r}'\,V_{\mathrm{dd}}(\boldsymbol{r}-\boldsymbol{r}')\,n_{\mathrm{b}}(\boldsymbol{r}') \tag{6.5}$$

and relies on the interspecies scattering length a_{bf} defining[3] $g_{\mathrm{bf}} = 4\pi\hbar^2 a_{\mathrm{bf}}/m_{\mathrm{f}}$. This way, the problem in eq. (6.4) reduces to the stationary Schrödinger equation with a Hamiltonian

$$H = -\frac{\hbar^2\Delta^2}{2m_{\mathrm{f}}} + U_{\mathrm{bf}}(\boldsymbol{r}) \tag{6.6}$$

describing a single particle in a fixed external potential $U_{\mathrm{bf}}(\boldsymbol{r})$.

[3] We assume equal masses $m_{\mathrm{f}} \approx m_{\mathrm{b}}$ and therefore use m_{f} instead of the reduced mass.

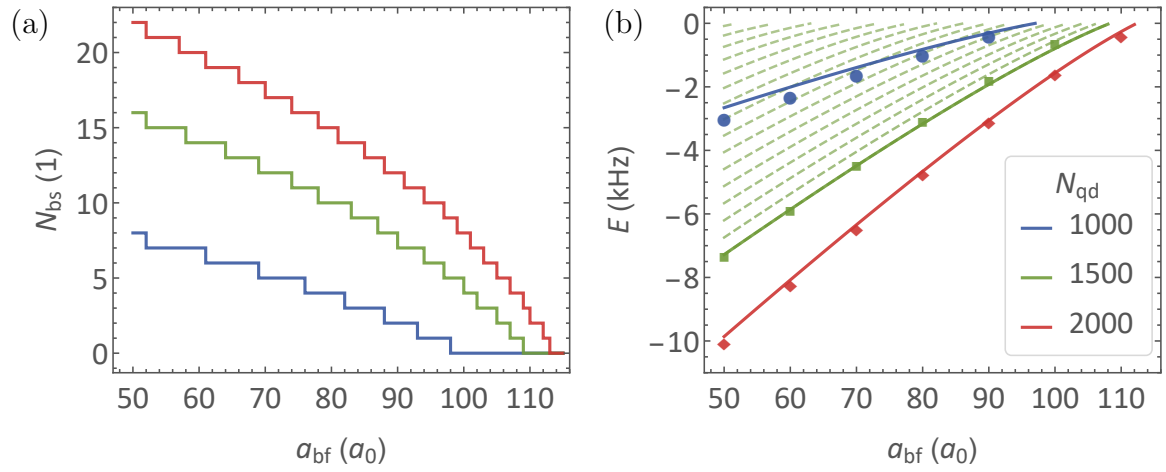

Figure 6.4.: **Bound state properties.** (a) Number of bound states N_{bs} over Bose-Fermi scattering length a_{bf} for various droplet atom numbers N_{qd}. (b) Ground state energy E_0 (solid lines) and corresponding calculations with the eGPE (dots). Additionally, excited states $E_s > E_0$ are shown for $N_{qd} = 1500$ (dashed).

Since we are particularly interested in dysprosium, we now consider a single fermionic impurity of ^{163}Dy immersed in a droplet of N_{qd} bosonic ^{164}Dy atoms with an intraspecies scattering length $a_{bb} = 70\,a_0$ in accordance with the previous consideration. Owing to the collisional richness of lanthanide atoms [10, 182], we expect to find a suitable Feshbach resonance to realize an intraspecies contact interaction with $a_{bf} = 70\,a_0$.

With the eGPE simulations, we then extract the droplet density profile $n_b(\boldsymbol{r})$ and calculate the interaction potential $U_{bf}(r, z) = U_{bf}(\boldsymbol{r})$ of eq. (6.5). As shown in fig. (6.3a), it resembles the droplet (white ellipse) with additional attractive wings axially (red) and repulsive ones radially (blue) due to the long-range character of the interaction. Figure (6.3b) shows radial and axial cuts for various atoms number revealing a strong dependence of the potential depth $U_0 = U_{bf}(0)$ on the atom number N_{qd}. In a next step, we calculate the spectrum of eq. (6.6), which is thoroughly described in [9], and find a couple of anharmonically spaced bound states, see fig. (6.3c). Due to the large aspect ratio of the potential, the acquired eigenstates ψ_s are qualitatively similar to the solution of a cylindrical harmonic oscillator restricted to the $l = 0$ radial ground state. As such, the trapped impurities can be used as testbeds for one-dimensional physics on the few atom level.

In fig. (6.4), we examine the properties of these bound states in the range $N_{qd} \leq 2000$ atoms and $a_{bf} = 50 - 120\,a_0$, where the bound states are well in the one-dimensional regime. We note, that the number of bound states N_{bs} is an upper limit for the number of trapped fermions N_f. Our assumption $N_f \ll N_{qd}$ for a negligible influence on the

bosonic ground state is thus intrinsically satisfied. Our approach is verified by independent numerical calculations of the ground state (dots), see fig. (6.4b). The anharmonicity of the trapping potential U_{bf} leads to a rich level scheme with a typical spacing of $\Delta E = E_{s+1} - E_s \approx h \times 500\,\mathrm{Hz}$, that decreases to $\approx h \times 200\,\mathrm{Hz}$ towards the threshold. Experimentally, the level spectrum could be probed by driving transitions between bound states through harmonic modulation of a_{bf} at the frequency $\Delta E/h$.

In addition, we estimate the magnitude of the DDI between fermions, which we neglected so far. Therefore, we compute the Hartree energy

$$E_{s,s'} = \frac{1}{2} \int \mathrm{d}\boldsymbol{r}\, \mathrm{d}\boldsymbol{r'}\, |\psi_s(\boldsymbol{r})|^2\, V_{\mathrm{dd}}(\boldsymbol{r} - \boldsymbol{r'})\, |\psi_{s'}(\boldsymbol{r'})|^2 \tag{6.7}$$

of the states ψ_s and $\psi_{s'}$. Assuming a single fermion in both states yields an energy shift $E_{0,1}$ between ground and first excited state of $\approx 20\,\mathrm{Hz}$, which is small compared to the level spacing ΔE. For other combinations of s and s' we find lower values due to decreasing overlap of the wavefunctions, such that the influence of the intraspecies DDI between fermions is indeed negligible. In the case of several fermions in the droplet full Hartree-Fock calculations would be necessary to calculate the modifications to the orbitals. In order to estimate a second effect, the interaction with depleted bosonic atoms, we calculate the condensate depletion $\Delta n/n \approx 5\,\%$ of the bosonic droplet [62]. For a droplet with $N_{\mathrm{qd}} = 1500$ atoms this corresponds to $N_{\mathrm{depl}} = 75$ depleted atoms, which is substantially higher than the number of bound states. Based on the prior estimate, the associated energy shift is likely on the order of the level spacing. Expanding on this effect, a fermionic impurity might therefore be used to probe the quantum depletion of the droplet, which has not been measured. Yet, a more sophisticated theory is needed to describe and understand this effect properly.

To summarize, we derived the Hamiltonian of few fermions interacting with a large number of bosons. For a low number of fermions, the bosonic state is unaffected and the problem reduces to a Schrödinger equation of a particle in a fixed potential. For the parameters discussed here, we find the possibility to immerse few fermionic impurities in a bosonic dipolar quantum droplet. Consequently, this is the first step towards probing quantum droplets with impurities. Since these thermalize with the bosonic environment, the excitation spectrum should be subject to thermal broadening, which we plan to use in order to measure the temperature of the quantum droplet. With negligible back-action, measurements of the impurity should be possible non-destructively using recently developed single atom detection techniques [191]. The tools to create Bose-Fermi mixtures with highly-magnetic atoms are readily available as well [192].

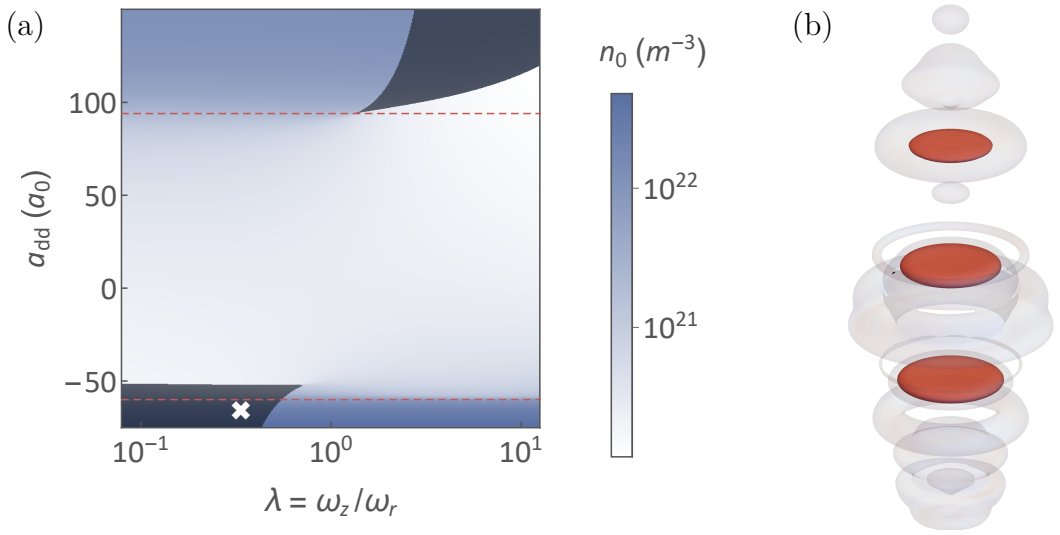

Figure 6.5.: **Pancakelets with inverted dipolar interaction.** (a) Peak density n_0 depending on the dipolar length a_{dd} and trap aspect rato $\lambda = \omega_z/\omega_r$ calculated with the variational ansatz of eq. (2.38). For $a_{\mathrm{dd}} \lesssim -52\,a_0$, we find droplet-like solutions with an inverted aspect ratio, which we call pancakelets. We assume $N = 10^4$ atoms with a scattering length of $a_{\mathrm{s}} = 70\,a_0$ in a harmonic trap with mean frequency $\bar{\omega} = 2\pi \times 70\,\mathrm{Hz}$. We find bistable solutions (dark) areas for both the droplet and pancakelet. Dashed lines mark the border for self-bound solutions, that are stable without a trap. The white cross at $\lambda = 1/3$ marks the situation in (b), where the modulational instability leads to a stack of pancakelets after a quench of the scattering length from $a_{\mathrm{s}} = 140\,a_0$ to $70\,a_0$.

6.4. Inverting the DDI: The Pancakelet

Finally, we point out a peculiar property of the dipolar interaction. Its anisotropy gives rise to another class of dipolar quantum droplets, which we call *pancakelets* and describe in the following.

As shown in fig. (6.5a) with the variational ansatz, we find the well-known droplet solutions for the usual dipolar length $a_{\mathrm{dd}} = 131\,a_0$ of ^{164}Dy. As we explained in ch. 2.4.3, these are characterized by a cloud aspect ratio $\kappa = \sigma_r/\sigma_z \ll 1$ and a peak density $n_0 \gtrsim 10^{21}\,\mathrm{m}^{-3}$. There is a bistable region (dark area) for $\lambda > 1$, where a modulational instability occurs experimentally. For this calculation, we use $N = 10^4$ atoms with a scattering length $a_{\mathrm{s}} = 70\,a_0$ in a harmonic potential with mean frequency $\bar{\omega} = 2\pi \times 70\,\mathrm{Hz}$. In the absence of this trapping potential, there are self-bound solutions for $a_{\mathrm{dd}} > 94\,a_0$ (dashed). Lowering the dipolar interaction we find the usual BEC solution with a lower peak density and an aspect ratio, that follows the trap aspect ratio, but is slightly altered due to magnetostriction.

If we invert the dipolar interaction as proposed in [75] and realized in [76], we consequently find droplet solutions for sufficiently strong interaction of $a_{\mathrm{dd}} < -52\,a_0$. Thus, the sign

of the interaction potential in eq. (2.7) is changed, such that it becomes attractive in a side-by-side configuration, where the interaction is a factor of two stronger. For this reason, the density is an order of magnitude higher compared to the usual droplet solution. More importantly, the aspect ratio $\kappa \gg 1$ is inverted, which is the reason why we named these solutions pancakelets. Here, the bistability occurs for $\lambda < 1$ and we find self-bound solutions for $a_{\mathrm{dd}} < -60\,a_0$. We further confirm this prediction of the variational ansatz with numerical simulations. Similar to the normal droplet, we find a saturating peak density. Such pancakelets have a thickness on the order of a healing length and can therefore be useful in the study of two-dimensional physics. In the bistable region we can create stacks of pancakelets by a quench of the scattering length a_{s} from $140\,a_0$ to $70\,a_0$ inducing a modulational instability, as presented in fig. (6.5b) for $\lambda = 1/3$.
The necessary tuneability of the dipolar interaction can be realized with a rotating magnetic field inducing a time-averaged dipolar interaction with an effective dipolar length in the range $-1/2\,a_{\mathrm{dd}}$ to $+1\,a_{\mathrm{dd}}$ [75]. This scheme has been realized in [76] for expansion measurements and has also been used for in situ measurements in our lab. By tuning of the magnetic field angle, we observed an inversion of the aspect ratio of a stable ^{162}Dy condensate. Due to severe heating, which we attribute to residual field gradients, these experiments are currently limited to lifetimes of $\sim 10\,\mathrm{ms}$. In order to create and probe such pancakelets in the experiment, this heating needs to be reduced.

Chapter 7

Superfluid effects in a dBEC

Superfluidity, as first discovered in liquid helium [12], is a hallmark of quantum physics on the macroscopic scale. The seminal Landau criterion [107] relates the absence of dissipation to the excitation spectrum of the superfluid, as we derived in ch. 2.3.3. With the dipolar interaction we predicted an anisotropic critical velocity for the onset of dissipation. In the context of ultracold atoms, superfluidity has been studied experimentally for trapped contact-interacting BECs [193, 194], a two-dimensional Bose gas [195] and a Fermi gas in the BEC-BCS crossover regime [196, 197].

Based on these pioneering experiments, we present the first transport measurements on a dBEC in the first section, which also have been published in [8]. By moving an attractive laser beam through the condensate we observe an anisotropy in both the critical velocity and the heating rate in the dissipative regime. In particular, we realize a situation, where for a fixed velocity the flow is dissipationless along one direction and subject to dissipation perpendicular to it. We find excellent agreement with dynamical simulations of the eGPE taking into account finite-size effects of the trapped dBEC as well as the characteristics of the moving impurity.

In the second section we numerically explore quantized vortices in rotating superfluids, which are a consequence of their irrotational flow. The spatial extent of such defects in the condensate is given by the healing length, which becomes anisotropic with the dipolar interaction, as we have shown in ch. 2.3.2. This effect leads to the deformation of the vortex core [103] and induces long-range interactions between vortices [104], which would result in the formation of striped vortex patterns [103, 105]. Within numerical simulations, we exploit the possibility to observe these effects in our experiment and point out ways to create the desired states.

7.1. Anisotropic critical velocity

In ch. 2.3.3, we derived the generalized Landau criterion of eq. (2.30) in the context of the dipolar interaction. Since the excitation spectrum $E(\boldsymbol{k})$ of a homogeneous dipolar gas is anisotropic, the critical velocity v_c we derived in eq. (2.32) depends on the angle α of momentum $\boldsymbol{k}$ with respect to the magnetic field axis $\boldsymbol{B}$. The anisotropy of the excitation spectrum has been confirmed experimentally with a chromium dBEC [101]. Based on a eq. (2.32), we found a variation of the critical velocity $v_c(\alpha)$ from 2.0 to 0.3 mm/s, which we want to study experimentally.

As depicted in fig. (7.1a), we therefore focus an attractive laser beam on a trapped dBEC of ^{162}Dy atoms. This "stirring beam" with a waist of $w_0 \approx 1.5\,\mu$m and a potential depth of roughly half the chemical potential is then moved transversally by an electro-optical deflector system, which we described in ch. 3.2. In order to measure the critical velocity, we move the beam at constant velocity $v = 4\,r_\mathrm{s} f_\mathrm{s}$. To get a sizeable heating effect, we repeat this process and thus vary the beam position with a triangular periodic function determined by the amplitude r_s with respect to the cloud center and the frequency f_s. This method introduces small heating for $v < v_\mathrm{c}$, due to the emission of sound waves at the turning points [198]. The determination of the velocity thus depends on the amplitude r_s, which we need to calibrate for both stirring directions. In a first step, we therefore determine the magnification $M_x = M_y = 44.2(1)$ of the imaging system by moving the objective mounted on a piezo-stage transversally. We confirm with a raytracing software that this method is not affected by imaging aberrations in the field of view. For the second step, we load all atoms in the stirring beam at large beam power and move it over the full range $d = 2\,r_\mathrm{max}$ of the deflector system along one direction taking several images. By a linear fit to the position data we then extract the maximum amplitudes $r_{\mathrm{max},x} = 2.9(2)\,\mu$m and $r_{\mathrm{max},y} = 3.4(2)\,\mu$m for both directions. We attribute this difference to a minor misalignment of the stirring beam focus with respect to the cloud. When comparing measured and theoretical Thomas-Fermi radii, we find an additional 6% difference in the two directions, which we attribute to imaging aberrations. Since these can influence the calibration of the velocity as well, we quadratically add this error to the one in r_max, which then yields the error of the displayed velocity v.

For the measurements we prepare a dBEC in an almost cylindrical trap $f_x = 52(1)\,\mathrm{Hz} \approx f_y = 49(1)\,\mathrm{Hz}$, $f_z = 168(1)\,\mathrm{Hz}$ at a condensed fraction of 0.7 with $1 \cdot 10^4$ to $2 \cdot 10^4$ atoms in total. Then – while moving the beam continuously – the power of the stirring beam is ramped up within 25 ms, kept constant for a time $t_\mathrm{stir} = 1\,\mathrm{s}$, and ramped down within 25 ms followed by an additional 200 ms for thermalization of the sample. In order to avoid thermal wings and to probe the high-density region of the cloud we choose a stirrer

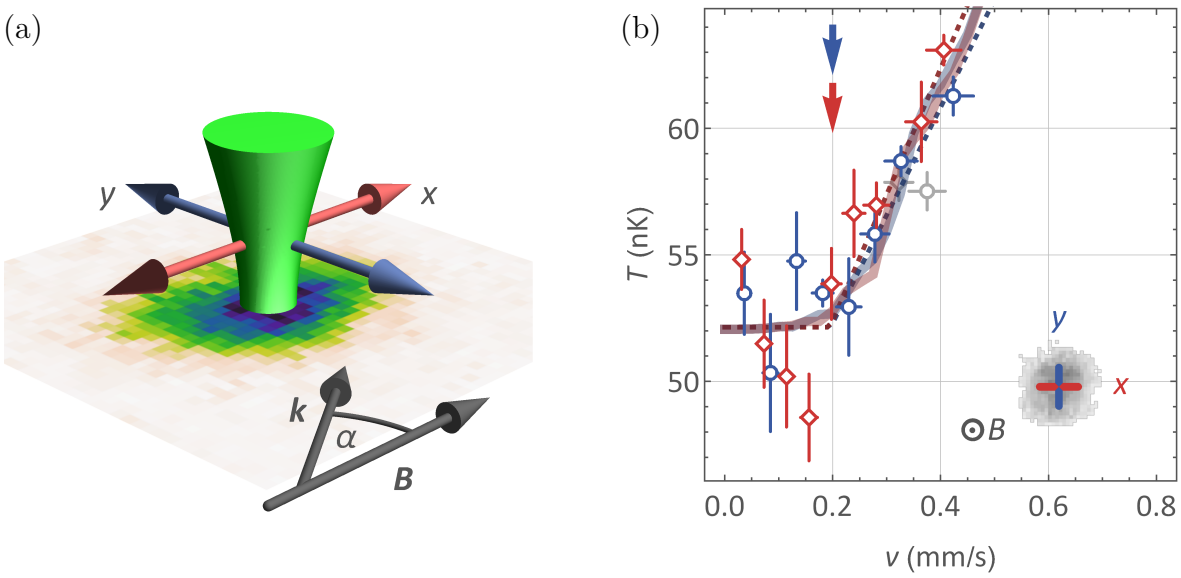

Figure 7.1.: **Probing the anisotropic critical velocity.** (a) Schematic of the experiment. We drag an attractive laser beam through a dipolar condensate perpendicular ($\alpha = 90\,°$, blue) and parallel ($\alpha = 0\,°$, red) to the magnetic field direction, which should allow to probe the critical velocity along both directions. (b) Reference measurement in the isotropic case $\boldsymbol{B} \parallel \hat{\boldsymbol{z}}$. We plot the temperature of the sample after repeatedly moving the stirring beam along the x- (red squares) or y- (blue circles) axis, as illustrated in the inset with an example in situ image. Critical velocities are extracted by a linear fit (dashed) and marked with arrows. As expected, the response is isotropic with $v_x = 0.20(5)\,\mathrm{mm/s}$ and $v_y = 0.20(7)\,\mathrm{mm/s}$. Data points with stirring frequency matching the trapping frequencies (gray) are excluded from the analysis. Simulations of the eGPE for a single stirring cycle (solid lines) show excellent agreement with the experiment. See text for further parameters.

amplitude $r_\mathrm{s}/R_\mathrm{TF} = 0.15 - 0.35$, well below the Thomas-Fermi radius R_TF of the dBEC. Finally, we image the atoms via phase-contrast imaging at $\Delta = 20\,\Gamma$ detuning as described in ch. 3.2. From these in situ images we extract the condensed fraction N_0/N by fitting the sum of a thermal Gaussian distribution plus a Thomas-Fermi parabola. From eq. (2.4) we extract the temperature T of the sample based on the calculated critical temperature $T_\mathrm{c} = 59 - 77\,\mathrm{nK}$ in our measurements including finite-size effects [126] and interactions [199]. We fit the acquired temperature data with the function

$$T(v) = T_0 + h\,t_\mathrm{stir}\,(v/v_\mathrm{c} - 1)\Theta(v - v_\mathrm{c}) \tag{7.1}$$

defining the critical velocity v_c. In the dissipationless regime for $v < v_\mathrm{c}$ it is constant and increases linearly with a given rate $\dot{T} = h\,(v/v_c - 1)$ above v_c, which is determined by the heating coefficient h. We stress, that our data is no clear proof of superfluidity due

to experimental noise in the dissipationless regime, but it is in excellent agreement with superfluid flow and well-described by this model.

We compare this data to dynamic simulations of the eGPE in order to take the inhomogeneity and finite-size effects of the BEC as well as the finite extent and depth of the stirring beam into account. To properly describe the experiment, we implement a time-dependent attractive "stirrer" Gaussian potential $V_{\mathrm{stir}}(\boldsymbol{r}, t)$ in addition to the static harmonic trap $V_{\mathrm{trap}}(\boldsymbol{r})$. After preparing the dBEC in the ground state, we move this beam with a constant velocity v along the desired direction for a single stirring cycle[1]. We then scale the gain in total energy $\Delta E/N$ of one cycle by the number of oscillations $t_{\mathrm{stir}} f_s$ in the experiment, thus assuming an identical increase in energy induced by the subsequent stirring cycles. The relation between the temperature and energy is non-linear even for the ideal Bose gas [60], and we assume a linear relation for the observed change in temperature of less than 20%. Thus, we map the simulation data to a temperature $T = T_0 + c\, t_{\mathrm{stir}} f_s\, \Delta E/N k_B$ with the Boltzmann constant k_B. The scaling coefficient c is then used as a fit parameter to match the theory with the experiment, which yields $c = 0.022$, 0.0375 and 0.05 for the first, second and third data set, respectively. This parameter also takes into account the relation between energy and temperature, the uncertainty in the potential depth, as well as finite-temperature effects lowering the superfluid fraction [200]. A finite-temperature theory would probably allow to include such effects and further model the introduced coefficient properly. From the simulated temperature, we then extract the critical velocity by the same fit function as used for the experimental data. We stress, that the used rescaling procedure does not influence the critical velocity and note, that preparing the ground state in the harmonic trap only and subsequent adiabatic ramping of the stirring potential's depth leads to similar results with the disadvantage of longer simulation times.

With the evaluation procedure and theory at hand we now turn to the measurements. For the reference measurement shown in fig. (7.1b), we apply a magnetic field $\boldsymbol{B} \parallel \hat{\boldsymbol{z}}$. Moving the laser defect along $\hat{\boldsymbol{x}}$ or $\hat{\boldsymbol{y}}$ is expected to give the same critical velocity, since the problem is isotropic in the xy plane. Indeed, we observe the same threshold in heating of the dBEC for both stirring directions along $\hat{\boldsymbol{x}}$ (red diamonds) and $\hat{\boldsymbol{y}}$ (blue circles). From the fits (dashed lines) we extract matching critical velocities $v_x = 0.20(5)\,\mathrm{mm/s}$ and $v_y = 0.20(7)\,\mathrm{mm/s}$ (marked by arrows) as well as heating coefficients $h_x = 8(5)\,\mathrm{nK/s}$ and $h_y = 9(8)\,\mathrm{nK/s}$. For this measurement the stirring frequency is varied between $f_{\mathrm{s}} = 3$ and $60\,\mathrm{Hz}$. Points at the transversal trap frequencies (gray) are excluded from the analysis, since coupling to the center-of-mass mode might influence the heating. We further find

[1] Thus the position varies from $r = 0$ to r_{s}, then to $-r_{\mathrm{s}}$, and finally back to 0 within the time $t = 1/f_{\mathrm{s}}$.

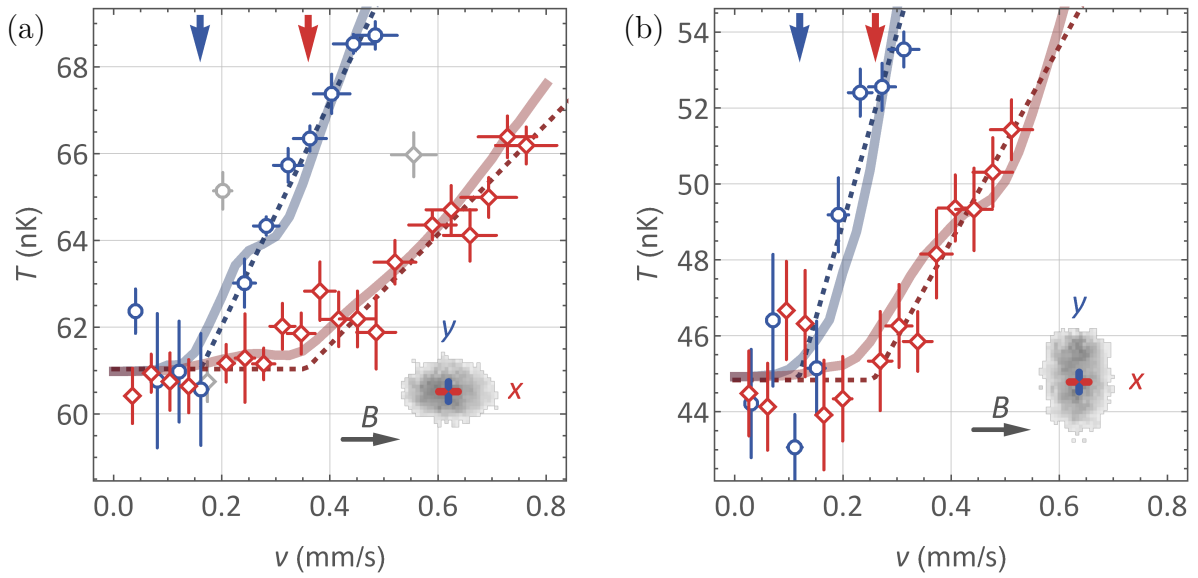

Figure 7.2.: **Temperature of the dBEC after stirring** for the anisotropic case with $\boldsymbol{B} \parallel \hat{\boldsymbol{x}}$ in an almost cylindrical trap (a). In (b) the trap is additionally reshaped to invert the cloud aspect ratio. The stirring beam is moved along the x- (red squares) or y- (blue circles) axis, as illustrated in the insets with example in situ images. Critical velocities are extracted by a linear fit (dashed) and marked with arrows. In (a) the response with $v_\perp = 0.16(2)\,\mathrm{mm/s}$ along $\hat{\boldsymbol{y}}$ and $v_\parallel = 0.36(3)\,\mathrm{mm/s}$ is clearly anisotropic. In (b) we extract $v_\perp = 0.12(3)\,\mathrm{mm/s}$ and $v_\parallel = 0.26(4)\,\mathrm{mm/s}$ proving that the observed anisotropy remains even when inverting the anisotropy of the atomic cloud. Data points with stirring frequency matching the trapping frequencies (gray) are excluded from the analysis. Simulations of the eGPE for a single stirring cycle (solid lines) show excellent agreement with the experiment. See text for further parameters.

excellent agreement with the simulation data (solid lines) yielding a fitted critical velocity $v_{x,\mathrm{sim}} = v_{y,\mathrm{sim}} = 0.21(1)\,\mathrm{mm/s}$. This reference measurement serves as a sanity check and verifies both the calibration of the experiment and the simulation procedure.

For the measurement of interest, we turn to the anisotropic case with the magnetic field $\boldsymbol{B} \parallel \hat{\boldsymbol{x}}$ along one of the stirring directions. The cloud is deformed due to magnetostriction with an in-plane aspect ratio aspect ratio $\kappa = R_x/R_y = 1.4$ given by the Thomas-Fermi radii $R_x = 6.0\,\mu\mathrm{m}$ and $R_y = 4.3\,\mu\mathrm{m}$. In this configuration with a predominantly attractive DDI, the peak density of $n_0 = 1.7 \times 10^{20}\,\mathrm{m}^{-3}$ is higher compared to the previous case. In this setting the excitation spectrum becomes anisotropic in the xy plane. Consequently, we directly observe a factor of two difference in the critical velocity, as shown in fig. (7.2a). Fitting the data, we find $v_x = 0.36(3)\,\mathrm{mm/s}$ and $v_y = 0.16(2)\,\mathrm{mm/s}$ with compatible heating coefficients $h_x = 4.5(9)\,\mathrm{nK/s}$ and $h_y = 4.2(9)\,\mathrm{nK/s}$. The difference in heating rates $\dot{T} = h\,(v/v_c - 1)$, determined by the slope in the figure, is thus fully covered by the anisotropy in critical velocity. A comparison to the simulation with $v_{x,\mathrm{sim}} = 0.35(2)\,\mathrm{mm/s}$

and $v_{y,\mathrm{sim}} = 0.16(1)\,\mathrm{mm/s}$ shows excellent agreement. We note, that we use a single fit parameter c for both curves. Therefore the anisotropy in heating rate is accurately reproduced by the simulation. We infer, that both anisotropic effects share a common cause in the anisotropy of the dipolar excitation spectrum.

With the presented measurement, we cannot exclude an induced anisotropy due to the deformation of the cloud. In a third measurement, we therefore adjust the trapping potential to invert the aspect ratio of the cloud $\kappa = R_x/R_y \approx 1.4^{-1}$. The trap frequencies are $f_x = 81(2)$, $f_y = 39(1)$ and $f_z = 140(1)\,\mathrm{Hz}$ with stronger confinement along the magnetic field axis $\boldsymbol{B} \parallel \hat{\boldsymbol{x}}$, which leads to measured sizes $R_x = 4.3\,\mu\mathrm{m}$ and $R_y = 5.8\,\mu\mathrm{m}$ of the condensate. From the data presented in fig. (7.2b) we extract the critical velocities $v_x = 0.26(4)\,\mathrm{mm/s}$ and $v_y = 0.12(3)\,\mathrm{mm/s}$ with compatible heating coefficients $h_x = 7(3)\,\mathrm{nK/s}$ and $h_y = 6(3)\,\mathrm{nK/s}$. Although the cloud aspect ratio was inverted, the anisotropy of transport remains in the same direction. The presented measurements therefore provide conclusive evidence that the latter arises directly from the dipolar interaction.

We can also compare the measured v_c to the value we derived in eq. (2.32) for the homogeneous gas. With the given peak density, we obtain $v_{x,\mathrm{hom}} = 2.6\,\mathrm{mm/s}$ and $v_{y,\mathrm{hom}} = 0.42\,\mathrm{mm/s}$. The measured critical velocity is thereby a factor 0.1 – 0.4 lower. This fraction is in good agreement with the pioneering experiments in [194]. The inhomogeneous density distribution of the gas in the trap obviously lowers the critical velocity both along the beam and transversally [201]. Vortex formation is a dominant effect for repulsive obstacles, but should be supressed in our experiment with an attractive beam [202]. Yet, the macroscopic size of the beam in comparison to the healing length influences the measured critical velocity as well [203]. In order to avoid the effective reduction of the measured critical velocity, one needs to resort to more advanced methods employing an optical lattice [204] or the use of microscopic impurities, which are realized by either stimulated Raman transitions [205] or with atomic mixtures [206].

To conclude, we performed the first transport measurements on a dBEC. We study the superfluid behavior of the gas by measuring the heating caused by moving an attractive laser beam at constant velocity through the condensate. We find an anisotropic critical velocity, which is in excellent agreement with numerical studies taking into account finite-size effects. From this agreement of the zero temperature theory with our data taken at a sizeable thermal fraction, we infer that thermal excitations do not influence the measured critical velocity. For the present experiments with dipolar strength $\varepsilon_{dd} < 1$ and weak confinement along the magnetic field, roton softening of the excitation spectrum is negligible. As discussed in ch. 2.3.4, increasing both quantities could lead to an observable

reduction of the critical velocity, which is an interesting perspective for future experiments.

7.2. Dipolar vortices

Another striking consequence of superfluidity is the formation of vortices, which are topological defects occuring in rotating superfluids. Here, we numerically study how the dipolar interaction influences these defects and whether we can observe them under experimental conditions. There is a myriad of experimental studies for superfluids with isotropic interactions in the context of ultracold atoms, starting with refs. [18, 207]. Later arrays of vortices aligning in triangular patterns have been observed in BECs [102] and in Fermi gases across the BEC-BCS crossover [22]. Much earlier, Abrikosov lattices of vortices carrying magnetic flux quanta had been predicted in superconductors [106] and measured [208, 209]. In this context, vortex chains have been observed for anisotropic superconductors [210].

An experimental study of vortices in an ultracold dipolar superfluid is lacking. Prior attempts to observe vortices in our experiment were not successful, which we attribute to the fast decay for finite temperatures $T > 0.5\,T_\mathrm{c}$ [211] and our limited imaging resolution, see below. In ref. [162], we numerically examined the stirring mechanism based on our electro-optical deflector system and the influence of an anisotropy in the in-plane confinement, both rendering the experimental observation feasible.

Before presenting the numerical simulations, we quickly review rotating superfluids based on refs. [60, ch. 14] and [213]. In a reference frame rotating at a constant angular velocity Ω about the $\hat{\boldsymbol{z}}$ axis, the Hamiltonian H_0 in the laboratory frame becomes

$$\tilde{H} = H_0 - \Omega L_z \tag{7.2}$$

lowering the energy for states with finite angular momentum L_z. Its ensemble-averaged value $\langle L_z \rangle = \Theta\Omega$ is proportional to the moment of inertia Θ, which we already introduced in ch. 5 for the scissors mode measurements. To recap, it takes the irrotational form

$$\Theta = \delta^2 \Theta_\mathrm{rig} \quad \text{with} \quad \delta = \frac{\langle y^2 - x^2 \rangle}{\langle y^2 + x^2 \rangle} \quad \text{and} \quad \Theta_\mathrm{rig} = Nm\langle y^2 + x^2 \rangle \tag{7.3}$$

for a superfluid determined by the deformation δ of the cloud in the xy plane. Therefore the superfluid moment of inertia vanishes for an isotropic distribution, in contrast to the classical rigid-body value Θ_rig having a well-defined value.

In this rotating frame, we calculate the ground state by imaginary time evolution with

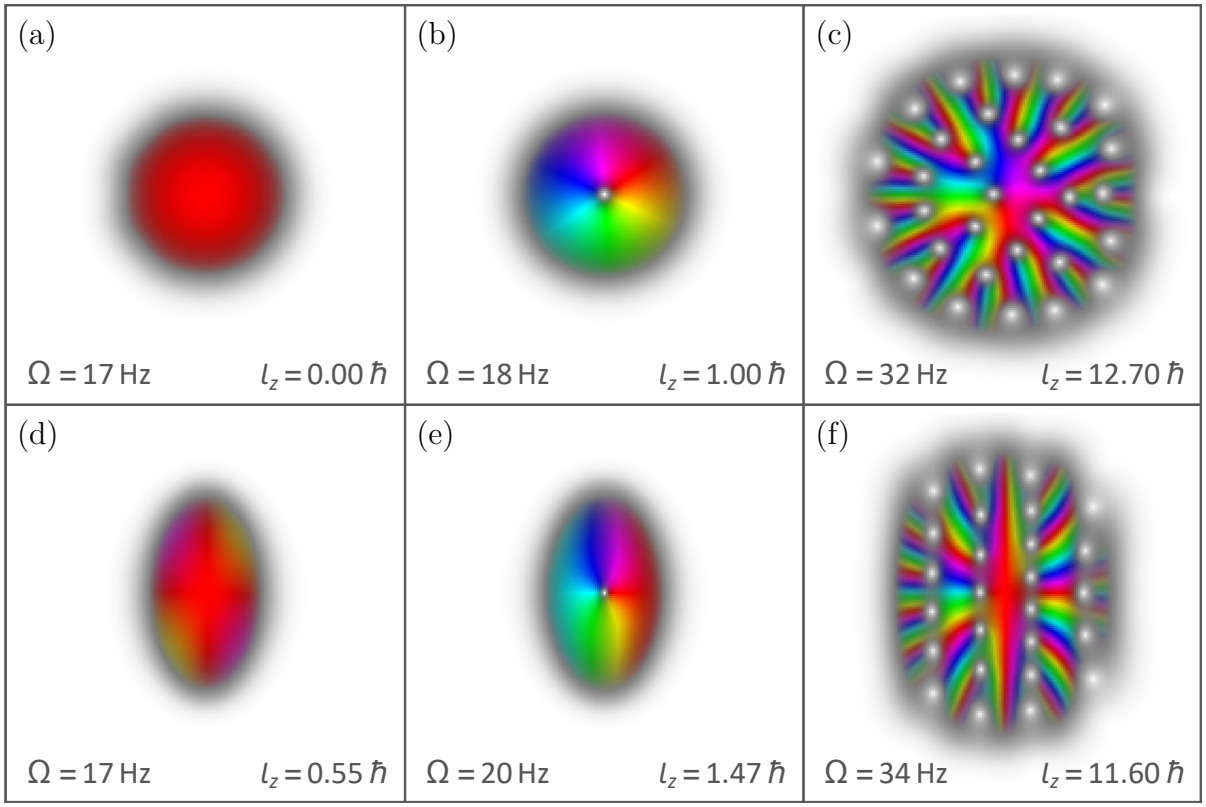

Figure 7.3.: **Ground state of a dBEC in the rotating frame** for the isotropic case with magnetic field $\boldsymbol{B} \parallel \hat{\boldsymbol{z}}$ (top) and the anisotropic case with $\boldsymbol{B} \parallel \hat{\boldsymbol{y}}$ (bottom) and various rotation frequencies Ω. In both cases, we find no (a,d), one (b,e) or many (c,f) vortices. The field of view is $(31\,\mu\text{m})^2$, see [212] for parameters.

a modified transversal trap frequency $\tilde{f}_\perp^2 = f_\perp^2 - \Omega^2$ taking into account the centrifugal force. The results are shown in fig. (7.3), where we quote the angular momentum per atom $l_z = \langle L_z \rangle / N$.

For $\boldsymbol{B} \parallel \hat{\boldsymbol{z}}$, the density distribution is isotropic and the moment of inertia vanishes according to eq. (7.3). (a) For slow rotation $\Omega < \Omega_\text{c}$ below a critical frequency Ω_c, the angular momentum per atom thereby yields zero and we find a uniform phase. (b) Above Ω_c the fluid features a single vortex at the center, which carries a single quantum $\hbar$ of angular momentum. As expected, the phase varies by 2π around the vortex core. (c) In the regime $\Omega \gg \Omega_\text{c}$ many singly-charged vortices develop forming an irregular pattern[2] due to the finite size of the system. For off-axis vortices, the angular momentum is less than $\hbar$, such that the angular momentum l_z is lower than the number of vortices. This behavior was confirmed in [214], where the lifted degeneracy of the two transverse

[2] For an infinite system, we would find the typical triangular Abrikosov lattice, which was observed in [102] with three orders of magnitude more atoms.

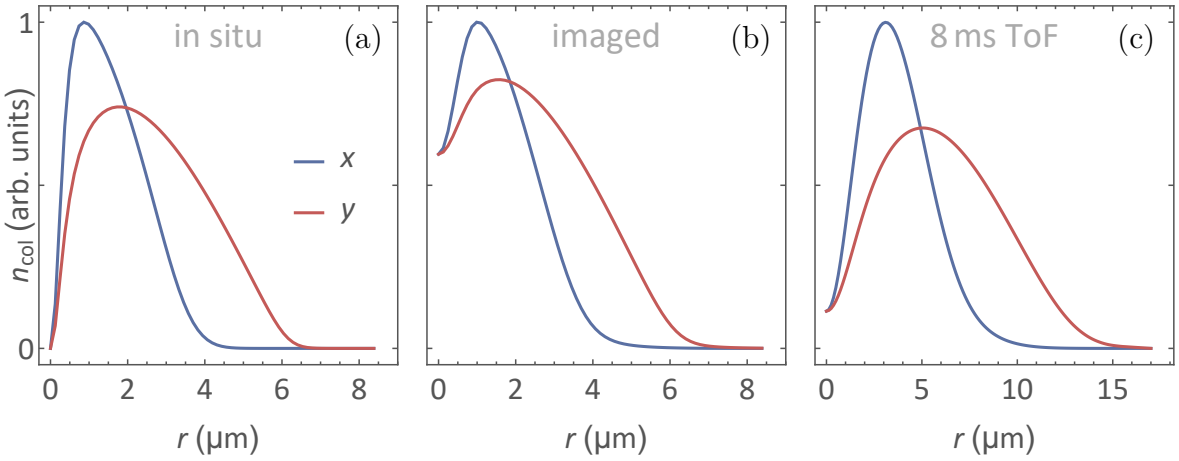

Figure 7.4.: **Imaging the anisotropic vortex core.** In (a) we show the in situ integrated column density $n_{\mathrm{col}}(r)$ along x (blue) and y (red) for a single anisotropic vortex of fig. (7.3e) [212]. By definition, the visibility v of the vortex core is 1. (b) The finite resolution of the imaging system lowers the visibility to 0.4. (c) An expansion for $t_{\mathrm{tof}} = 8\,\mathrm{ms}$ enlarges the vortex core and increases the visibility to 0.9.

quadrupole modes was exploited to measure l_z of the ensemble.

In contrast, for $\boldsymbol{B} \parallel \hat{\boldsymbol{y}}$ the cloud is anisotropic in the xy plane leading to a finite moment of inertia. (d) With increasing rotation frequency Ω, the angular momentum l_z of the sample therefore monotonously increases[3]. This leads to a quadrupole-like pattern of the phase. (e) We find the first vortex for slightly higher Ω_{c}. Both effects combined lead to an angular momentum of $l_z > 1\hbar$. As dicussed in ch. 2.3.2, the healing length of a dBEC is anisotropic leading to a deformed vortex core [103], as we study later. (f) For fast rotations $\Omega \gg \Omega_{\mathrm{c}}$, we find in general less vortices compared to the isotropic case. More importantly, vortices arrange in striped patterns along the magnetic field [103, 105]. We note, that the vortex number and position depends on the intial phase distribution we use to seed the vortex patterns, such that the acquired states are ambigious for the set of parameters[4].

For a single anisotropic vortex in (e) we plot cuts along the x (blue) and y (red) directions of the in situ column density, which is integrated along the imaging axis $\hat{\boldsymbol{z}}$. As shown in fig. (7.4a), the visibility $v = 1 - n_{\mathrm{col}}(0)/\max(n_{\mathrm{col}})$ of the vortex core yields 1 in this case. With an extent on the order of the imaging resolution, which is $r_0 = 1\,\mu\mathrm{m}$ according to the Rayleigh criterion [156], we examine whether this feature can be resolved. Therefore,

[3] Additonally, there is an implicit dependence $\Theta(\Omega)$ due to the centrifugal term weakening the trap, which increases the deformation δ.

[4] The dependence of a vortices' energy on the position is very weak, leading to long convergence times for the imaginary time evolution.

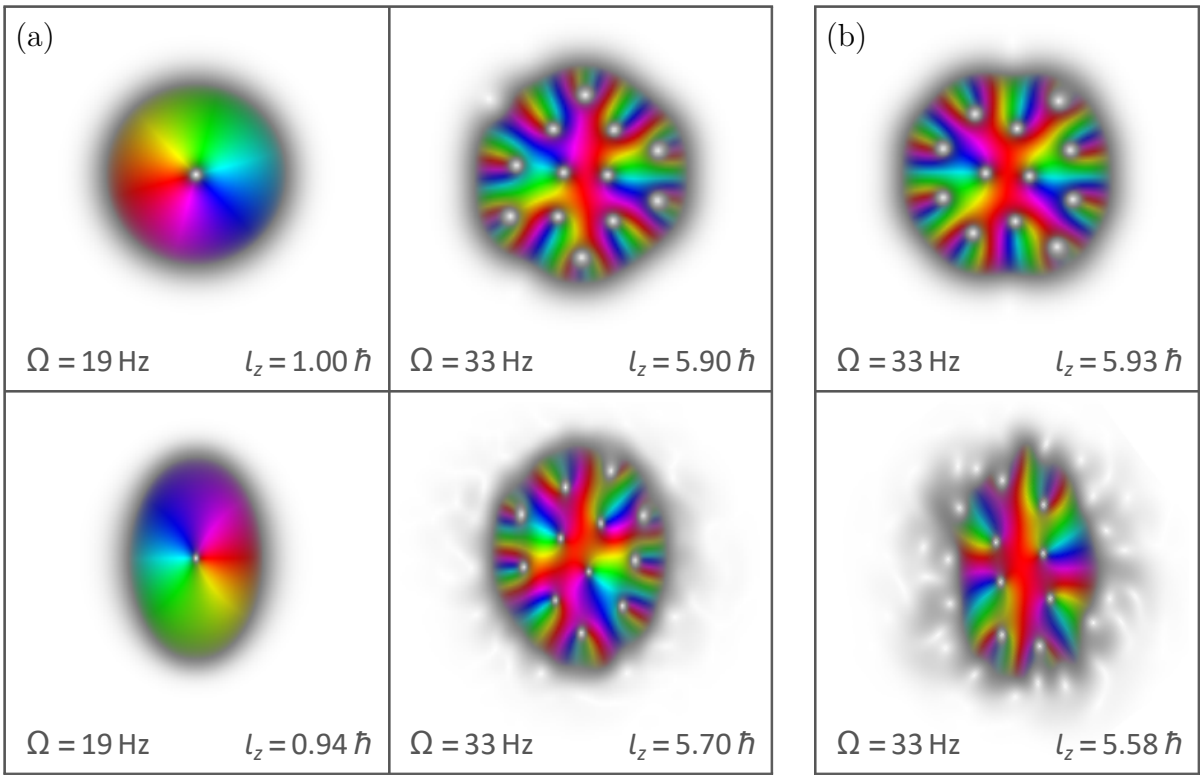

Figure 7.5.: **Dynamic creation of vortex patterns.** In (a) we tilt the magnetic field $\boldsymbol{B}$ from $\hat{\boldsymbol{z}}$ (top) within 100 ms to $\hat{\boldsymbol{y}}$ (bottom). This way, we recover the density distribution for a single vortex in the center. For multiple vortices, in (b), we additionally rotate the magnetic field at the rotation frequency, while tilting it towards the xy plane within 200 ms. With this method, vortices align in a striped pattern. The field of view is $(20\,\mu\text{m})^2$, see ref. [212] for parameters.

we compute the convolution of the in situ column density with the experimental point spread function, as shown in fig. (7.4b). Thus, the maximum visibility for in situ images is $v = 0.4$, which is additionally decreased due to thermal atoms and subject to experimental noise, such that vortices likely cannot be detected. Conveniently, we can increase the visbility by a time-of-flight expansion for e.g. $t_{\text{tof}} = 8\,\text{ms}$. As shown in fig. (7.4c), we recover a visibility $v = 0.9$ this way, which should allow to detect vortices under typical experimental conditions. Ref. [103] predicts additional modulations on the density profile, for a dBEC close to the stability threshold. We verified this effect for our experimental parameters, but the density modulations are typically smaller than the imaging resolution even after the expansion and might therefore prove hard to observe.

For the seminal experiments in [18, 22, 102], the gas is stirred with a laser beam already during the evaporation phase, such that the transition from classical to quantum gas and subsequent cooling occurs under constant rotation. For the states of interest with a

fixed magnetic field $\boldsymbol{B} \parallel \hat{\boldsymbol{y}}$ in the rotating frame, we would therefore need to continuously rotate the magnetic field in the xy plane at the same rotation frequency Ω in the laboratory frame. As this might prove hard to realize experimentally, we investigate other ways to dynamically create these states in the following.
For the first method we aim to utilize a rotation of the magnetic field in the xy plane to transfer angular momentum to the cloud. Since there is a finite moment of inertia caused by magnetostriction of the dBEC, the density distribution rotates with the magnetic field axis. To avoid an excitation of the scissors or other collective modes, see ch. 5, we increase the rotation frequency from $\Omega = 0$ to 35 Hz in 1 s. For the configuration in [212], we can thereby transfer $l_z \sim 3\,\hbar$ to the rotating sample. Unfortunately, vortices do not form with this method due to the large aspect ratio $\sigma_y/\sigma_x \sim 2.4$ of the cloud.
In fig. (7.5a), we propose a second method, where we generate vortices by stirring in an isotropic configuration[5] with $\boldsymbol{B} \parallel \hat{\boldsymbol{z}}$ and subsequently tilt the magnetic field along $\hat{\boldsymbol{y}}$ within 100 ms. With this approach, the created vortices are preserved and we can reproduce the presented density distribution around a single vortex in the center similar to the ground state. Yet, off-center vortices rotate around the center and therefore with respect to the fixed magnetic field, which prevents the observation of striped vortex patterns this way. In order to realize the latter, we extend this method and therefore additionally rotate the magnetic field about the $\hat{\boldsymbol{z}}$ axis while tilting it in the xy plane. This way, we obtain the density distribution in fig. (7.5b), where a stable "striped" vortex pattern rotates with the magnetic field axis. We note, that a tilt time of at least 200 ms is necessary to observe this effect for this example.
Finally we conclude, that anisotropic vortex cores and striped vortex arrays, as predicted in [103, 105], should indeed be observable with our experiment and point out experimental techniques to probe these effects.

[5] For the simulation, we compute the ground state in the rotating field, then switch off the rotation and tilt the magnetic field in real time evolution to study the dynamics.

Chapter 8

Conclusion

In this thesis, we have investigated macroscopic quantum states of ultracold bosonic atoms with a dominant dipolar interaction. These investigations include both extensive numerical simulations and novel experiments. A part of this thesis was devoted to the development of these simulations, which were crucial to shape our present knowledge of the quantum droplet state. Furthermore, they have proven to be an important tool to find parameter regimes, for which the desired effects can be observed under experimental conditions.

With this tool, we predicted striped ground states consisting of multiple droplets, which are induced by the frustration of the droplet along the polarization axis of the dipoles. These are especially interesting, because the droplets can share a common phase, which makes them a possible realization of a supersolid state of matter. In the experiments, we indeed were able to create states with multiple droplets by tilting the magnetic field in an highly anisotropic harmonic trapping potential. In contrast to previous experiments, where we induced the transition to the droplet state by a variation of the contact interaction, the new protocol provides control over the mean-field dipolar interaction. The experimentally realized multi-droplet states are likely metastable and we did not find the fixed phase relation between neighboring droplets, that would be a marker for supersolidity. Based on condensates in double-well potentials we developed a model that confirms this behavior and also predicts a parameter range where phase-coherence could be established, a fact that we also verified using our numerical simulations. With a better understanding of this process, we should be able to reach the regime, where the phase link is robust against thermal and quantum fluctuations.

Future work in this direction could be guided towards higher density, where the quantum fluctuations are more pronounced. In this regime, we predict *labyrinth* and *wet foam* patterns, see fig. (8.1), which are similar to the structures observed in classical ferrofluids

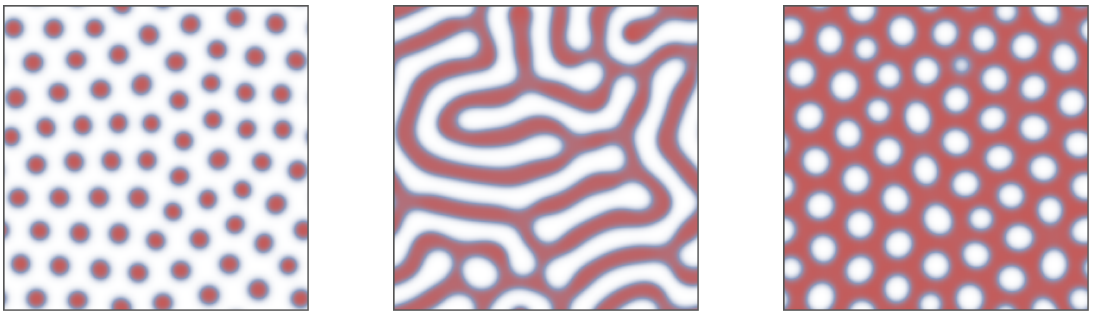

Figure 8.1.: **Self-organisation in a dipolar quantum gas.** With increasing density, there is a transition from single isolated droplets, via a labyrinth arrangement to a wet foam pattern. The images show the ground state of the eGPE for ^{164}Dy atoms in a box with in-plane periodic boundary conditions. The density is $n_{2D} = \{1.3, 4.0, 6.3\} \times 10^4\,\mu\text{m}^{-2}$ (left to right), see [215] for further parameters.

[141]. Unlike the striped states we investigated in this thesis, for these states the problem of missing phase links is solved. We therefore expect these states to have a robust uniform phase, making them excellent candidates for the realization of a supersolid state of matter and the study of self-organisation in a dipolar quantum gas.

Regarding the internal properties of the quantum droplet, we discussed the nature of the scissors mode and presented measurements of both the scissors and the quadrupole mode. Based on a time-dependent model of the variational ansatz, we extracted a background scattering length $a_{bg} = 69(4)\,a_0$ for the isotope ^{164}Dy. Contradicting a previous measurement of the critical atom number for the stability of a self-bound droplet, we further investigated effects influencing the critical atom number. We found good agreement for a temperature-dependent enhancement of the dipolar interaction, which is within a simple assumption compatible with higher values of a_{bg} obtained in non-degenerate thermal samples. As shown in fig. (8.2), new measurements for larger self-bound droplets of the isotope ^{162}Dy point towards a systematic shift supporting this claim. We infer that dipolar scattering is not universal for temperatures below 1 µK and further experimental and theoretical studies are needed to understand this effect. Cross-dimensional relaxation measurements of non-degenerate samples should be appropriate to address this question over a wide temperature range [184]. For lower temperatures, an optical lattice can be used to distinguish the contact and dipolar contributions of the interactions [46].

With thermometry in mind, we also investigated the immersion of fermionic impurities in self-bound bosonic quantum droplets. We found, that indeed a few dipolar fermions can be trapped inside a droplet and calculated the corresponding bound states. Based on this knowledge, we plan to use such an impurity to measure the temperature of the droplet and other properties non-destructively. Furthermore, we predict the pancakelet, which is

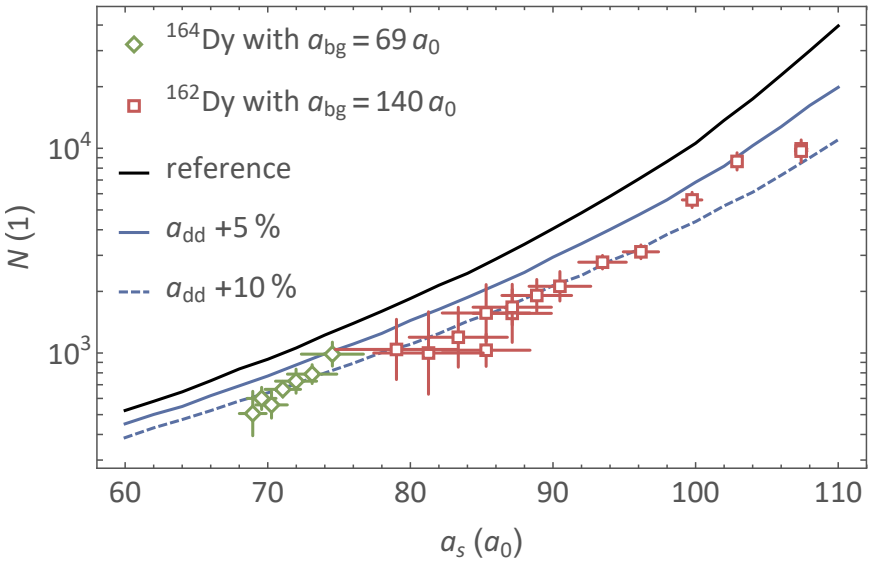

Figure 8.2.: **Critical atom number of a self-bound droplet revisited.** New independent measurements with self-bound droplets of ^{162}Dy (red), which we can produce with higher atom number, point to a systematic shift towards lower critical atom number. Background scattering lengths a_{bg} are given to the best of our knowledge. See fig. (6.2) for more details.

a two-dimensional variation of the droplet for an inverted dipolar interaction.

The dipolar interaction not only gives rise to the fascinating field of dipolar quantum droplets, it also alters the excitation spectrum and thus the superfluid properties of a dipolar condensate. In this thesis, we reported the first transport measurements of such a dBEC, where we found an anisotropic critical velocity for the onset of dissipation in the superfluid. The measured anisotropy of both the critical velocity and the heating rate are in excellent agreement with our numerical studies. As an outlook we presented simulations of dipolar vortices, where we evaluated ways to observe both the previously predicted deformation of the vortex core and novel striped vortex lattices. Based on these considerations, we expect to observe these predictions in future experiments.

While we investigated many-body effects of dipolar bosons in this thesis, our experiment is also capable to produce degenerate Fermi gases. With the dipolar interaction single component gases are particularly interesting, since they are expected to exhibit p-wave superfluidity with anisotropic pairing [168].

Ultimately, we plan to move from studies of the bulk behavior in harmonic traps to the investigation of atoms in optical lattices. To this end, a next-generation apparatus for site- and energy-resolved quantum gas microscopy is currently under development. In order to obtain a sizeable next-neighbor dipolar interaction, an UV optical lattice resulting in a lattice spacing of 180 nm will be used, which we will combine with super-resolution

techniques to optically resolve single lattice sites. The energy of atoms in the lattice can further be probed by a narrow optical transition of $\sim 60\,\mathrm{Hz}$ linewidth. Taken together these novel techniques will allow us to obtain unprecedented and exciting insights ranging from the microscopic processes all the way to the macroscopic bulk behavior of dipolar quantum systems.

Paving the way for the study of dipolar quantum matter with even stronger correlations, the creation of quantum gases from heteronuclear molecules has long been investigated and only very recently been achieved with the creation of the first degenerate Fermi gas of $^{40}\mathrm{K}^{87}\mathrm{Rb}$ [216]. In comparison to the magnetic DDI of dysprosium atoms such molecules can have an electric dipolar interaction, that is 15 times stronger for KRb or even few orders of magnitude stronger for others, once they are polarized by an external field [61].

Appendix A

DyGPE: Solving the eGPE

As introduced in ch. 2.5, we implemented a C/C++ program to solve the extended Gross-Pitaevskii equation for a wavefunction discretized on a three-dimensional grid. Here we describe the implementation details and further show how the program is installed and used. The structure of this program is inspired by D. Peter's GPE solver [217], whose diploma thesis is a good introduction to the topic [218].

A.1. Implementation

In order to cover all processes discussed in this thesis, we extend the Hamiltonian of the eGPE in eq. (2.21) by three-body losses [35] and the contribution in the rotating frame [213], which yields

$$H = \underbrace{-\frac{\hbar^2\nabla^2}{2m} - \Omega L_z}_{H_\nabla} + \underbrace{V_{\text{ext}} + g|\psi|^2 + \Phi_{\text{dd}} + g_{\text{qf}}|\psi|^3 - i\frac{\hbar L_3}{2}|\psi|^4}_{H_{|\psi|}} . \tag{A.1}$$

Split-step method

In general, we are interested in the time evolution of the wavefunction. Therefore, we implement the split-step Crank-Nicolson method following ref. [219] and split the Hamiltonian in a part with spatial derivatives, H_∇, and the other contributions, $H_{|\psi|}$, depending on the modulus of the wavefunction. Making use of the Baker-Hausdorff formula[1], the time evolution can be separated as

$$\psi(t) = e^{-i(H_\nabla + H_{|\psi|})t/\hbar}\,\psi(0) \quad \Rightarrow \quad \psi(t+\Delta t) \approx e^{-iH_\nabla \Delta t/\hbar}\, e^{-iH_{|\psi|}\Delta t/\hbar}\,\psi(t) \tag{A.2}$$

[1] The two parts of the Hamiltonian do not commute in general.

introducing an error $\propto (\Delta t)^2$ which in turn makes it necessary to carry out the evaluation in many small timesteps $\Delta t \ll 1$. For a single timestep we can directly apply the latter exponential in real space. For the derivative part, one can resort to a spectral Fourier method, see e.g. [144, ch. A.1]. Alternatively, we employ a semi-implicit scheme, that is unconditionally stable and can handle arbitrary derivatives, as we explain in the following.

Crank-Nicolson method

To compute the spatial derivatives we employ the semi-implicit Crank-Nicolson finite difference (CNFD) method. The derivatives for the three spatial directions are applied sequentially such that we only need to cover a one-dimensional differential equation of the form

$$\gamma\, \partial_t \psi(x,t) = H_{\partial x}\psi(x,t) = \left(-\frac{1}{2}\partial_x^2 + c\, \partial_x\right)\psi(x,t) \tag{A.3}$$

with constants $\gamma, c \in \mathbb{C}$. The discretization of the wavefunction ψ on a complex grid ψ_k^n with temporal index n and spacing Δt as well as spatial index k and spacing Δx is

$$\begin{aligned}\frac{\gamma}{\Delta t}\left(\psi_k^{n+1} - \psi_k^n\right) &= -\frac{1}{4(\Delta x)^2}\left[\left(\psi_{k+1}^{n+1} - 2\psi_k^{n+1} + \psi_{k-1}^{n+1}\right) + \left(\psi_{k+1}^{n} - 2\psi_k^{n} + \psi_{k-1}^{n}\right)\right] \\ &\quad + \frac{c}{4\Delta x}\left[\left(\psi_{k+1}^{n+1} - \psi_{k-1}^{n+1}\right) + \left(\psi_{k+1}^{n} - \psi_{k-1}^{n}\right)\right]. \end{aligned} \tag{A.4}$$

Solving for the next timestep $n+1$ we obtain

$$\begin{aligned}&\underbrace{\left(\frac{\Delta t}{4\gamma(\Delta x)^2} - \frac{c\Delta t}{4\gamma\Delta x}\right)}_{A_+}\psi_{k+1}^{n+1} + \underbrace{\left(1 - \frac{\Delta t}{2\gamma(\Delta x)^2}\right)}_{A_0}\psi_k^{n+1} + \underbrace{\left(\frac{\Delta t}{4\gamma(\Delta x)^2} + \frac{c\Delta t}{4\gamma\Delta x}\right)}_{A_-}\psi_{k-1}^{n+1} \\ &\qquad = \underbrace{-\frac{\Delta t}{4\gamma(\Delta x)^2}\left(\psi_{k+1}^{n} - 2\psi_k^{n} + \psi_{k-1}^{n}\right) + \frac{c\Delta t}{4\gamma\Delta x}\left(\psi_{k+1}^{n} - \psi_{k-1}^{n}\right) + \psi_k^n}_{B_k}. \end{aligned} \tag{A.5}$$

Above equation is of tridiagonal form

$$A_+\psi_{k+1}^{n+1} + A_0\psi_k^{n+1} + A_-\psi_{k-1}^{n+1} = B_k \tag{A.6}$$

where the A cofficients are constants and only B_k is known for the current timestep n. To determine ψ^{n+1} we use a one-step forward recursion relation

$$\psi_{k+1}^{n+1} = \alpha_k\psi_k^{n+1} + \beta_k \tag{A.7}$$

which is plugged into (A.6)

$$A_+\left(\alpha_k\psi_k^{n+1}+\beta_k\right)+A_0\psi_k^{n+1}+A_-\psi_{k-1}^{n+1}=B_k \tag{A.8}$$

to finally solve for

$$\psi_k^{n+1}=\underbrace{\frac{-A_-}{A_+\alpha_k+A_0}}_{\alpha_{k-1}}\psi_{k-1}^{n+1}+\underbrace{\frac{B_k-A_+\beta_k}{A_+\alpha_k+A_0}}_{\beta_{k-1}}\,. \tag{A.9}$$

Thus we obtain a set of backward recursion relations for α_{k-1} and β_{k-1} which are used to determine α_k and β_k for the whole grid.
For a grid with N_x points, where the index k ranges from $k=0$ to N_x-1, we first compute these coefficients in a backward sweep from $k=N_x-2$ to 0 using (A.9). The initial values are $\alpha_{N_x-1}=\beta_{N_x-1}=0$ ensuring $\psi_{N_x-1}^{n+1}=0$ at the boundary. In a second step we can then determine the wavefunction via ansatz (A.7) in a forward sweep from $k=0$ to N_x-2 with boundary conditions $\psi_0^{n+1}=0$.

Dipolar Interaction

As detailed in [61] the dipolar interaction potential Φ_{dd} is most easily calculated in Fourier space, since the convolution becomes a simple multiplication. For an arbitrary field direction $\hat{\boldsymbol{B}}$ under the angles α and β with respect to $\hat{\boldsymbol{z}}$ in real space, we find the relation

$$\begin{aligned} V_{\mathrm{dd}}(\boldsymbol{k}) &= -1+3\left(\hat{\boldsymbol{k}}\cdot\hat{\boldsymbol{B}}\right)^2=-1+3\left[\begin{pmatrix}\cos\phi_k\,\sin\theta_k\\ \sin\phi_k\sin\theta_k\\ \cos\theta_k\end{pmatrix}\cdot\begin{pmatrix}\cos\beta\sin\alpha\\ \sin\beta\sin\alpha\\ \cos\alpha\end{pmatrix}\right]^2 \\ &= -1+3\left[\cos(\phi_k-\beta)\sin\theta_k\sin\alpha+\cos\theta_k\cos\alpha\right]^2 \end{aligned} \tag{A.10}$$

for the dipolar interaction in momentum space, which reduces to the well-known form eq. (2.10) for $\hat{\boldsymbol{B}}\parallel\hat{\boldsymbol{z}}$. For the computation of the density distribution $\tilde{n}(\boldsymbol{k})$ we use a fast fourier transformation (FFT) [220], which assumes a periodic repetition of the input signal and thus a periodic array of density distributions. In order to avoid a long-range interaction with these mirror images the physical dimension of the grid must be chosen accordingly. To avoid large unused areas of the grid, the range of the dipolar interaction can be limited to a cut-off range R. As introduced in the appendix of [148], one possibility is the corrected dipolar interaction

$$V_{\mathrm{dd,cut}}(\boldsymbol{k})=V_{\mathrm{dd}}(\boldsymbol{k})\left[1+3\frac{\cos(kR)}{(kR)^2}-3\frac{\sin(kR)}{(kR)^3}\right] \tag{A.11}$$

yielding zero for $r > R$ in real space. This choice of cut-off is isotropic and thus compatible with any magnetic field direction.

Imaginary time evolution

For imaginary time evolution, we follow the same propagation method and replace the timestep Δt by its imaginary counterpart $-i\Delta t$, see e.g. [144, ch. A.3]. Upon propagation of the wavefunction, all excitations decay over time and the wavefunction ψ converges towards the ground state of the system. We typically start with an initial Gaussian wavefunction and stop the evolution, when the relative change of all observables is below 10^{-3} within an imaginary millisecond. The mentioned observables are all energy contributions, the variance in all directions of the density distributions and the peak density. The acquired state is then considered the ground state, although there is no guarantee that we reach the real ground state.

Thermal Noise

In order to model thermal fluctuations we follow the approach in [50, 221] and randomly add atoms in the single-particle eigenstates ϕ_n with energy ϵ_n in the harmonic potential. To resemble a thermal distribution $T < T_\mathrm{c}$, the random complex coefficient α_n is chosen according to a Bose-Einstein distribution restricted to modes with $\epsilon_n \leq 2k_\mathrm{B}T$. The final state then reads

$$\psi_\mathrm{thermal} = \psi + \sum_n \alpha_n \phi_n \quad \text{with} \quad \langle |\alpha_n|^2 \rangle = \frac{1}{e^{\epsilon_n / k_\mathrm{B}T} - 1} + \frac{1}{2}\,. \tag{A.12}$$

Although resembling thermal noise, we emphasize that the evolution of these atoms follows the eGPE equation and is thus fully coherent. To properly take into account the evolution at finite temperature one needs to resort to more involved calculations using c-field techniques [221].

A.2. Instructions

The code relies on the compiler g++ and the FFTW library with OpenMP support for parallelization. A document summarizing the simulation results is created with python3 making use of matplotlib. Under Debian Stretch, the necessary packages to compile, run and evaluate the simulations can be installed by the command:

```
apt-get install g++ libfftw3-dev python3-numpy python3-scipy python3-matplotlib
```

In fig. (A.1), we show a simple run file `name123.cc`, which can be executed via the command `make name123` when placed in the same directory as the makefile.
Available commands for the simulation are listed in `src/simulation.h`. After instantiation of the `Simulation` class, we typically specify the timestep and the dimensions of the grid as well as its physical size. After the grid is specified, we can add various external potentials and specifiy the interactions. Based on this, the grid is populated with a certain number of atoms, where the approximate size is automatically determined by an analytical formula for the BEC. This way, the initial wavefunction is close to the ground state in the case of the BEC and convergence of imaginary time evolution via the command `runImagFindEquilibrium` is faster. The command `doStepsRealRamp` for the real time evolution periodically calls `Simulation::doRampUpdate`, which is used to implement time-dependent behavior of e.g. the trapping potential. Finally, the data is moved to a specified folder and automatically evaluated via `eval.py` creating a summary document.
We further supply a real-world run file, see fig. (A.2), which was used to calculate the simulation data in fig. (2.10a,b). There we additionally parallelize the execution of the parallelized simulations with 32 threads each to make use of our multi-processor computers efficiently.

Figure A.1.: Simple example run file to get started.

```
/* DYGPE RUN */
#include "src/simulation.h"

void Simulation::doRampUpdate(int index, double tRel /*1*/, double tAbs /*ms*/) {
    return;
}

int main()
{
    // sample variable for the trap frequency
    int N = 1e4;
    // create simulation instance and set a timestep of 10^-3 sim. units
    Simulation sim;
    sim.setTimeStep(1e-3);
    // set isotropic grid with 2^6 points and physical length of 8 sim. units
    sim.setGridLog(5,5,5, 10,10,10);
    // add a spherical harmonic trap with omega = 2 pi * 100 Hz
    sim.setHarmonicTrap(100);
    // set interactions: a_s (a0), a_dd (a0) and quant. fluc. on or off (1)
    sim.setInteractionsTwoBody(100, 100, 1);
    // put initial gaussian wavefunction with 10^4 atoms
    sim.populateAtoms(N);
    // do imag. time evolution until rel. change of all observables < 10^-3
    sim.runImagFindEquilibrium(1e-3, 1e23);
    // real time evo. for 5 ms, taking 3 snapshots of the cloud
    sim.doStepsReal(5, 3);
    // move data to parametric folder
    sim.moveData("testrun_N%05d", N);
    // simulation finished
    return 0;
}

/* this is a working example aiming for fast execution.
 * for more accurate computation the grid size should be increased
 * and the time step decreased.
 */
```

Figure A.2.: Parallelized run file used to calculate the points in fig. (2.10a,b).

```
/* DYGPE RUN */
#include "src/simulation.h"

void Simulation::doRampUpdate(int index, double tRel /*1*/, double tAbs /*ms*/) {
    return;
}

int main() {
    // parent process should ignore signals
    signal(SIGQUIT, SIG_IGN);
    // global parameters
    int G = 7; double L = 20;
    int N = 10; int A = 70; int F = 70;

for (A = 65; A <= 145; A += 5) {
    // fork & start simulation
    if (fork()) { sleep(1); continue; }

    Simulation sim(32);
    sim.setDipoleCutOffMethod(1);
    sim.setTimeStep(5e-4);
    // determine size of ground state with starting atom number
    sim.setGridLog(G, G, G+1, L, L, 2*L);
    sim.setHarmonicTrap(F);
    sim.setInteractionsTwoBody(A, 131, 1);
    sim.populateAtoms(1000*N, 1e-6, 1e-6, 3e-6);
    sim.runImagFindEquilibrium(1e-3, 1e23);
    // resize properly and find ground state again
    printf("LENGTH = %.3f\n", sim.stats[17]);
    L = 2. * sim.stats[17];
    sim.setGridLog(G, G, G+1, L, L, 2*L);
    sim.setHarmonicTrap(F);
    sim.setInteractionsTwoBody(A, 131, 1);
    sim.populateAtoms(1000*N, 1e-6, 1e-6, 3e-6);
    sim.runImagFindEquilibrium(5e-4, 1e23);

    sim.outPotentials();

    // save values
    sim.moveData("r042/f05_gausscompare1_G%1d_A%03d", G, A);

    // end simulation, child finished
    return 0;
}

    // wait for children to finish
    while (wait(NULL) > 0); return 0;
}
```

Appendix B

Three-Body Losses in Dy-164

In an effort to extend the lifetime of quantum droplets, which is determined by the losses due to three-body recombination, we measured the latter over a wide magnetic field range.

B.1. The thermal gas

A classical gas of atoms, called a *thermal gas* here, in a harmonic trapping potential E_{pot} follows the Maxwell-Boltzmann distribution

$$n(\boldsymbol{r}) = n_0 \mathrm{e}^{-E_{\mathrm{pot}}(\boldsymbol{r})/k_B T} \qquad \text{with} \qquad E_{\mathrm{pot}} = \frac{1}{2} m \left(\omega_x^2 x^2 + \omega_y^2 y^2 + \omega_z^2 z^2\right) \tag{B.1}$$

with a peak density $n_0 = N(2\pi\bar{\sigma}^2)^{-3/2}$ fixed by the total atom number $N = \int \mathrm{d}\boldsymbol{r}\, n(\boldsymbol{r})$ and the mean size $\bar{\sigma} = (\sigma_x\sigma_y\sigma_z)^{1/3}$. From the resulting Gaussian density distribution, we obtain the sizes $\sigma_k^2 = k_{\mathrm{B}}T/m\omega_k^2$ in an anisotropic trap with mean frequency $\bar{\omega} = (\omega_x\omega_y\omega_z)^{1/3}$. An important quantity is the phase-space density $\mathcal{D} = n_0\,\lambda_{\mathrm{T}}^3 = N\left(\frac{\hbar\bar{\omega}}{k_{\mathrm{B}}T}\right)^3$, which is conserved for an adiabatic change of the trapping frequencies [222].
Here, we are interested in the investigation of three-body losses in such a classical sample of atoms. Following [223], we therefore define the local *three-body* loss rate as $L_3\, n(\boldsymbol{r})^3$. To derive ensemble quantities we integrate over the whole distribution, which leads to the loss per atom

$$\frac{\dot{N}}{N} = -\frac{1}{N}\int \mathrm{d}\boldsymbol{r}\, L_3\, n(\boldsymbol{r})^3 = -L_3 \underbrace{\frac{N^2}{\sqrt{27}\,(2\pi)^3\,\bar{\sigma}^6}}_{\langle n^2\rangle} = -\underbrace{\frac{L_3}{\sqrt{27}}\left(\frac{m\bar{\omega}^2}{2\pi k_{\mathrm{B}}}\right)^3}_{\gamma}\frac{N^2}{T^3} \tag{B.2}$$

expressed by the accessible quantities N and T. Additional losses in the experiment are

caused e.g. by collisions with the background gas, which we include by the *one-body* loss rate α. This way, we arrive at the differential equation

$$\dot{N} = -\alpha\, N - \gamma\, N^3/T^3\,. \tag{B.3}$$

The underlying process for such three-body losses is the recombination of the three atoms, such that two atoms form a molecule while the third one gains the binding energy of the dimer additionally heating the sample. For a single atom lost from the trap, the temperature gain is thus the total heating energy $k_\mathrm{B}(T + T_\mathrm{h})$ per average energy $3k_\mathrm{B}T$ of the trapped particle. This way, we obtain

$$\frac{\dot{T}}{T} = -\frac{\dot{N}}{N}\,\frac{k_B(T+T_\mathrm{h})}{3k_\mathrm{B}T} = \gamma\,\frac{N^2}{T^3}\,\frac{T+T_\mathrm{h}}{3T}\,, \tag{B.4}$$

which we use in conjunction with eq. (B.3) to simultaneously fit the experimental data to both differential equations.
We note, that the heating energy $k_\mathrm{B}T_\mathrm{h}$ in ref. [56] is neglected, which results in a simpler relation

$$\dot{N} = -\underbrace{\frac{\gamma}{T_0^3}}_{\gamma_0}\,\frac{N^4}{N_0} \quad \Rightarrow \quad N(t) = \frac{N_0}{\left(1+3\gamma_0 N_0^2\, t\right)^{1/3}} \tag{B.5}$$

for the atom number only, where an initial temperature T_0 is assumed. There, one-body losses are neglected since the measurement time of 1 s is short compared to the lifetime $1/\alpha \sim 30\,\mathrm{s}$.

B.2. Measurement

In the experiment, we prepare a thermal sample of atoms at a temperature around 180 nK by forced evaporative cooling in a magnetic field region with small losses. In order to boost the density of the sample and thus the timescale for losses, we then increase the laser power of the traps by a factor 1.3 within 150 ms. Subsequently, we ramp the magnetic field to the desired value within 30 ms and hold the sample prior to imaging for a variable time of up to 5 s. The acquired atom number and temperature are then simultaneously fitted to eq. (B.3) and eq. (B.4). This way, we obtain the loss coefficient L_3 as presented in fig. (B.1). Losses in the BEC phase are additionally suppressed by a factor of 3! [224].

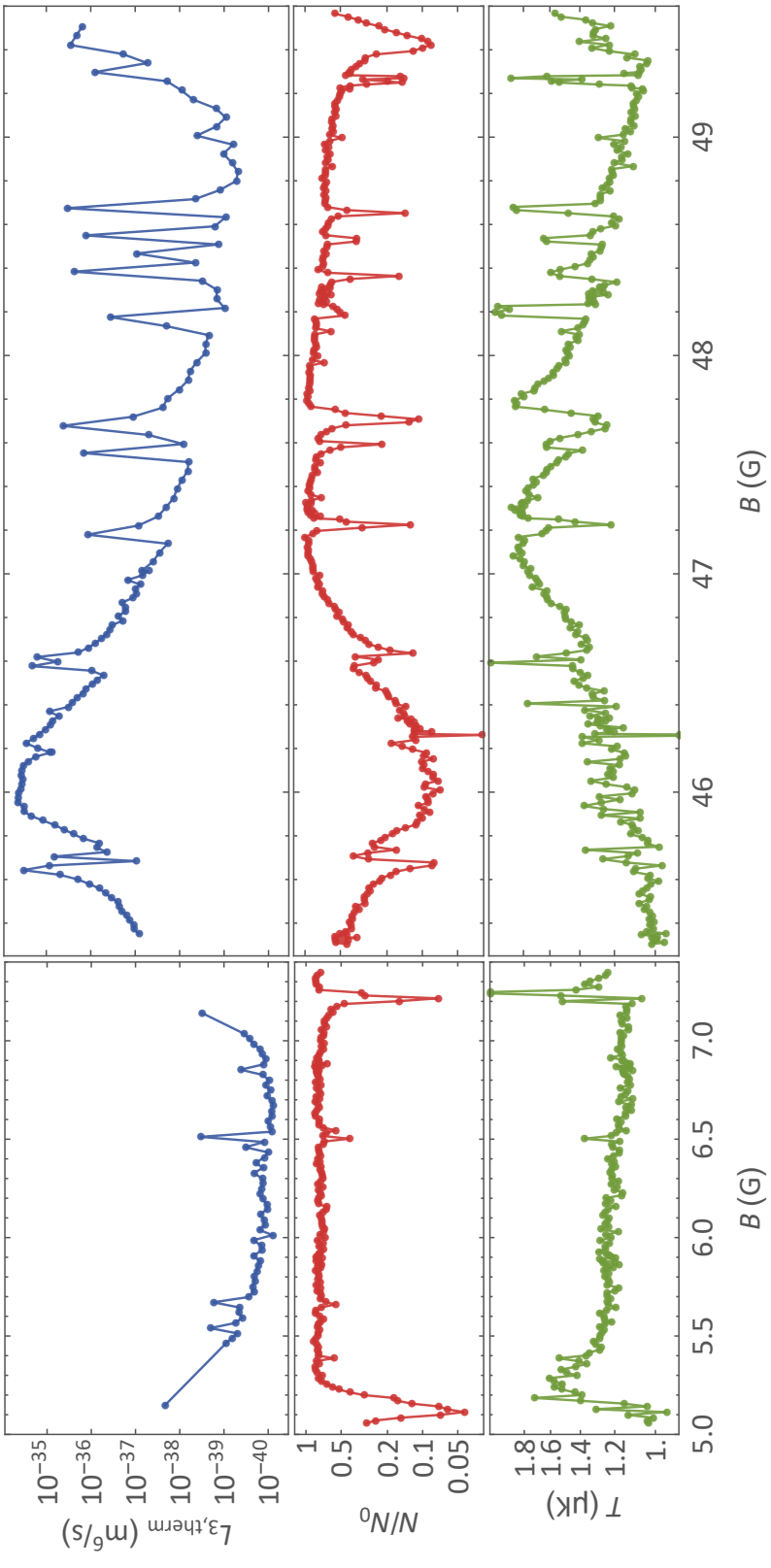

Figure B.1.: **Three-Body loss coefficient L_3 and Feshbach spectrum for ^{164}Dy.** For the former, we take a series of points with variable hold time for each magnetic field value and extract the loss coefficient, see main text. For the Feshbach spectrum, we take three single measurements for each magnetic field value and show the mean atom number and temperature. For the broader resonance located at 46.0 G we observe the zero crossing of the scattering length at 47.2 G, which is determined by a maximum in temperature due to reduced thermalization, and the minimum of three-body losses at 48.8 G.

Bibliography

[1] H. Kadau, M. Schmitt, M. Wenzel, C. Wink, T. Maier, I. Ferrier-Barbut, and T. Pfau, *Observing the Rosensweig instability of a quantum ferrofluid*, Nature **530**, 194 (2016). pp. 14, 34, 40, 45, 47, 49, 59, 62, 64, 67

[2] I. Ferrier-Barbut, H. Kadau, M. Schmitt, M. Wenzel, and T. Pfau, *Observation of Quantum Droplets in a Strongly Dipolar Bose Gas*, Phys. Rev. Lett. **116**, 215301 (2016). pp. 14, 34, 47, 49, 62, 67, 79

[3] M. Schmitt, M. Wenzel, F. Böttcher, I. Ferrier-Barbut, and T. Pfau, *Self-bound droplets of a dilute magnetic quantum liquid*, Nature **539**, 259 (2016). pp. 15, 40, 41, 45, 65, 67, 81, 83–85, 87

[4] I. Ferrier-Barbut, M. Schmitt, M. Wenzel, H. Kadau, and T. Pfau, *Liquid quantum droplets of ultracold magnetic atoms*, J. Phys. B. **49**, 214004 (2016). pp. 14, 34, 45, 47, 67

[5] M. Wenzel, F. Böttcher, T. Langen, I. Ferrier-Barbut, and T. Pfau, *Striped states in a many-body system of tilted dipoles*, Phys. Rev. A **96**, 053630 (2017). pp. 34, 40, 45, 59

[6] I. Ferrier-Barbut, M. Wenzel, M. Schmitt, F. Böttcher, and T. Pfau, *Onset of a modulational instability in trapped dipolar Bose-Einstein condensates*, Phys. Rev. A **97**, 011604(R) (2018). pp. 40, 45

[7] I. Ferrier-Barbut, M. Wenzel, F. Böttcher, T. Langen, M. Isoard, S. Stringari, and T. Pfau, *Scissors Mode of Dipolar Quantum Droplets of Dysprosium Atoms*, Phys. Rev. Lett. **120**, 160402 (2018). pp. 22, 42–45, 74, 76

[8] M. Wenzel, F. Böttcher, J. Schmidt, M. Eisenmann, T. Langen, T. Pfau, and I. Ferrier-Barbut, *Anisotropic Superfluid Behavior of a Dipolar Bose-Einstein Condensate*, Phys. Rev. Lett. **121**, 030401 (2018). pp. 45, 95

[9] M. Wenzel, T. Pfau, and I. Ferrier-Barbut, *A fermionic impurity in a dipolar quantum droplet*, Physica Scripta **93**, 104004 (2018). pp. 83, 88, 90

[10] T. Maier, H. Kadau, M. Schmitt, M. Wenzel, I. Ferrier-Barbut, T. Pfau, A. Frisch, S. Baier, K. Aikawa, L. Chomaz, M. J. Mark, F. Ferlaino, C. Makrides, E. Tiesinga, A. Petrov, and S. Kotochigova, *Emergence of Chaotic Scattering in Ultracold Er and Dy*, Phys. Rev. X **5**, 041029 (2015). pp. 14, 20, 90

[11] T. Maier, I. Ferrier-Barbut, H. Kadau, M. Schmitt, M. Wenzel, C. Wink, T. Pfau, K. Jachymski, and P. S. Julienne, *Broad universal Feshbach resonances in the chaotic spectrum of dysprosium atoms*, Phys. Rev. A **92**, 060702(R) (2015). pp. 14, 20, 22, 81, 86

[12] P. L. Kapitsa, *Viscosity of Liquid Helium below the λ-Point*, Nature **141**, 74 (1938). pp. 13, 30, 95

[13] D. van Delft and P. Kes, *The discovery of superconductivity*, Physics Today **63**, 38 (2010). p. 13

[14] M. H. Anderson, J. R. Ensher, M. R. Matthews, C. E. Wieman, and E. A. Cornell, *Observation of Bose-Einstein Condensation in a Dilute Atomic Vapor*, Science **269**, 5221 (1995). p. 13

[15] K. B. Davis, M. O. Mewes, M. R. Andrews, N. J. van Druten, D. S. Durfee, D. M. Kurn, and W. Ketterle, *Bose-Einstein Condensation in a Gas of Sodium Atoms*, Phys. Rev. Lett. **75**, 3969 (1995). p. 13

[16] B. DeMarco and D. S. Jin, *Onset of Fermi Degeneracy in a Trapped Atomic Gas*, Science **285**, 1703 (1999). p. 13

[17] M. R. Andrews, C. G. Townsend, H.-J. Miesner, D. S. Durfee, D. M. Kurn, and W. Ketterle, *Observation of Interference Between Two Bose Condensates*, Science **275**, 637 (1997). pp. 14, 19

[18] K. W. Madison, F. Chevy, W. Wohlleben, and J. Dalibard, *Vortex Formation in a Stirred Bose-Einstein Condensate*, Phys. Rev. Lett. **84**, 806 (2000). pp. 14, 29, 101, 104

[19] M. Greiner, O. Mandel, T. Esslinger, T. Hänsch, and I. Bloch, *Quantum phase transition from a superfluid to a Mott insulator in a gas of ultracold atoms*, Nature **415**, 39 (2002). p. 14

[20] M. Greiner, C. A. Regal, and D. S. Jin, *Emergence of a Molecular Bose-Einstein Condensate from a Fermi Gas*, Nature **426**, 537 (2003). p. 14

[21] S. Jochim, M. Bartenstein, A. Altmeyer, G. Hendl, S. Riedl, C. Chin, J. Hecker Denschlag, and R. Grimm, *Bose-Einstein Condensation of Molecules*, Science **302**, 2101 (2003). p. 14

[22] M. W. Zwierlein, J. R. Abo-Shaeer, A. Schirotzek, C. H. Schunck, and W. Ketterle, *Vortices and superfluidity in a strongly interacting Fermi gas*, Nature **435**, 1047 (2005). pp. 14, 101, 104

[23] W. S. Bakr, A. Peng, M. E. Tai, R. Ma, J. Simon, J. I. Gillen, S. Fölling, L. Pollet, and M. Greiner, *Probing the Superfluid–to–Mott Insulator Transition at the Single-Atom Level*, Science **329**, 547 (2010). p. 14

[24] J. F. Sherson, C. Weitenberg, M. Endres, M. Cheneau, I. Bloch, and S. Kuhr, *Single-atom-resolved fluorescence imaging of an atomic Mott insulator*, Nature **467**, 68 (2010). p. 14

[25] E. Haller, J. Hudson, A. Kelly, D. A. Cotta, B. Peaudecerf, G. D. Bruce, and S. Kuhr, *Single-atom imaging of fermions in a quantum-gas microscope*, Nature Physics **11**, 738 (2015). p. 14

[26] L. W. Cheuk, M. A. Nichols, M. Okan, T. Gersdorf, V. V. Ramasesh, W. S. Bakr, T. Lompe, and M. W. Zwierlein, *Quantum-Gas Microscope for Fermionic Atoms*, Phys. Rev. Lett. **114**, 193001 (2015). p. 14

[27] M. F. Parsons, F. Huber, A. Mazurenko, C. S. Chiu, W. Setiawan, K. Wooley-Brown, S. Blatt, and M. Greiner, *Site-Resolved Imaging of Fermionic* ^{6}Li *in an Optical Lattice*, Phys. Rev. Lett. **114**, 213002 (2015). p. 14

[28] J. Klaers, J. Schmitt, F. Vewinger, and M. Weitz, *Bose-Einstein condensation of photons in an optical microcavity*, Nature **468**, 545 (2010). p. 14

[29] S. Autti, V. V. Dmitriev, J. T. Mäkinen, J. Rysti, A. A. Soldatov, G. E. Volovik, A. N. Yudin, and V. B. Eltsov, *Bose-Einstein Condensation of Magnons and Spin Superfluidity in the Polar Phase of* ^{3}He, Phys. Rev. Lett. **121**, 025303 (2018). p. 14

[30] J. Kasprzak, M. Richard, S. Kundermann, A. Baas, P. Jeambrun, J. M. Keeling, F. M. Marchetti, M. H. Szymánska, R. André, J. L. Staehli, V. Savona, P. B. Littlewood, B. Deveaud, and L. S. Dang, *Bose-Einstein condensation of exciton polaritons*, Nature **443**, 409 (2006). p. 14

[31] A. Griesmaier, J. Werner, S. Hensler, J. Stuhler, and T. Pfau, *Bose-Einstein Condensation of Chromium*, Phys. Rev. Lett. **94**, 160401 (2005). pp. 14, 36

[32] J. Stuhler, A. Griesmaier, T. Koch, M. Fattori, T. Pfau, S. Giovanazzi, P. Pedri, and L. Santos, *Observation of Dipole-Dipole Interaction in a Degenerate Quantum Gas*, Phys. Rev. Lett. **95**, 150406 (2005). pp. 14, 36, 37, 63

[33] T. Lahaye, T. Koch, B. Fröhlich, M. Fattori, J. Metz, A. Griesmaier, S. Giovanazzi, and T. Pfau, *Strong dipolar effects in a quantum ferrofluid*, Nature **448**, 672 (2007). pp. 14, 24, 36–38

[34] T. Koch, T. Lahaye, J. Metz, B. Fröhlich, A. Griesmaier, and T. Pfau, *Stabilization of a purely dipolar quantum gas against collapse*, Nature Physics **4**, 218 (2008). pp. 14, 36, 37

[35] T. Lahaye, J. Metz, B. Fröhlich, T. Koch, M. Meister, A. Griesmaier, T. Pfau, H. Saito, Y. Kawaguchi, and M. Ueda, *d-Wave Collapse and Explosion of a Dipolar Bose-Einstein Condensate*, Phys. Rev. Lett. **101**, 080401 (2008). pp. 14, 36, 37, 45, 47, 111

[36] G. Bismut, B. Pasquiou, E. Maréchal, P. Pedri, L. Vernac, O. Gorceix, and B. Laburthe-Tolra, *Collective Excitations of a Dipolar Bose-Einstein Condensate*, Phys. Rev. Lett. **105**, 040404 (2010). pp. 14, 45

[37] B. Pasquiou, E. Maréchal, G. Bismut, P. Pedri, L. Vernac, O. Gorceix, and B. Laburthe-Tolra, *Spontaneous Demagnetization of a Dipolar Spinor Bose Gas in an Ultralow Magnetic Field*, Phys. Rev. Lett. **106**, 255303 (2011). p. 14

[38] B. Pasquiou, E. Maréchal, L. Vernac, O. Gorceix, and B. Laburthe-Tolra, *Thermodynamics of a Bose-Einstein Condensate with Free Magnetization*, Phys. Rev. Lett. **108**, 045307 (2012). p. 14

[39] A. de Paz, A. Sharma, A. Chotia, E. Maréchal, J. H. Huckans, P. Pedri, L. Santos, O. Gorceix, L. Vernac, and B. Laburthe-Tolra, *Nonequilibrium Quantum Magnetism in a Dipolar Lattice Gas*, Phys. Rev. Lett. **111**, 185305 (2013). p. 14

[40] M. Lu, N. Q. Burdick, S. H. Youn, and B. L. Lev, *Strongly Dipolar Bose-Einstein Condensate of Dysprosium*, Phys. Rev. Lett. **107**, 190401 (2011). pp. 14, 53

[41] M. Lu, N. Q. Burdick, and B. L. Lev, *Quantum Degenerate Dipolar Fermi Gas*, Phys. Rev. Lett. **108**, 215301 (2012). pp. 14, 22, 53

[42] K. Aikawa, A. Frisch, M. Mark, S. Baier, A. Rietzler, R. Grimm, and F. Ferlaino, *Bose-Einstein Condensation of Erbium*, Phys. Rev. Lett. **108**, 210401 (2012). p. 14

[43] K. Aikawa, A. Frisch, M. Mark, S. Baier, R. Grimm, and F. Ferlaino, *Reaching Fermi Degeneracy via Universal Dipolar Scattering*, Phys. Rev. Lett. **112**, 010404 (2014). pp. 14, 22

[44] K. Aikawa, S. Baier, A. Frisch, M. Mark, C. Ravensbergen, and F. Ferlaino, *Observation of Fermi surface deformation in a dipolar quantum gas*, Science **345**, 1484 (2014). p. 14

[45] A. Frisch, M. Mark, K. Aikawa, F. Ferlaino, J. L. Bohn, C. Makrides, A. Petrov, and S. Kotochigova, *Quantum chaos in ultracold collisions of gas-phase erbium atoms*, Nature **507**, 475 (2014). p. 14

[46] S. Baier, M. J. Mark, D. Petter, K. Aikawa, L. Chomaz, Z. Cai, M. Baranov, P. Zoller, and F. Ferlaino, *Extended Bose-Hubbard models with ultracold magnetic atoms*, Science **352**, 201 (2016). pp. 14, 22, 108

[47] Y. Tang, W. Kao, K.-Y. Li, S. Seo, K. Mallayya, M. Rigol, S. Gopalakrishnan, and B. Lev, *Thermalization near integrability in a dipolar quantum Newton's cradle*, Phys. Rev. X **8**, 21030 (2018). pp. 14, 22

[48] D. S. Petrov, *Quantum Mechanical Stabilization of a Collapsing Bose-Bose Mixture*, Phys. Rev. Lett. **115**, 155302 (2015). pp. 14, 15, 26, 46, 49

[49] K.-T. Xi and H. Saito, *Droplet formation in a Bose-Einstein condensate with strong dipole-dipole interaction*, Phys. Rev. A **93**, 011604 (2016). pp. 14, 49

[50] R. N. Bisset and P. B. Blakie, *Crystallization of a dilute atomic dipolar condensate*, Phys. Rev. A **92**, 061603 (2015). pp. 14, 49, 114

[51] P. B. Blakie, *Properties of a dipolar condensate with three-body interactions*, Phys. Rev. A **93**, 033644 (2016). pp. 14, 49

[52] R. N. Bisset, R. M. Wilson, D. Baillie, and P. B. Blakie, *Ground-state phase diagram of a dipolar condensate with quantum fluctuations*, Phys. Rev. A **94**, 033619 (2016). pp. 14, 26, 36, 38

[53] D. Baillie, R. M. Wilson, R. N. Bisset, and P. B. Blakie, *Self-bound dipolar droplet: A localized matter wave in free space*, Phys. Rev. A **94**, 021602 (2016). pp. 14, 26, 36, 38, 40, 60, 88

[54] F. Wächtler and L. Santos, *Quantum filaments in dipolar Bose-Einstein condensates*, Phys. Rev. A **93**, 061603 (2016). pp. 14, 26, 49, 59, 85

[55] F. Wächtler and L. Santos, *Ground-state properties and elementary excitations of quantum droplets in dipolar Bose-Einstein condensates*, Phys. Rev. A **94**, 043618 (2016). pp. 14, 26, 36, 38, 40, 43–45, 49, 60, 83, 88

[56] L. Chomaz, S. Baier, D. Petter, M. J. Mark, F. Wächtler, L. Santos, and F. Ferlaino, *Quantum-Fluctuation-Driven Crossover from a Dilute Bose-Einstein Condensate to a Macrodroplet in a Dipolar Quantum Fluid*, Phys. Rev. X **6**, 041039 (2016). pp. 15, 22, 45, 80, 120

[57] C. R. Cabrera, L. Tanzi, J. Sanz, B. Naylor, P. Thomas, P. Cheiney, and L. Tarruell, *Quantum liquid droplets in a mixture of Bose-Einstein condensates*, Science **359**, 301 (2018). p. 15

[58] G. Semeghini, G. Ferioli, L. Masi, C. Mazzinghi, L. Wolswijk, F. Minardi, M. Modugno, G. Modugno, M. Inguscio, and M. Fattori, *Self-Bound Quantum Droplets of Atomic Mixtures in Free Space*, Phys. Rev. Lett. **120**, 235301 (2018). p. 15

[59] P. Cheiney, C. R. Cabrera, J. Sanz, B. Naylor, L. Tanzi, and L. Tarruell, *Bright Soliton to Quantum Droplet Transition in a Mixture of Bose-Einstein Condensates*, Phys. Rev. Lett. **120**, 135301 (2018). p. 15

[60] L. Pitaevskii and S. Stringari, *Bose-Einstein Condensation and Superfluidity* (Oxford University Press, 2016). pp. 17–20, 23, 24, 29, 35, 41, 42, 73, 75, 98, 101

[61] T. Lahaye, C. Menotti, L. Santos, M. Lewenstein, and T. Pfau, *The physics of dipolar bosonic quantum gases*, Rep. Prog. Phys. **72**, 126401 (2009). pp. 17, 21, 24, 27, 110, 113

[62] A. R. P. Lima and A. Pelster, *Quantum fluctuations in dipolar Bose gases*, Phys. Rev. A **84**, 041604 (2011). pp. 17, 25, 36, 91

[63] A. R. P. Lima and A. Pelster, *Beyond mean-field low-lying excitations of dipolar Bose gases*, Phys. Rev. A **86**, 063609 (2012). pp. 17, 25, 36

[64] S. N. Bose, *Plancks Gesetz und Lichtquantenhypothese*, Zeitschrift f. Physik **26**, 178 (1924). p. 17

[65] A. Einstein, *Quantentheorie des einatomigen idealen Gases*, in *Sitzungsberichte der Preußischen Akademie der Wissenschaften* (1924). p. 17

[66] A. Einstein, *Quantentheorie des einatomigen idealen Gases: Zweite Abhandlung*, in *Sitzungsberichte der Preußischen Akademie der Wissenschaften* (1925). p. 17

[67] J. Harms, J. P. Toennies, and F. Dalfovo, *Density of superfluid helium droplets*, Phys. Rev. B **58**, 3341 (1998). pp. 18, 42, 46

[68] C. N. Yang, *Concept of Off-Diagonal Long-Range Order and the Quantum Phases of Liquid He and of Superconductors*, Rev. Mod. Phys. **34**, 694 (1962). p. 19

[69] T. Maier, *Interactions in a Quantum Gas of Dysprosium Atoms*, PhD Thesis (University of Stuttgart, 2015). pp. 19, 22, 51–53

[70] S. Inouye, M. R. Andrews, J. Stenger, H. J. Mlesner, D. M. Stamper-Kurn, and W. Ketterle, *Observation of Feshbach resonances in a Bose-Einstein condensate*, Nature **392**, 151 (1998). p. 20

[71] C. Chin, R. Grimm, P. Julienne, and E. Tiesinga, *Feshbach resonances in ultracold gases*, Rev. Mod. Phys. **82**, 1225 (2010). pp. 20, 64

[72] P. O. Fedichev, Y. Kagan, G. V. Shlyapnikov, and J. T. M. Walraven, *Influence of Nearly Resonant Light on the Scattering Length in Low-Temperature Atomic Gases*, Phys. Rev. Lett. **77**, 2913 (1996). p. 20

[73] M. Theis, G. Thalhammer, K. Winkler, M. Hellwig, G. Ruff, R. Grimm, and J. H. Denschlag, *Tuning the Scattering Length with an Optically Induced Feshbach Resonance*, Phys. Rev. Lett. **93**, 123001 (2004). p. 20

[74] P. O. Fedichev, M. W. Reynolds, and G. V. Shlyapnikov, *Three-Body Recombination of Ultracold Atoms to a Weakly Bound s Level*, Phys. Rev. Lett. **77**, 2921 (1996). p. 20

[75] S. Giovanazzi, A. Görlitz, and T. Pfau, *Tuning the Dipolar Interaction in Quantum Gases*, Phys. Rev. Lett. **89**, 130401 (2002). pp. 21, 36, 92, 93

[76] Y. Tang, W. Kao, K.-Y. Li, and B. L. Lev, *Tuning the Dipole-Dipole Interaction in a Quantum Gas with a Rotating Magnetic Field*, Phys. Rev. Lett. **120**, 230401 (2018). pp. 21, 92, 93

[77] D. M. Stamper-Kurn and M. Ueda, *Spinor Bose gases: Symmetries, magnetism, and quantum dynamics*, Rev. Mod. Phys. **85**, 1191 (2013). p. 22

[78] B. Pasquiou, G. Bismut, Q. Beaufils, A. Crubellier, E. Maréchal, P. Pedri, L. Vernac, O. Gorceix, and B. Laburthe-Tolra, *Control of dipolar relaxation in external fields*, Phys. Rev. A **81**, 042716 (2010). p. 22

[79] A. Frisch, M. Mark, K. Aikawa, S. Baier, R. Grimm, A. Petrov, S. Kotochigova, G. Quéméner, M. Lepers, O. Dulieu, and F. Ferlaino, *Ultracold Dipolar Molecules Composed of Strongly Magnetic Atoms*, Phys. Rev. Lett. **115**, 203201 (2015). p. 22

[80] S. Yi and L. You, *Trapped condensates of atoms with dipole interactions*, Phys. Rev. A **63**, 053607 (2001). pp. 21, 36, 42

[81] C. Ticknor, *Collisional Control of Ground State Polar Molecules and Universal Dipolar Scattering*, Phys. Rev. Lett. **100**, 133202 (2008). p. 21

[82] J. L. Bohn, M. Cavagnero, and C. Ticknor, *Quasi-universal dipolar scattering in cold and ultracold gases*, New Journal of Physics **11**, 055039 (2009). p. 21

[83] R. Ołdziejewski and K. Jachymski, *Properties of strongly dipolar Bose gases beyond the Born approximation*, Phys. Rev. A **94**, 063638 (2016). pp. 22, 43, 86

[84] R. Ołdziejewski and K. Jachymski, *Erratum: Properties of strongly dipolar Bose gases beyond the Born approximation [Phys. Rev. A 94, 063638 (2016)]*, Phys. Rev. A **95**, 049901 (2017). pp. 22, 86, 87

[85] S. Hensler, J. Werner, A. Griesmaier, P. O. Schmidt, A. Görlitz, T. Pfau, S. Giovanazzi, and K. Rzazewski, *Dipolar relaxation in an ultra-cold gas of magnetically trapped chromium atoms*, Appl. Phys. B Lasers Opt. **77**, 765 (2003). p. 22

[86] M. Fattori, T. Koch, S. Goetz, A. Griesmaier, S. Hensler, J. Stuhler, and T. Pfau, *Demagnetization cooling of a gas*, Nat. Phys. **2**, 765 (2006). p. 22

[87] V. V. Volchkov, J. Rührig, T. Pfau, and A. Griesmaier, *Efficient demagnetization cooling of atoms and its limits*, Phys. Rev. A **89**, 043417 (2014). p. 22

[88] B. Naylor, E. Maréchal, J. Huckans, O. Gorceix, P. Pedri, L. Vernac, and B. Laburthe-Tolra, *Cooling of a Bose-Einstein Condensate by Spin Distillation*, Phys. Rev. Lett. **115**, 243002 (2015). p. 22

[89] N. Bogoliubov, *On the theory of superfluidity*, J. Phys. USSR **11**, 23 (1947). pp. 23, 26

[90] E. P. Gross, *Structure of a quantized vortex in boson systems*, Il Nuovo Cimento **20**, 454 (1961). p. 24

[91] L. P. Pitaevskii, *Vortex Lines in an Imperfect Bose Gas*, JETP **13**, 451 (1961). p. 24

[92] T. D. Lee, K. Huang, and C. N. Yang, *Eigenvalues and Eigenfunctions of a Bose System of Hard Spheres and Its Low-Temperature Properties*, Phys. Rev. **106**, 1135 (1957). p. 25

[93] T. T. Wu, *Ground State of a Bose System of Hard Spheres*, Phys. Rev. **115**, 1390 (1959). p. 25

[94] H. R. Glyde, S. O. Diallo, R. T. Azuah, O. Kirichek, and J. W. Taylor, *Atomic momentum distribution and Bose-Einstein condensation in liquid ^{4}He under pressure*, Phys. Rev. B **84**, 184506 (2011). p. 25

[95] R. Lopes, C. Eigen, N. Navon, D. Clément, R. P. Smith, and Z. Hadzibabic, *Quantum Depletion of a Homogeneous Bose-Einstein Condensate*, Phys. Rev. Lett. **119**, 190404 (2017). p. 25

[96] D. S. Petrov and G. E. Astrakharchik, *Ultradilute Low-Dimensional Liquids*, Phys. Rev. Lett. **117**, 100401 (2016). p. 26

[97] T. Ilg, J. Kumlin, L. Santos, D. S. Petrov, and H. P. Büchler, *Dimensional crossover for the beyond-mean-field correction in Bose gases*, arXiv:1806.01784 (2018). p. 26

[98] D. Edler, C. Mishra, F. Wächtler, R. Nath, S. Sinha, and L. Santos, *Quantum Fluctuations in Quasi-One-Dimensional Dipolar Bose-Einstein Condensates*, Phys. Rev. Lett. **119**, 050403 (2017). p. 26

[99] If not stated otherwise, we assume a stable Bose-Einstein condensate of ^{162}Dy. The parameters therefore are mass $m = 162\,u$, dipolar length $a_{\mathrm{dd}} = 131\,a_0$ and scattering length $a_{\mathrm{s}} = 140\,a_0$. For the homogeneous gas, the density is fixed to $n = 10^{20}\,\mathrm{m}^{-3}$. For the trapped gas, we employ a spherical harmonic trapping potential of mean frequency $\bar{\omega} = 2\pi \times 70\,\mathrm{Hz}$ close to the experiment. pp. 27–29, 31, 33, 37–41, 43, 47

[100] L. Santos, G. V. Shlyapnikov, P. Zoller, and M. Lewenstein, *Bose-Einstein Condensation in Trapped Dipolar Gases*, Phys. Rev. Lett. **85**, 1791 (2000). p. 27

[101] G. Bismut, B. Laburthe-Tolra, E. Maréchal, P. Pedri, O. Gorceix, and L. Vernac, *Anisotropic Excitation Spectrum of a Dipolar Quantum Bose Gas*, Phys. Rev. Lett. **109**, 155302 (2012). pp. 28, 96

[102] J. R. Abo-Shaeer, C. Raman, J. M. Vogels, and W. Ketterle, *Observation of Vortex Lattices in Bose-Einstein Condensates*, Science **292**, 476 (2001). pp. 29, 101, 102, 104

[103] S. Yi and H. Pu, *Vortex structures in dipolar condensates*, Phys. Rev. A **73**, 061602 (2006). pp. 29, 95, 103–105

[104] B. C. Mulkerin, R. M. W. van Bijnen, D. H. J. O'Dell, A. M. Martin, and N. G. Parker, *Anisotropic and Long-Range Vortex Interactions in Two-Dimensional Dipolar Bose Gases*, Phys. Rev. Lett. **111**, 170402 (2013). pp. 29, 95

[105] N. R. Cooper, E. H. Rezayi, and S. H. Simon, *Vortex Lattices in Rotating Atomic Bose Gases with Dipolar Interactions*, Phys. Rev. Lett. **95**, 200402 (2005). pp. 29, 95, 103, 105

[106] A. A. Abrikosov, *The magnetic properties of superconducting alloys*, Journal of Physics and Chemistry of Solids **2**, 199 (1957). pp. 29, 101

[107] L. Landau, *The theory of superfluidity of helium II*, J. Phys. U.S.S.R. **60**, 71 (1941). pp. 30, 34, 95

[108] Z.-Q. Yu, *Landau criterion for an anisotropic Bose-Einstein condensate*, Phys. Rev. A **95**, 033618 (2017). pp. 30, 31

[109] B. E. A. Saleh and M. C. Teich, *Fundamentals of Photonics* (John Wiley & Sons, 1991). pp. 32, 53, 77

[110] L. Santos, G. V. Shlyapnikov, and M. Lewenstein, *Roton-Maxon Spectrum and Stability of Trapped Dipolar Bose-Einstein Condensates*, Phys. Rev. Lett. **90**, 250403 (2003). pp. 32, 34

[111] U. Fischer, *Stability of quasi-two-dimensional Bose-Einstein condensates with dominant dipole-dipole interactions*, Phys. Rev. A **73**, 031602(R) (2006). p. 32

[112] M. Klawunn and L. Santos, *Hybrid multisite excitations in dipolar condensates in optical lattices*, Phys. Rev. A **80**, 013611 (2009). p. 32

[113] D. G. Henshaw and A. D. B. Woods, *Modes of Atomic Motions in Liquid Helium by Inelastic Scattering of Neutrons*, Phys. Rev. **121**, 1266 (1961). p. 34

[114] S. Komineas and N. R. Cooper, *Vortex lattices in Bose-Einstein condensates with dipolar interactions beyond the weak-interaction limit*, Phys. Rev. A **75**, 023623 (2007). p. 34

[115] R. Rosensweig, *Ferrohydrodynamics* (Cambridge University Press, 1985). p. 34

[116] M. D. Cowley and R. E. Rosensweig, *The interfacial stability of a ferromagnetic fluid*, Journal of Fluid Mechanics **30**, 671 (1967). p. 34

[117] R. Richter and A. Lange, *Surface instabilities of ferrofluids*, in *Colloidal magnetic fluids: basics, development and application of ferrofluids*, edited by S. Odenbach (Springer Berlin Heidelberg, 2009). p. 34

[118] S. Ronen, D. C. E. Bortolotti, and J. L. Bohn, *Radial and Angular Rotons in Trapped Dipolar Gases*, Phys. Rev. Lett. **98**, 030406 (2007). pp. 34, 45

[119] R. N. Bisset, D. Baillie, and P. B. Blakie, *Roton excitations in a trapped dipolar Bose-Einstein condensate*, Phys. Rev. A **88**, 043606 (2013). p. 34

[120] N. G. Parker, C. Ticknor, A. M. Martin, and D. H. J. O'Dell, *Structure formation during the collapse of a dipolar atomic Bose-Einstein condensate*, Phys. Rev. A **79**, 013617 (2009). pp. 34, 45, 48

[121] R. M. Wilson, S. Ronen, and J. L. Bohn, *Angular collapse of dipolar Bose-Einstein condensates*, Phys. Rev. A **80**, 023614 (2009). pp. 34, 45, 48

[122] L. Chomaz, R. M. W. van Bijnen, D. Petter, G. Faraoni, S. Baier, J. H. Becher, M. J. Mark, F. Wächtler, L. Santos, and F. Ferlaino, *Observation of roton mode population in a dipolar quantum gas*, Nat. Phys. **14**, 442 (2018). pp. 34, 49

[123] R. M. Wilson, S. Ronen, and J. L. Bohn, *Critical Superfluid Velocity in a Trapped Dipolar Gas*, Phys. Rev. Lett. **104**, 094501 (2010). p. 34

[124] C. Ticknor, R. M. Wilson, and J. L. Bohn, *Anisotropic Superfluidity in a Dipolar Bose Gas*, Phys. Rev. Lett. **106**, 065301 (2011). p. 34

[125] R. Grimm, M. Weidemüller, and Y. B. Ovchinnikov, *Optical Dipole Traps for Neutral Atoms*, Adv. At. Mol. Opt. Phys. **42**, 95 (2000). pp. 35, 53

[126] F. Dalfovo, S. Giorgini, L. P. Pitaevskii, and S. Stringari, *Theory of Bose-Einstein condensation in trapped gases*, Rev. Mod. Phys. **71**, 463 (1999). pp. 35, 97

[127] D. H. J. O'Dell, S. Giovanazzi, and C. Eberlein, *Exact Hydrodynamics of a Trapped Dipolar Bose-Einstein Condensate*, Phys. Rev. Lett. **92**, 250401 (2004). p. 36

[128] G. Baym and C. J. Pethick, *Ground-State Properties of Magnetically Trapped Bose-Condensed Rubidium Gas*, Phys. Rev. Lett. **76**, 6 (1996). p. 36

[129] V. M. Pérez-García, H. Michinel, J. I. Cirac, M. Lewenstein, and P. Zoller, *Low Energy Excitations of a Bose-Einstein Condensate: A Time-Dependent Variational Analysis*, Phys. Rev. Lett. **77**, 5320 (1996). p. 36

[130] V. M. Pérez-García, H. Michinel, J. I. Cirac, M. Lewenstein, and P. Zoller, *Dynamics of Bose-Einstein condensates: Variational solutions of the Gross-Pitaevskii equations*, Phys. Rev. A **56**, 1424 (1997). p. 36

[131] S. Giovanazzi, A. Görlitz, and T. Pfau, *Ballistic expansion of a dipolar condensate*, Journal of Optics B: Quantum and Semiclassical Optics **5**, S208 (2003). p. 36

[132] R. M. W. van Bijnen, N. G. Parker, S. J. J. M. F. Kokkelmans, A. M. Martin, and D. H. J. O'Dell, *Collective excitation frequencies and stationary states of trapped dipolar Bose-Einstein condensates in the Thomas-Fermi regime*, Phys. Rev. A **82**, 033612 (2010). pp. 36, 43

[133] S. Müller, J. Billy, E. A. L. Henn, H. Kadau, A. Griesmaier, M. Jona-Lasinio, L. Santos, and T. Pfau, *Stability of a dipolar Bose-Einstein condensate in a one-dimensional lattice*, Phys. Rev. A **84**, 053601 (2011). p. 37

[134] J. Werner, A. Griesmaier, S. Hensler, J. Stuhler, T. Pfau, A. Simoni, and E. Tiesinga, *Observation of Feshbach Resonances in an Ultracold Gas of* ^{52}Cr, Phys. Rev. Lett. **94**, 183201 (2005). p. 38

[135] S. Stringari and J. Treiner, *Surface properties of liquid* ^{3}*He and* ^{4}*He: A density-functional approach*, Phys. Rev. B **36**, 8369 (1987). p. 42

[136] F. Dalfovo, A. Lastri, L. Pricaupenko, S. Stringari, and J. Treiner, *Structural and dynamical properties of superfluid helium: a density-functional approach*, Phys. Rev. B **52**, 1193 (1995). pp. 42, 46

[137] D. S. Jin, J. R. Ensher, M. R. Matthews, C. E. Wieman, and E. A. Cornell, *Collective Excitations of a Bose-Einstein Condensate in a Dilute Gas*, Phys. Rev. Lett. **77**, 420 (1996). p. 42

[138] M.-O. Mewes, M. R. Andrews, N. J. van Druten, D. M. Kurn, D. S. Durfee, C. G. Townsend, and W. Ketterle, *Collective Excitations of a Bose-Einstein Condensate in a Magnetic Trap*, Phys. Rev. Lett. **77**, 988 (1996). p. 42

[139] D. S. Jin, M. R. Matthews, J. R. Ensher, C. E. Wieman, and E. A. Cornell, *Temperature-Dependent Damping and Frequency Shifts in Collective Excitations of a Dilute Bose-Einstein Condensate*, Phys. Rev. Lett. **78**, 764 (1997). p. 42

[140] O. M. Maragò, S. A. Hopkins, J. Arlt, E. Hodby, G. Hechenblaikner, and C. J. Foot, *Observation of the Scissors Mode and Evidence for Superfluidity of a Trapped Bose-Einstein Condensed Gas*, Phys. Rev. Lett. **84**, 2056 (2000). pp. 42, 74, 76

[141] J. Bacri and F. Elias, *Ferrofluids: a model system of self-organised equilibrium*, in *Morphogenesis*, edited by P. Bourgine and A. Lesne (Springer Berlin Heidelberg, 2011). pp. 45, 46, 108

[142] H. Kadau, *Rosensweig Instability and Droplets in a Quantum Ferrofluid of Dysprosium Atoms*, PhD Thesis (University of Stuttgart, 2016). pp. 46, 51, 53

[143] M. Schmitt, *A Self-bound Dilute Quantum Liquid of Dysprosium Atoms*, PhD Thesis (University of Stuttgart, 2017). pp. 46, 51, 53, 81, 83, 85

[144] C. F. Barenghi and N. G. Parker, *A primer on quantum fluids* (SpringerBriefs in Physics, 2016). pp. 46, 112, 114

[145] F. Abraham, *A theory for the thermodynamics and structure of nonuniform systems, with applications to the liquid–vapor interface and spinodal decomposition*, J. Chem. Phys. **63**, 157 (1975). p. 46

[146] M. J. P. Nijmeijer, A. F. Bakker, C. Bruin, and J. H. Sikkenk, *A molecular dynamics simulation of the Lennard-Jones liquid–vapor interface*, J. Chem. Phys. **89**, 3789 (1988). p. 46

[147] P. Ring and P. Schuck, *The Nuclear Many-Body Problem* (Springer-Verlag Berlin Heidelberg, 1980). p. 46

[148] S. Ronen, D. C. E. Bortolotti, and J. L. Bohn, *Bogoliubov modes of a dipolar condensate in a cylindrical trap*, Phys. Rev. A **74**, 013623 (2006). pp. 49, 113

[149] P. B. Blakie, D. Baillie, and R. N. Bisset, *Roton spectroscopy in a harmonically trapped dipolar bose-einstein condensate*, Phys. Rev. A **86**, 021604 (2012). p. 49

[150] D. Baillie, R. M. Wilson, and P. B. Blakie, *Collective Excitations of Self-Bound Droplets of a Dipolar Quantum Fluid*, Phys. Rev. Lett. **119**, 255302 (2017). p. 49

[151] H. Saito, *Path-Integral Monte Carlo Study on a Droplet of a Dipolar Bose–Einstein Condensate Stabilized by Quantum Fluctuation*, J. Phys. Soc. Japan **85**, 053001 (2016). p. 50

[152] A. Macia, J. Sánchez-Baena, J. Boronat, and F. Mazzanti, *Droplets of Trapped Quantum Dipolar Bosons*, Phys. Rev. Lett. **117**, 205301 (2016). p. 50

[153] F. Cinti, A. Cappellaro, L. Salasnich, and T. Macri, *Superfluid Filaments of Dipolar Bosons in Free Space*, Phys. Rev. Lett. **119**, 215302 (2017). p. 50

[154] F. Cinti and M. Boninsegni, *Classical and quantum filaments in the ground state of trapped dipolar Bose gases*, Phys. Rev. A **96**, 013627 (2017). p. 50

[155] R. Bombin, J. Boronat, and F. Mazzanti, *Dipolar Bose Supersolid Stripes*, Phys. Rev. Lett. **119**, 250402 (2017). p. 50

[156] M. Wenzel, *A dysprosium quantum gas in highly controllable optical traps*, Master Thesis (University of Stuttgart, 2015). pp. 51, 53, 55, 56, 103

[157] C. J. Foot, *Atomic Physics* (Oxford University Press, 2005). p. 51

[158] I. Segal, L. Halicz, and I. T. Platzner, *Isotope ratio measurements of dysprosium by multiple collection inductively coupled plasma mass spectrometry*, Int. J. Mass Spectrom. **216**, 177 (2002). p. 51

[159] M. Lu, S. H. Youn, and B. L. Lev, *Spectroscopy of a narrow-line laser-cooling transition in atomic dysprosium*, Phys. Rev. A **83**, 012510 (2011). p. 52

[160] M. Gustavsson, H. Lundberg, L. Nilsson, and S. Svanberg, *Lifetime measurements for excited states of rare-earth atoms using pulse modulation of a cw dye-laser beam*, J. Opt. Soc. Am. **69**, 984 (1979). p. 52

[161] T. Maier, H. Kadau, M. Schmitt, A. Griesmaier, and T. Pfau, *Narrow-line magneto-optical trap for dysprosium atoms*, Opt. Lett. **39**, 3138 (2014). pp. 52, 57

[162] M. Eisenmann, *Superfluid Behaviour of Dipolar Quantum Gases*, Master Thesis (University of Stuttgart, 2018). pp. 55, 101

[163] C. C. Bradley, C. A. Sackett, and R. G. Hulet, *Bose-Einstein Condensation of Lithium: Observation of Limited Condensate Number*, Phys. Rev. Lett. **78**, 985 (1997). p. 55

[164] C. M. Bühner, *Fast Magnetic Field Control for the Precise Tuning of Interactions in a Dipolar Gas*, Master Thesis (University of Stuttgart, 2017). p. 56

[165] J. Léonard, A. Morales, P. Zupancic, T. Esslinger, and T. Donner, *Supersolid formation in a quantum gas breaking continuous translational symmetry*, Nature **543**, 87 (2017). p. 59

[166] J.-R. Li, J. Lee, W. Huang, S. Burchesky, B. Shteynas, F. Ç. Top, A. O. Jamison, and W. Ketterle, *A stripe phase with supersolid properties in spin-orbit-coupled Bose-Einstein condensates*, Nature **543**, 91 (2017). p. 59

[167] J. Orenstein and A. J. Millis, *Advances in the Physics of High-Temperature Superconductivity*, Science **288**, 468 (2000). p. 59

[168] M. A. Baranov, M. Dalmonte, G. Pupillo, and P. Zoller, *Condensed matter theory of dipolar quantum gases*, Chem. Rev. **112**, 5012 (2012). pp. 59, 109

[169] S. Giovanazzi, P. Pedri, L. Santos, A. Griesmaier, M. Fattori, T. Koch, J. Stuhler, and T. Pfau, *Expansion dynamics of a dipolar Bose-Einstein condensate*, Phys. Rev. A **74**, 013621 (2006). p. 61

[170] K. Glaum and A. Pelster, *Bose-Einstein condensation temperature of dipolar gas in anisotropic harmonic trap*, Phys. Rev. A **76**, 023604 (2007). p. 61

[171] R. Gati and M. K. Oberthaler, *A bosonic Josephson junction*, J. Phys. B **40**, R61 (2007). pp. 67, 68

[172] A. Smerzi, S. Fantoni, S. Giovanazzi, and R. Shenoy, *Quantum Coherent Atomic Tunneling between Two Trapped Bose-Einstein Condensates*, Phys. Rev. Lett. **79**, 4950 (1997). pp. 68, 71, 72

[173] M. Abad, M. Guilleumas, R. Mayol, M. Pi, and D. M. Jezek, *A dipolar self-induced bosonic Josephson junction*, Europhysics Lett. **94**, 10004 (2011). p. 68

[174] R. Gati, B. Hemmerling, J. Fölling, M. Albiez, and M. K. Oberthaler, *Noise thermometry with two weakly coupled bose-einstein condensates*, Phys. Rev. Lett. **96**, 130404 (2006). p. 69

[175] G. C. Baldwin and G. S. Klaiber, *Photo-fission in heavy elements*, Phys. Rev. **71**, 3 (1947). p. 73

[176] M. Goldhaber and E. Teller, *On nuclear dipole vibrations*, Phys. Rev. **74**, 1046 (1948). p. 73

[177] N. Lo Iudice and F. Palumbo, *New isovector collective modes in deformed nuclei*, Phys. Rev. Lett. **41**, 1532 (1978). p. 73

[178] E. Lipparini and S. Stringari, *Isovector M1 rotatitional states in deformed nuclei*, Phys. Lett. **130B**, 139 (1983). p. 73

[179] K. Heyde, P. Von Neumann-Cosel, and A. Richter, *Magnetic dipole excitations in nuclei: Elementary modes of nucleonic motion*, Rev. Mod. Phys. **82**, 2365 (2010). pp. 73, 74

[180] D. Guéry-Odelin and S. Stringari, *Scissors Mode and Superfluidity of a Trapped Bose-Einstein Condensed Gas*, Phys. Rev. Lett. **83**, 4452 (1999). pp. 73, 76

[181] J. Enders, H. Kaiser, P. von Neumann-Cosel, C. Rangacharyulu, and A. Richter, *Comprehensive analysis of the scissors mode in heavy even-even nuclei*, Phys. Rev. C **59**, R1851 (1999). p. 74

[182] K. Baumann, N. Q. Burdick, M. Lu, and B. L. Lev, *Observation of low-field Fano-Feshbach resonances in ultracold gases of dysprosium*, Phys. Rev. A **89**, 020701 (2014). pp. 79, 90

[183] R. C. Paule and J. Mandel, *Consensus Values, Regressions and Weighting Factors*, J. Res. Natl. Bur. Stand. **94**, 197 (1989). p. 81

[184] Y. Tang, A. Sykes, N. Q. Burdick, J. L. Bohn, and B. L. Lev, *s-wave scattering lengths of the strongly dipolar bosons* ^{162}Dy *and* ^{164}Dy, Phys. Rev. A **92**, 022703 (2015). pp. 81, 86, 108

[185] Y. Tang, A. G. Sykes, N. Q. Burdick, J. M. DiSciacca, D. S. Petrov, and B. L. Lev, *Anisotropic Expansion of a Thermal Dipolar Bose Gas*, Phys. Rev. Lett. **117**, 155301 (2016). pp. 81, 86

[186] A. Boudjemâa, *Quantum dilute droplets of dipolar bosons at finite temperature*, Annals of Physics **381**, 68 (2017). pp. 85, 86

[187] E. Aybar and M. O. Oktel, *Temperature Dependent Density Profiles of Dipolar Droplets*, arXiv:1805.06261 (2018). pp. 85, 134

[188] Private Communication with the author of [187]. p. 86

[189] J. P. Toennies and A. F. Vilesov, *Superfluid helium droplets: A uniquely cold nanomatrix for molecules and molecular complexes*, Angew. Chemie **43**, 2622 (2004). p. 88

[190] R. Schützhold, M. Uhlmann, Y. Xu, and U. R. Fischer, *Mean-Field Expansion in Bose–Einstein Condensates With Finite-Range Interactions*, Int. J. Mod. Phys. B **20**, 3555 (2006). p. 88

[191] A. Bergschneider, V. M. Klinkhamer, J. H. Becher, R. Klemt, G. Zürn, P. M. Preiss, and S. Jochim, *Spin-resolved single-atom imaging of 6Li in free space*, Phys. Rev. A **97**, 063613 (2018). p. 91

[192] A. Trautmann, G. Durastante, C. Politi, M. Sohmen, M. J. Mark, and F. Ferlaino, *Dipolar Quantum Mixtures of Erbium and Dysprosium Atoms*, arXiv:1807.07555 (2018). p. 91

[193] C. Raman, M. Köhl, R. Onofrio, D. S. Durfee, C. E. Kuklewicz, Z. Hadzibabic, and W. Ketterle, *Evidence for a Critical Velocity in a Bose-Einstein Condensed Gas*, Phys. Rev. Lett. **83**, 2502 (1999). p. 95

[194] R. Onofrio, C. Raman, J. M. Vogels, J. R. Abo-Shaeer, A. P. Chikkatur, and W. Ketterle, *Observation of Superfluid Flow in a Bose-Einstein Condensed Gas*, Phys. Rev. Lett. **85**, 2228 (2000). pp. 95, 100

[195] R. Desbuquois, L. Chomaz, T. Yefsah, J. Léonard, J. Beugnon, C. Weitenberg, and J. Dalibard, *Superfluid behaviour of a two-dimensional Bose gas*, Nat. Phys. **8**, 645 (2012). p. 95

[196] D. E. Miller, J. K. Chin, C. A. Stan, Y. Liu, W. Setiawan, C. Sanner, and W. Ketterle, *Critical Velocity for Superfluid Flow across the BEC-BCS Crossover*, Phys. Rev. Lett. **99**, 070402 (2007). p. 95

[197] W. Weimer, K. Morgener, V. P. Singh, J. Siegl, K. Hueck, N. Luick, L. Mathey, and H. Moritz, *Critical Velocity in the BEC-BCS Crossover*, Phys. Rev. Lett. **114**, 095301 (2015). p. 95

[198] B. Jackson, J. F. McCann, and C. S. Adams, *Dissipation and vortex creation in Bose-Einstein condensed gases*, Phys. Rev. A **61**, 051603 (2000). p. 96

[199] K. Glaum and A. Pelster, *Bose-Einstein condensation temperature of dipolar gas in anisotropic harmonic trap*, Phys. Rev. A **76**, 023604 (2007). p. 97

[200] M. Ghabour and A. Pelster, *Bogoliubov theory of dipolar Bose gas in a weak random potential*, Phys. Rev. A **90**, 063636 (2014). p. 98

[201] P. O. Fedichev and G. V. Shlyapnikov, *Critical velocity in cylindrical Bose-Einstein condensates*, Phys. Rev. A **63**, 045601 (2001). p. 100

[202] V. P. Singh, W. Weimer, K. Morgener, J. Siegl, K. Hueck, N. Luick, H. Moritz, and L. Mathey, *Probing superfluidity of Bose-Einstein condensates via laser stirring*, Phys. Rev. A **93**, 023634 (2016). p. 100

[203] J. S. Stießberger and W. Zwerger, *Critcal velocity of superfluid flow past large obstacles in Bose-Einstein condensates*, Phys. Rev. A **62**, 061601 (2000). p. 100

[204] S. Burger, F. S. Cataliotti, C. Fort, F. Minardi, M. Inguscio, M. L. Chiofalo, and M. P. Tosi, *Superfluid and dissipative dynamics of a Bose-Einstein condensate in a periodic optical potential*, Phys. Rev. Lett. **86**, 4447 (2001). p. 100

[205] A. P. Chikkatur, A. Görlitz, D. M. Stamper-Kurn, S. Inouye, S. Gupta, and W. Ketterle, *Suppression and Enhancement of Impurity Scattering in a Bose-Einstein Condensate*, Phys. Rev. Lett. **85**, 483 (2000). p. 100

[206] M. Delehaye, S. Laurent, I. Ferrier-Barbut, S. Jin, F. Chevy, and C. Salomon, *Critical Velocity and Dissipation of an Ultracold Bose-Fermi Counterflow*, Phys. Rev. Lett. **115**, 265303 (2015). p. 100

[207] M. R. Matthews, B. P. Anderson, P. C. Haljan, D. S. Hall, C. E. Wieman, and E. A. Cornell, *Vortices in a Bose-Einstein Condensate*, Phys. Rev. Lett. **83**, 2498 (1999). p. 101

[208] Y. A. Rocher and J. C. Renard, *On the existence of several-quanta flux lines in type II superconductors*, Phys. Lett. A **25**, 119 (1967). p. 101

[209] H. F. Hess, R. B. Robinson, R. C. Dynes, J. M. Valles, and J. V. Waszczak, *Scanning-Tunneling-Microscope Observation of the Abrikosov Flux Lattice and the Density of States near and inside a Fluxoid*, Phys. Rev. Lett. **62**, 214 (1989). p. 101

[210] C. A. Bolle, P. L. Gammel, D. G. Grier, C. A. Murray, D. J. Bishop, D. B. Mitzi, and A. Kapitulnik, *Observation of a commensurate array of flux chains in tilted flux lattices in Bi-Sr-Ca-Cu-O single crystals*, Phys. Rev. Lett. **66**, 112 (1991). p. 101

[211] J. R. Abo-Shaeer, C. Raman, and W. Ketterle, *Formation and decay of vortex lattices in bose-einstein condensates at finite temperatures*, Phys. Rev. Lett. **88**, 070409 (2002). p. 101

[212] For the vortex simulations, we assume a stable Bose-Einstein condensate of ^{162}Dy and parameters of the experiment. These are mass $m = 162\,u$, dipolar length $a_{\mathrm{dd}} = 131\,a_0$ and scattering length $a_{\mathrm{s}} = 140\,a_0$ with a cylindrical harmonic trap $f_x = f_y = 50\,\mathrm{Hz}$ and $f_z = 150\,\mathrm{Hz}$. We note, that the energy-dependence on vortex position is very weak, which leads to slow convergence of the imaginary time evolution. As a consequence, the final vortex position depends on the initial phase step, which we use to seed vortices. In the isotropic case the magnetic field points along $\hat{\boldsymbol{z}}$ in the image plane and for the anisotropic case it points upwards along $\hat{\boldsymbol{y}}$. The color code with white-gray-hue is proportional to the column density integrated along $\hat{\boldsymbol{z}}$ with a hue determined by the phase of the condensate. pp. 102–105

[213] A. L. Fetter, *Rotating trapped Bose-Einstein condensates*, Rev. Mod. Phys. **81**, 647 (2009). pp. 101, 111

[214] F. Chevy, K. W. Madison, and J. Dalibard, *Measurement of the Angular Momentum of a Rotating Bose-Einstein Condensate*, Phys. Rev. Lett. **85**, 2223 (2000). p. 102

[215] For these states we use a box of length $10\,\mu\mathrm{m}$ with periodic boundaries in the plane and seed the patterns with a randomized initial wavefunction breaking the symmetry. Along the magnetic field axis, which points in the plane, there is a harmonic confinement $\omega_z/2\pi = 1\,\mathrm{kHz}$. The interaction parameters with $a_{\mathrm{s}} = 70\,a_0$ and $a_{\mathrm{dd}} = 131\,a_0$ match ^{164}Dy atoms leading to a peak density $n_0 \approx 6 \times 10^{21}\,\mathrm{m}^{-3}$. Although this is reminiscent of a quasi-2D setting, the quantum gas is well in the 3D regime with $\mu \gg \hbar\omega_z$ owing to the large density. p. 108

[216] L. D. Marco, G. Valtolina, K. Matsuda, W. Tobias, J. Covey, and J. Ye, *A Fermi Degenerate Gas of Polar Molecules*, arXiv:1808.00028 (2018). p. 110

[217] D. Peter, *GitHub repository "sharkdp/GPE-Solver"*, (May 2014) `https://github.com/sharkdp/GPE-Solver`. p. 111

[218] D. Peter, *Theoretical investigations of dipolar quantum gases in multi-well potentials*, Diploma Thesis (University of Stuttgart, 2011). p. 111

[219] P. Muruganandam and S. K. Adhikari, *Fortran programs for the time-dependent Gross-Pitaevskii equation in a fully anisotropic trap*, **180**, 1888 (2009). p. 111

[220] *The design and implementation of FFTW3*, Proc. IEEE **93**, 216 (2005). p. 113

[221] P. B. Blakie, A. S. Bradley, M. J. Davis, R. J. Ballagh, and C. W. Gardiner, *Dynamics and statistical mechanics of ultra-cold Bose gases using c-field techniques*, Adv. Phys. **57**, 363 (2008). p. 114

[222] I. Ferrier-Barbut, *Mixtures of Bose and Fermi superfluids*, PhD Thesis (ENS et LKB Paris, 2014). p. 119

[223] T. Weber, J. Herbig, M. Mark, H.-C. Nägerl, and R. Grimm, *Three-Body Recombination at Large Scattering Lengths in an Ultracold Atomic Gas*, Phys. Rev. Lett. **91**, 123201 (2003). p. 119

[224] E. A. Burt, R. W. Ghrist, C. J. Myatt, M. J. Holland, E. A. Cornell, and C. E. Wieman, *Coherence, Correlations, and Collisions: What One Learns about Bose-Einstein Condensates from Their Decay*, Phys. Rev. Lett. **79**, 337 (1997). p. 120

Acknowledgement

Auch wenn die Quantenwelt viele Überraschungen bereit hält, entdeckt man einen neuen Materiezustand nicht jeden Tag. Zu diesem Erlebnis am Experiment haben viele Leute beigetragen, bei denen ich mich an dieser Stelle bedanken möchte.

Natürlich beginnt und endet alles mit dir, Tilman. Deine Faszination für die Physik ist damals in der Vorlesung zur Atomphysik auf mich übergesprungen. Deine Art deinen Studenten großen Freiraum zu lassen und sie auch mal ins kalte Wasser zu werfen lässt in meinen Augen den größten Spielraum für die persönliche Entwicklung. Desweiteren hast du damals im Studium den Kontakt zu Joseph in Toronto vermittelt. Der Auslandsaufenthalt war eine Erfahrung, die mich persönlich und wissenschaftlich reifer gemacht hat. Mit der Betreuung der Übungsgruppen konnte ich hoffentlich einen Teil deiner Faszination an die nächste Generation von Studenten weitergeben.

Desweiteren möchte ich meinem Mitberichter Prof. Dr. Martin Dressel und dem Prüfungsvorsitzenden Prof. Dr. Hans Peter Büchler, der uns auch von theoretischer Seite mehr als einmal unterstützt hat, danken.

Von experimenteller Seite gilt mein größter Dank Thomas, Holger und Matthias, die mich zur Masterarbeit an "ihrem" Experiment aufgenommen haben. Die Zeit mit euch war immer unterhaltsam und interessant zugleich. In diesem Jahr habe ich tausend neue Dinge von euch gelernt und ihr habt mir letztendlich die Entscheidung leicht gemacht für die Doktorarbeit am Experiment zu bleiben, was sich mehr als ausgezahlt hat. Ein Grundpfeiler unseres Experiments war natürlich auch Igor. Du hast dich in den vier Jahren unserer Zusammenarbeit vom einfachen Student zum Gruppenleiter entwickelt und mit unermüdlicher Motivation dafür gesorgt, dass mir nie langweilig wurde. Letztlich habe ich von dir gelernt wie man Physik "macht", danke dafür. Eine riesige Entwicklung hat auch unser "Jungspund" Fabian vollzogen. Danke für die super Zeit am Experiment, das du inzwischen besser als ich meisterst. Vortices und das Supersolid stehen ja noch aus, hol sie dir! Außerdem möchte ich Tim danken. Du warst immer als Ansprechpartner zu haben und hast all meine Formulierungen geschliffen wie einen Rohdiamanten. Dem Team für das neue Experiment bestehend aus Jan-Niklas, Julian, Mingyang und Arup wünsche ich viel Erfolg und schnelles Gelingen! Ich hoffe unsere Erfahrungen mit der aktuellen Maschine bringen euch weiter und ihr findet ganz neue, noch nie dagewesene Physik. Zuletzt gehörten zum Team auch noch eine Reihe von Bachelor- und Masterstudenten. Ihr habt das Experiment weiter gebracht und mich gleichzeitig das Vermitteln von Wissen gelehrt. Danke an Isabel, Clarissa, Tobias, Tobias, Carl, Michael und Yannick.

Natürlich ist dies nur ein kleiner Teil des Instituts. Danke an das restliche Team. Ihr habt jeden langweiligen Rydberg-Talk, sei es mit kalten oder warmen Atomen, durch die unterhaltsamen Mittagspausen und Abende wieder wett gemacht. Mein Dank gilt auch dem benachbarten Rübli-Team, die jede Art von Werkzeug fein säuberlich aufgereiht zum Ausleihen bereit halten, allen voran Christian, mit dem ich im kanadischen Winter ausharren durfte. Desweiteren möchte ich Astrid, Kati und Karin für die grandiose Organisation und Verwaltung der vielen Rechnungen und Dienstreisen danken.
Den größten Anteil an meiner Laufbahn haben wohl meine Eltern. Ihr habt mich von Kindesbeinen stets unterstützt und motiviert meinen Weg zu finden. Vielen Dank.
Zum Schluss möchte ich mich bei meiner zukünftigen Frau Yvonne bedanken. Mit deiner Spontaneität und Lebensfreude motivierst du mich immer wieder aufs Neue. Du hast uns mit Emilia das größte Geschenk gemacht.